A High-Affinity Calmodulin-Binding Site in the CyaA Toxin Translocation Domain is Essential for Invasion of Eukaryotic Cells

Alexis Voegele, Mirko Sadi, Darragh Patrick O'Brien, Pauline Gehan, Dorothée Raoux-barbot, Maryline Davi, Sylviane Hoos, Sébastien Brûlé, Bertrand Raynal, Patrick Weber, et al.

ADVANCED SCIENCE Open Access
www.advancedscience.com

A High-Affinity Calmodulin-Binding Site in the CyaA Toxin Translocation Domain is Essential for Invasion of Eukaryotic Cells

Alexis Voegele, Mirko Sadi, Darragh Patrick O'Brien, Pauline Gehan, Dorothée Raoux-Barbot, Maryline Davi, Sylviane Hoos, Sébastien Brûlé, Bertrand Raynal, Patrick Weber, Ariel Mechaly, Ahmed Haouz, Nicolas Rodriguez, Patrice Vachette, Dominique Durand, Sébastien Brier, Daniel Ladant, and Alexandre Chenal**

The molecular mechanisms and forces involved in the translocation of bacterial toxins into host cells are still a matter of intense research. The adenylate cyclase (CyaA) toxin from *Bordetella pertussis* displays a unique intoxication pathway in which its catalytic domain is directly translocated across target cell membranes. The CyaA translocation region contains a segment, P454 (residues 454–484), which exhibits membrane-active properties related to antimicrobial peptides. Herein, the results show that this peptide is able to translocate across membranes and to interact with calmodulin (CaM). Structural and biophysical analyses reveal the key residues of P454 involved in membrane destabilization and calmodulin binding. Mutational analysis demonstrates that these residues play a crucial role in CyaA translocation into target cells. In addition, calmidazolium, a calmodulin inhibitor, efficiently blocks CyaA internalization. It is proposed that after CyaA binding to target cells, the P454 segment destabilizes the plasma membrane, translocates across the lipid bilayer and binds calmodulin. Trapping of CyaA by the CaM:P454 interaction in the cytosol may assist the entry of the N-terminal catalytic domain by converting the stochastic motion of the polypeptide chain through the membrane into an efficient vectorial chain translocation into host cells.

1. Introduction

The adenylate cyclase (CyaA) toxin is a major virulence factor produced by *Bordetella pertussis*, the causative agent of whooping cough, and is involved in the early stages of respiratory tract colonization.[1,2] CyaA, a 1706-residue long protein (Figure S1, Supporting Information), is a Repeat-in-ToXin (RTX)[3–6] multi-domain toxin.[7,8] Once secreted by *B. pertussis*, CyaA invades eukaryotic cells through an original molecular mechanism that involves a direct translocation of its N-terminal adenyl cyclase catalytic (AC) domain across the plasma membrane. The ATP-cyclizing, calmodulin-activated AC domain comprises the first 364 N-terminal residues.[9–11] The translocation region (TR, residues 365–527) is essential for AC translocation into target cells.[12] The hydrophobic region (HR, residues 528–710) inserts into the cell membrane and makes cation-selective pores[6,13,14]; the acylation region (AR, residues 711–1005) contains

A. Voegele, M. Sadi, D. P. O'Brien, D. Raoux-Barbot, M. Davi, D. Ladant, A. Chenal
Biochemistry of Macromolecular Interactions Unit
Department of Structural Biology and Chemistry
Institut Pasteur
CNRS UMR3528
Paris 75015, France
E-mail: daniel.ladant@pasteur.fr; alexandre.chenal@pasteur.fr

The ORCID identification number(s) for the author(s) of this article can be found under https://doi.org/10.1002/advs.202003630

DOI: 10.1002/advs.202003630

A. Voegele, M. Sadi
Université de Paris
Sorbonne Paris Cité, Paris 75006, France

P. Gehan, N. Rodriguez
Sorbonne Université
École normale supérieure
PSL University
CNRS
Laboratoire des biomolécules
LBM
Paris 75005, France

S. Hoos, S. Brûlé, B. Raynal
Plateforme de Biophysique Moléculaire
Institut Pasteur
UMR 3528 CNRS
Paris 75015, France

two post-translational acylation sites, at lysines K860 and K983,[15–17] required for the refolding of the CyaA toxin[8,18] and AC translocation across membranes in vivo and in vitro.[2,15,16,19] The cell-receptor binding domain of CyaA (RD, residues 1006–1706) is made up of approximately 40 copies of calcium-binding RTX motifs.[4–6,20]

The dedicated type 1 secretion system (T1SS), made of CyaB, CyaD, and CyaE proteins,[21] recognizes a secretion signal located at the C-terminal extremity of CyaA. Once secreted through the T1SS, the toxin binds calcium and folds in the extracellular milieu. A calcium-induced disorder-to-order transition of the RTX motifs occurs upon CyaA secretion from the low-calcium concentration of the bacterial cytosol to the calcium-rich extracellular environment.[4,20,22–35] CyaA folding is an acylation-dependent and calcium-driven sequential process.[8,18,36]

Invasion of target cells occurs via a unique process among known bacterial toxins. First, RD binds with high affinity to a cell receptor, the CD11b/CD18 integrin that is expressed by a subset of leukocytes (neutrophils, dendritic cells (DC) and macrophages).[37–42] CyaA can also intoxicate cells lacking CD11b/CD18 by directly interacting with the target cell membrane, although with a reduced efficiency.[8,43–46] CyaA then inserts into the membrane of target cells via its hydrophobic domains and AC is directly translocated across the plasma membrane into the cytoplasm in a calcium and membrane-potential dependent manner.[12,19,41,47,48]

Inside the cell, AC binds to calmodulin (CaM) that stabilizes the catalytic site into its active state[10,11,49] to convert ATP into cAMP with a high catalytic turnover (>1000 s^{-1}). Accumulation of supraphysiologic levels of cAMP in target cells alters their phagocytic functions leading to host defense subversion.[2,7,50,51]

Experimental results from the past few decades have provided direct evidence that AC translocation requires CyaA acylation, a calcium gradient, and a membrane potential across the plasma membrane.[16,19,52,53] However, the molecular mechanism and forces involved in the translocation of the CyaA catalytic domain across the plasma membrane have thus far remained elusive. We have previously shown that a peptide, corresponding to the C-terminus of the translocation region TR of CyaA, P454 (residues 454–484, Figure S1, Supporting Information), exhibits membrane-active properties related to antimicrobial peptides (AMPs)[12,54]: this peptide adopts a helical conformation upon membrane interaction and induces a local destabilization of the lipid bilayer.[54–57] This property is likely essential for CyaA as deletion of the TR region (residues 384–489) encompassing the P454 segment, selectively abrogates the ability of the modified toxin to intoxicate target cells.[12]

Here, we show that P454 is able to translocate across a lipid bilayer and binds with high affinity to calcium-loaded calmodulin (holo-CaM). We present structural models and crystal structures of the P454 peptide in complex with holo-CaM, and identified in P454, the amino acid residues that are critical for CaM-binding, membrane interaction, and destabilization. Modifications of these residues within the full-length CyaA toxin are sufficient to fully and specifically abrogate the translocation of the catalytic domain across the cell membrane. Finally, we show that calmidazolium (CDZ), a high-affinity CaM inhibitor, specifically blocks translocation of the AC domain into eukaryotic cells. We propose that once CyaA is inserted into the target cell membrane, the P454 segment can interact with the plasma membrane and destabilize the lipid bilayer, favoring its translocation across the lipid bilayer into the cytosol where it binds CaM. Trapping of the CyaA polypeptide chain by the CaM:P454 interaction may thus assist the irreversible translocation of the N-terminal AC domain. Therefore, CaM is not only a key activator of the catalytic activity of CyaA inside cells, but also acts as an essential cytosolic binder of the CyaA translocation region able to grab the polypeptide chain to favor its entry into target cells.

2. Results

2.1. The P454 Peptide from the CyaA Toxin Binds to Calmodulin

We have previously shown that the P454 peptide, residues 454–484 from the CyaA translocation region, exhibits membrane-active properties similar to antimicrobial peptides (AMPs).[58–60] As with certain AMPs, the P454 peptide displays biophysical properties[54] that are similar to that of many calmodulin-binding peptides: they can form amphiphilic helices, they are positively charged and contain a few aromatic or hydrophobic residues involved in complex stabilization.[61–63] Indeed, we found that P454 binds calmodulin (CaM) in solution in a calcium-dependent manner as shown by analytical ultracentrifugation and far-UV circular dichroism spectroscopy (Figure S2 and Table S1, Supporting Information). Analysis of the thermodynamic parameters of the P454:CaM complex formation by isothermal titration calorimetry (ITC) revealed a calcium-dependent interaction with a dissociation constant of about 90 nM at 25 °C (ΔG_{Kd} = -9.6 kcal mol^{-1}) and a P454:CaM stoichiometry of 1:1 (Figures S3A,B and S4, and Table S2, Supporting Information). No binding could be detected in the absence of calcium (Figure S3A,B, Supporting Information).

The affinity of P454 for CaM is much higher than that for lipid membranes. Indeed, the dissociation constant K_d of the P454:membrane equilibrium (calculated from the partition coefficient Kx = 790 000) is ≈70 µM (ΔG_{Kx} = −8 kcal mol^{-1}, Table S3, Supporting Information), about three orders of magnitude higher than that for CaM. Therefore, based on the free energy difference, $\Delta\Delta G$, P454 should preferentially bind to CaM rather than interact with the membrane. This was confirmed by solution-to-membrane partition of P454 measured by

P. Weber, A. Mechaly, A. Haouz
Institut Pasteur
Plate-forme de cristallographie-C2RT
UMR-3528 CNRS
Paris 75015, France
P. Vachette, D. Durand
Université Paris-Saclay
CEA
CNRS
Institute for Integrative Biology of the Cell (I2BC)
Gif-sur-Yvette 91198, France
S. Brier
Biological NMR Technological Plateform
Center for Technological Resources and Research
Department of Structural Biology and Chemistry
Institut Pasteur
CNRS UMR3528
Paris 75015, France

fluorescence (Figure S5A,B, Supporting Information): P454 progressively partitioned from buffer to membranes as lipid concentration increased. A shift of fluorescence polarity was observed upon addition of calcium-loaded calmodulin (holo-CaM), indicating that a P454:CaM complex was formed whatever the lipid concentration. Holo-CaM is converted into apo-CaM upon EDTA addition, leading to its dissociation from P454 that can then interact again with membranes (Figure S5, Supporting Information).

The preferential binding of P454 to calmodulin over membrane was confirmed by a lipid vesicle permeabilization assay.[54,56] In this set up, addition of P454 peptide to ANTS:DPX loaded vesicles induces membrane permeabilization leading to a dye efflux that is monitored by fluorescence increase as a result of ANTS dequenching. Addition of holo-CaM at an early stage of membrane permeabilization immediately stopped the P454-induced dye efflux (Figure S5C, Supporting Information). This suggests that holo-CaM selectively binds P454 leading to a displacement of the peptide from the membrane and an arrest of the P454-induced vesicle permeabilization. Calcium chelation by EDTA triggered dissociation of the P454:CaM complex and release of the P454 peptide that could partition back into membranes to resume permeabilization of the vesicles, leading to ANTS fluorescence recovery (Figure S5C, Supporting Information). Taken together, these experiments show that P454 is a calcium-dependent calmodulin-binding peptide and that holo-CaM can efficiently antagonize the P454 interaction with membrane. These results prompted us to evaluate the intrinsic propensity of P454 to translocate across a lipid bilayer, in particular if holo-CaM would be asymmetrically present on the *trans* side of the membrane.

2.2. P454 Translocation Across Lipid Bilayers

We investigated the ability of P454 to translocate across membranes using the droplet interface bilayers (DIB) approach.[64] The *cis* droplet population contains the dye-labeled peptide TAMRA-P454 while the *trans* droplet population is prepared in the presence or absence of holo-CaM. After mixing and random formation of pairs of droplets, a lipid bilayer is formed at the interface between two adhering droplets (Figure S6, Supporting Information). We measure the transfer of fluorescence from a *cis* fluorescent droplet to a *trans* non-fluorescent droplet to reveal peptide translocation across the lipid bilayer formed at the droplet interface (Figure S6A, Supporting Information). All dye-labeled peptides used in this study interact with membranes, as evidenced by the fluorescent rings staining the *cis* droplets at the beginning of the experiments. In the absence of calmodulin in the *trans* droplet; no increase of fluorescent P454 is measured in the volume of the *trans* compartment after 15 min of incubation (**Figure 1** and Figure S6B, Supporting Information). Conversely, in the presence of 5 µM of holo-CaM in the *trans* droplet, a significant amount of fluorescence is measured in the *trans* compartment (Figure 1 and Figure S6C, Supporting Information). These results indicate that P454 is competent to translocate across membrane and to bind holo-CaM if present in the *trans* compartment.

We then assayed two other dye-labeled peptides: the first being the H-helix peptide, corresponding to the main binding site of AC (residues 233–254 of CyaA) to CaM and that is involved in adenyl cyclase activation.[11] The second peptide is a P454-derived peptide in which the two arginine residues R461 (R*1*) and R474 (R*2*) were substituted by glutamate residues, hereafter designated $P454_{R\,12E}$. This peptide exhibits a drastically reduced affinity for CaM ($K_d^{R12E} / K_d^{WT} = 300$) and a slightly decreased partitioning into membrane ($K_x^{R12E} / K_x^{WT} = 10$, see below). Both $P454_{R\,12E}$ and H-helix peptides interact with the membrane, as evidenced by the fluorescent ring located on the *cis* lipid leaflet observed at the beginning of the experiment. However, these peptides do not accumulate in the *trans* droplets containing 5 µM of holo-CaM even after 15 min of incubation (Figure 1). These results suggest that the H-helix peptide does not translocate across membrane in these experimental conditions, as this peptide should strongly interact with CaM ($K_d^H = 10$ nM, Figure S7 and Table S4, Supporting Information) and accumulate as a peptide:CaM complex in the *trans* compartment if translocation had occurred. The DIB experiment was also carried out with $P454_{R\,12E}$ in the presence of 100 µM of CaM in the *trans* compartment (Figure S6D, Supporting Information), i.e., at a concentration well above the K_d (22.7 µM) of the $P454_{R\,12E}$:CaM complex formation (Table S3, Supporting Information). In these conditions, a significant accumulation of $P454_{R\,12E}$ in the *trans* compartment was measured, indicating that this peptide was able to translocate across the lipid bilayer and to bind CaM. Taken together, these data indicate that P454 interacts with the *cis* lipid leaflet of the membrane, translocates across the droplet interface bilayers, and forms a peptide:CaM complex in the *trans* compartment, as summarized in Figure S8, Supporting Information.

2.3. Structure and Dynamics of P454:CaM Complex

We further characterized the interaction between P454 and CaM by an integrative structural biology approach. Initial attempts to crystallize the P454:CaM complex were unsuccessful. However, we obtained two distinct crystal forms of CaM in complex with a slightly shorter peptide, P458, corresponding to the residues 458–481 of CyaA (i.e., shorter than P454 by 4 residues (ASAH) at N-terminus and 3 residues (MTQ) at C-terminus), and that displays an affinity for CaM similar to that of P454 (K_d^{CaM} = 240 nM, see Table S3, Supporting Information). In both cases, several copies of CaM and P458 were present in the asymmetric unit (Table S5A, Supporting Information). The superposition of these multiple copies yields an ensemble of P458:CaM conformations (**Figure 2**A and Figure S9, Supporting Infromation), which illustrates the well-documented conformational plasticity of CaM[61,62,65] due to its central helix flexibility.

The dynamics and the overall shape of the P454:CaM complex in solution were confirmed by size exclusion chromatography–small-angle X-ray scattering (SEC-SAXS) measurements.[66] The experimental SAXS pattern of the P454:CaM complex is shown in Figure 2B and the derived structural parameters are compared in Table S6, Supporting Information, to that of the previously analyzed CaM complexes with either the H-helix peptide, corresponding to the main CaM binding segment from the AC domain or the myosin light chain kinase (MLCK) peptide, corresponding to the CaM binding site from myosin light chain kinase.[11] The distance distribution P(r) of the P454:CaM

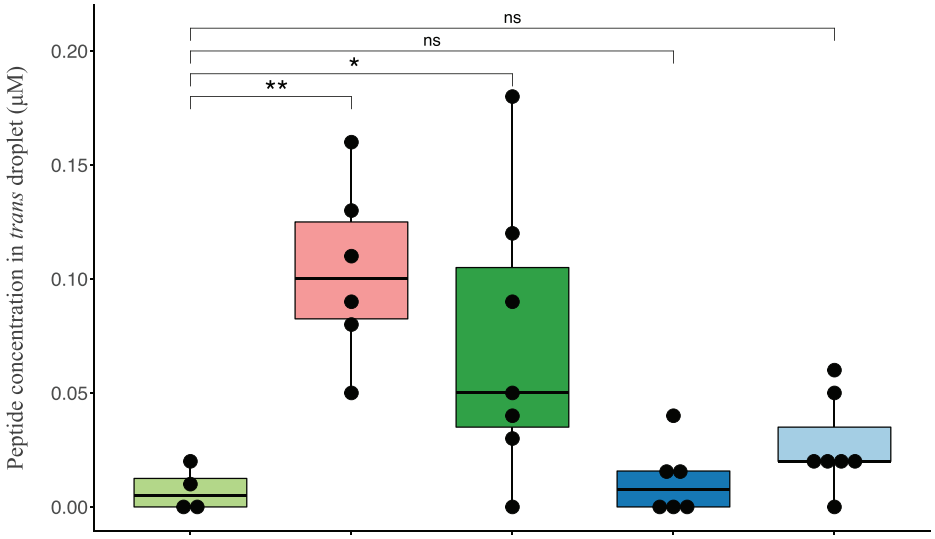

Conditions	A	B	C	D	E
Cis droplet					
Peptide-Tamra	P454	P454	P454	P454 R12E	H-Helix
$CaCl_2$ (mM)	2	2	0.2	2	2
Trans droplet					
CaM (μM)	0	5	5	5	5
$CaCl_2$ (mM)	0.2	0.2	0.2	0.2	0.2

Figure 1. Peptide translocation across droplet interface bilayers. Boxplot representation of the TAMRA-peptide concentration (μM) in the *trans* droplet 15 min after the formation of the droplet interface bilayers (see Experimental Section for details). TAMRA fluorescence was measured in the A) absence and in the B–E) presence of 5 μM CaM in the *trans* droplet; C) in the absence and in (A–B,D–E) the presence of a calcium gradient across the lipid bilayer ($CaCl_2$: 2 mM *cis* versus 0.2 mM *trans*). Concentration of A–C) TAMRA-P454 WT, D) TAMRA-P454 R12E, and the E) TAMRA-H-helix peptides in the *trans* droplets are reported. Four to seven independent trials were conducted for each condition. Mann–Whitney–Wilcoxon test was applied to compare the experiments (ns: $p > 0.05$, *: $p < 0.05$, and **: $p < 0.01$).

complex appears to be intermediate between that of free CaM and H:CaM complex on the one hand, and MLCK:CaM complex on the other (Figure 2C). Ab initio modeling yields a shape intermediate between the globular MLCK:CaM complex and the bi-lobed, extended shape of free CaM and H:CaM complex (Figure 2D), further exemplifying the conformational plasticity of CaM adapted to peptide ligand diversity.

The calculated SAXS curves from ten out of the twelve crystal structures of P458:CaM (PDB 6YNS) obtained are similar to, but slightly different from our experimental SAXS data, while two structures exhibit a different N– and C– domain arrangement and, accordingly, larger amplitude differences with experimental data. Using the model with the closest agreement, we added the six missing N-terminal amino-acids of CaM and the few missing terminal residues of P454 with Modeller[67] to the P458:CaM X-ray structure. We then used this completed complex as a starting model to fit the SAXS data using the modeling program Dadimodo.[68,69] Each run of the program yielded several models, the scattering pattern of which fitted our experimental SAXS data. After superimposition of the N-terminal domain of CaM (N-CaM), all resulting models appeared to exhibit close, but slightly different positions of the C-CaM domain (Figure 2E) that were similar to those observed within the crystal structures (Figure 2A).

Using hydrogen/deuterium exchange mass spectrometry (HDX-MS),[70] we compared the effect of P454 binding to CaM (Figure 2F; FigureS10 and Table S7, Supporting Information) with those observed following H-helix and MLCK peptide binding reported in our previous study.[11] HDX-MS analysis reveals that the inter-lobe helix (residues 73–84) remains accessible in the presence and absence of all three peptides. The MLCK and H-helix peptides induce similar differences in deuterium uptake when bound to CaM as those observed in Figures S4 and S5, Supporting Information from ref. [11]. Interestingly, the deuterium uptake difference induced by P454 binding to CaM is significantly distinct from that observed with MLCK or H-helix, further highlighting the high conformational plasticity of CaM that is able to adapt to a wide diversity of peptide ligands. HDX-MS data show that N-CaM is more strongly stabilized by P454 than by the H-helix peptide as suggested from the comparison of the magnitudes in deuterium uptake differences following P454 binding (Figure S10, Supporting Information) or H-helix binding (see Figure S4, Supporting Information, in ref. [11]). This is in agreement with the mutational analysis of the P454-derived peptides (see below and Table S3, Supporting Information), and the crystal structures of the P458:CaM complex, which show that the C-terminal part of P454 establishes several interactions with the hydrophobic groove of N-CaM (**Figure 3**A). In summary, these

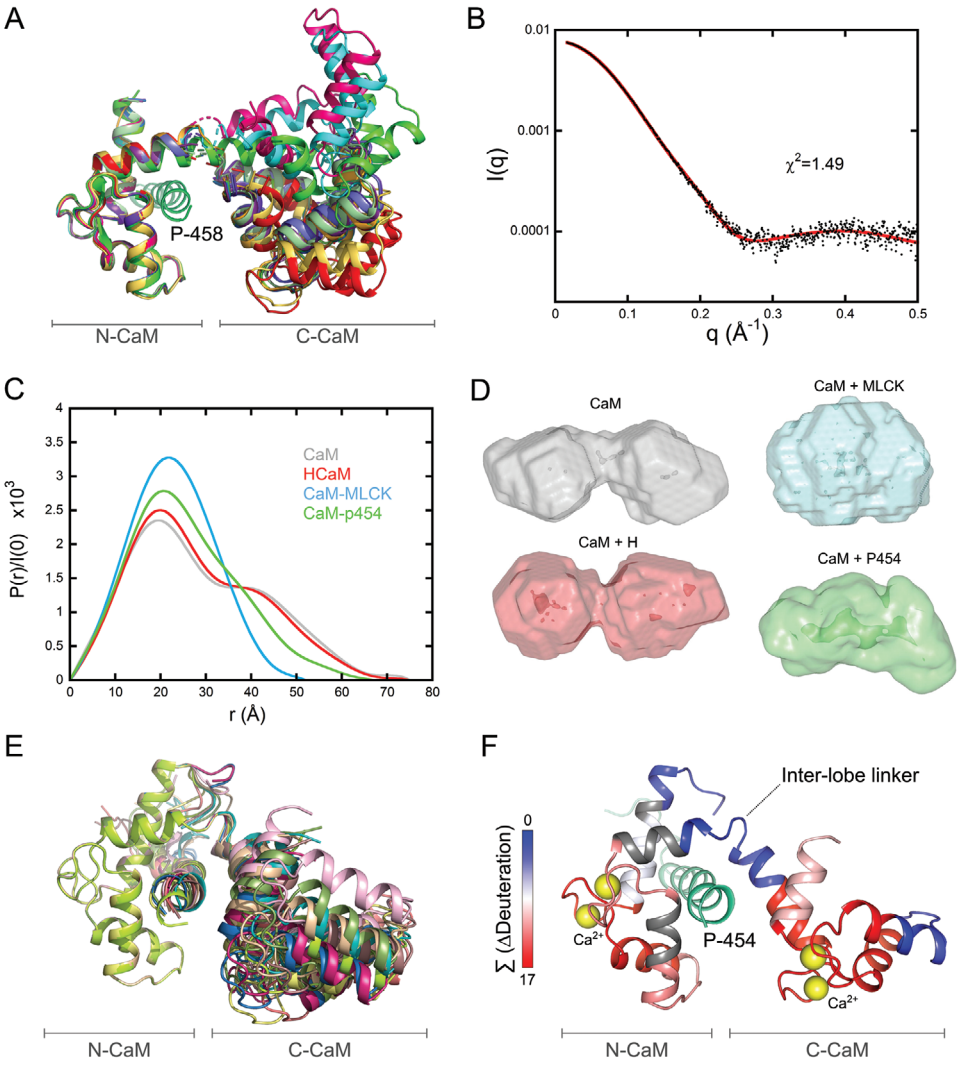

Figure 2. Structure and dynamics of the P454:CaM complex. A) The twelve P458:CaM crystal structures (PDB 6YNS) are displayed after superimposition of C_αs over the range 10 to 70 included, corresponding to the N-ter lobe of calmodulin. The crystal structure 1CLL[92] of the extended conformation of CaM is shown in light green. B) Experimental SAXS curve of the P454:CaM complex (black dots) superimposed over the best fit (red curve) obtained from the structural model shown in Figure 2F. C) Comparison of the four distance distribution functions obtained using the program GNOM for CaM alone (grey), H:CaM (red), MLCK:CaM (cyan), and P454:CaM (green) complexes. D) DAMMIN models of CaM alone, H:CaM, MLCK:CaM, and P454:CaM complexes, shown with the same color code. E) Ten models fitting the SAXS curve shown on Figure 2B obtained using the program DADIMODO[68] are displayed after superimposition of C_αs over the range 10 to 70. F) Effects of P454 on the HDX behavior of CaM. The uptake differences (ΔDeuteration) measured between the free- and P454-bound CaM were extracted for each peptide at each time point, summed, and plotted on the best-fitting structural model of P454:CaM (red curve in 2B). The summed ΔDeuteration values [Σ (ΔDeuteration)] are colored from blue (no variation of deuterium uptake) to red (major reductions of deuterium uptake). Uncovered regions are in grey.

studies establish that P454 is an authentic CaM binder displaying original structural and dynamic features (Figures 2,3; Figures S3 and S7 and Table S3, Supporting Information).

2.4. Mutations Altering P454:CaM and P454:Membrane Interactions In Vitro

The structure of the P454:CaM complex presented above reveals several residues of P454 that might be critical for the interaction with CaM, including the aromatic residue W458, the arginine residues R461 (R*1*) and R474 (R*2*), the aliphatic residues L463, L475, I479 and L481, and finally the histidine residue H477. To corroborate the structural data, we designed a series of P454 derivatives in which several of these residues were mutated and characterized both their CaM binding as well as their membrane interaction properties.

The affinity of the P454-derived peptides for CaM was investigated by fluorescence and ITC (Table S3 and Figure S11, Supporting Information) through the determination of the dissociation constant K_d and the free energy of the peptide:CaM complex (ΔG_{Kd}). Our data shows that the affinity of the P454-derived peptides for CaM is mainly altered by mutations of arginine and aliphatic residues (Table S3, Supporting Information, and

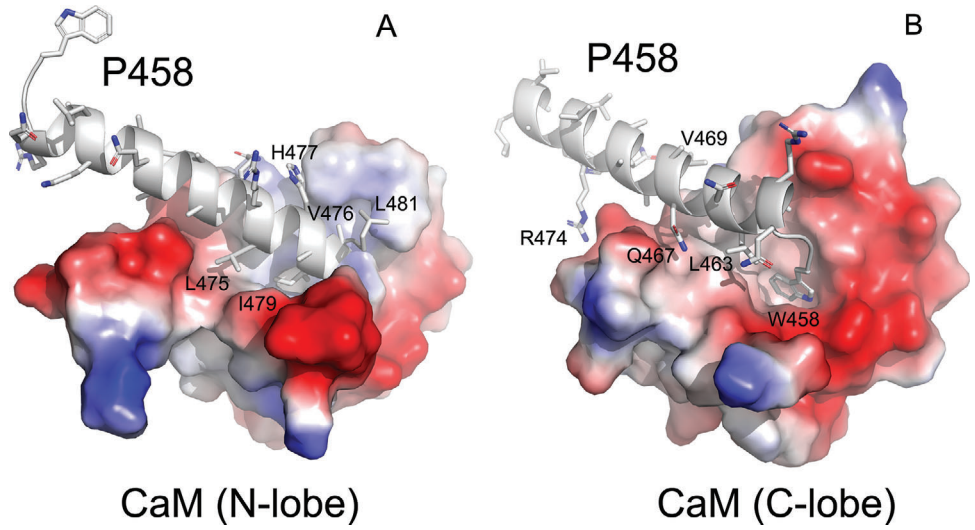

Figure 3. P458:CaM interactions. Close views of the molecular contacts between P458 and the panel A) N and panel B) C lobes of CaM (pdb 6YNU). The peptide is shown in cartoon representation and colored in grey. Side chains of key residues interacting with CaM are shown as sticks. These residues establish numerous non-polar interactions, as well as several hydrogen bonds with CaM residues. These contacts are summarized in Table S5B,C, Supporting Information.The CaM lobes are represented by their electrostatic surfaces (negative and positive charges are colored in red and blue, respectively).

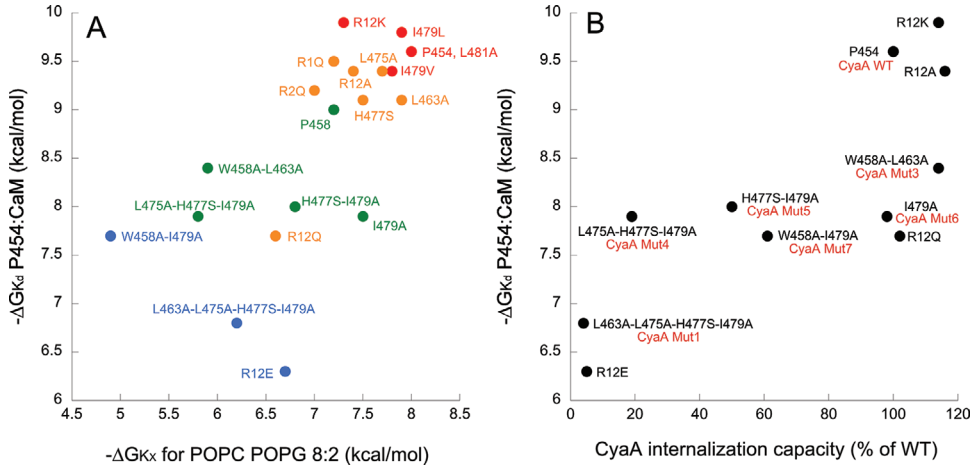

Figure 4. Correlations between in vitro properties of P454-derived peptides and the internalization activity of the CyaA recombinant proteins. A) The free energy values of peptide:CaM complex formation (ΔG_{Kd}) are plotted as a function of free energy values for peptide solution-to-membrane partitioning (ΔG_{Kx}, see Table S3, Supporting Information) and permeabilization efficiency ($Cp_{1/2}$ values, see Table S9, Supporting Information). The color code refers to the $Cp_{1/2}$ values ranging from red-to-blue (high-to-low permeabilization efficiency, respectively) using a logarithmic scale (red: $Cp_{1/2} < 100$ nM, orange: $0.1 < Cp_{1/2} < 1$ μM, green: $1 < Cp_{1/2} < 10$ μM, and blue: $10 < Cp_{1/2} < 100$ μM. B) The free energy values of peptide:CaM complex formation (ΔG_{Kd}) as a function of relative internalization activity of the CyaA variants (data from Table 1). The peptide names are in black and the names of the recombinant CyaA proteins are in red, if different from the peptide name. Each dot reported on plots corresponds to the average value of at least three independent replicates (see Table 1; Tables S3 and S9, Supporting Information). The r^2 values for the data of panels (A) and (B) are 0.54 and 0.62, respectively.

Figure 4A) with a progressive decrease with the single point mutations L475A, R474Q, H477S, L463A and I479A or with the reduction of the side chain apolarity of the I479 residue (i.e., I479L, I479V, and I479A). These results confirm the contribution of these residues in the complex formation as suggested from the observation of the peptide:CaM crystal structure (Figure 3A).

As expected, the affinity of the P454-derived peptides for CaM is affected to a greater extent by multiple mutations. In particular, the double substitution of both arginine residues R461 and R474 (R*12*) into either glutamine or glutamate residues (R*12*Q and R*12*E peptides respectively) resulted in both cases in a significant loss of affinity for CaM. Substitutions of aliphatic and histidine residues at the C-terminus of P454 (H477S-I479A and L475A-H477S-I479A) resulted in ≈20-fold decrease of affinity of P454 for CaM, while the mutation of the N-terminal aromatic and aliphatic residues (W458A-L463A) results in only a 4-fold

Table 1. Cytotoxic activities of the recombinant CyaA proteins. The binding and internalization of CyaA and different variants were assayed on sheep erythrocytes as described in the Experimental Section. The proteins in 6M urea were directly diluted (to a final concentration of 5.6 nM) in sheep erythrocyte suspensions in buffer B. Bound and internalized AC activities for each recombinant protein is expressed as % of that measured with the wild-type CyaA toxin and represent the average values of at least three independent measurements. The substituted residues are indicated in bold letters for each CyaA variants.

Proteins	Sequence of the 454–484 region of CyaA recombinant proteins	Cell-bound AC activity [% of wt]	Internalized AC activity [% of wt]	Number of replicates
CyaAwt	ASAHWGQRALQGAQAVAAAQRLVHAIALMTQ	100	100	17
$CyaA_{Mut1}$	-------**E**-**A**----------**EA**-**S**-**A**-----	96 ± 24	4 ± 2	5
$CyaA_{R12E}$	-------**E**------------**E**----------	106 ± 28	3 ± 3	9
$CyaA_{R12Q}$	-------**Q**------------**Q**----------	107 ± 36	102 ± 7	3
$CyaA_{R12A}$	-------**A**------------**A**----------	112 ± 18	112 ± 7	3
$CyaA_{R12K}$	-------**K**------------**K**----------	110 ± 17	114 ± 19	3
$CyaA_{Mut2}$	---------**A**-----------**A**-**S**-**A**-----	112 ± 17	4 ± 3	6
$CyaA_{Mut3}$	----**A**----**A**----------	94 ± 9	106 ± 13	3
$CyaA_{Mut4}$	----------**A**-**S**-**A**-----	110 ± 19	15 ± 6	8
$CyaA_{Mut5}$	----------**S**-**A**-----	113 ± 10	72 ± 12	5
$CyaA_{Mut6}$	----------**A**-----	97 ± 33	99 ± 7	3
$CyaA_{Mut7}$	----**A**----------**A**-----	107 ± 34	62 ± 7	5

decrease in P454:CaM affinity (Table S3, Supporting Information). These observations are in agreement with the crystal structure of P458:CaM, showing that the residue H477, and more importantly I479, from the C-terminal part of P454 are crucial for P454:CaM interactions (Figure 3A). The W458 substitution also seems to be involved in CaM binding as its combination with I479 (W458A-I479A) induces a significant loss in affinity (Table S3, Supporting Information, and Figure 3B). Taken together, the mutational analysis (Table S3, Supporting Information), the HDX-MS data (Figure 2F), and the crystal structures of the complex (Figure 3) indicate that the C-terminal part of the peptide strongly interacts with the N-terminal lobe of CaM and, to a lesser extent, the N-terminal part of the peptide interacts with the C-terminal lobe of CaM.

We then characterized the membrane binding and permeabilization properties of P454-derived peptides. We analyzed the membrane-induced secondary structure changes of the peptides by circular dichroism (Figure S12 and Table S8, Supporting Information) and also determined their partition coefficient, K_X, and free energy of membrane interaction, ΔG_{Kx}, using fluorescence spectroscopy and ITC (Figure 4A; and Table S3, Supporting Information). The secondary structure content of the P454-derived peptides is characterized by a disorder-to-helical conformation transition upon membrane binding for most peptides. The ΔG_{Kx} values indicate that membrane interaction of P454-derived peptides is affected by mutations of arginine, aliphatic, and aromatic residues. Notably, a strong correlation is observed between the free energy values of P454-derived peptides for membrane interaction and CaM binding (Figure 4A). We also measured the membrane permeabilization efficiency of the P454-derived peptides, reported as the peptide concentration required for recovering 50% of ANTS fluorescence intensity upon permeabilization ($Cp_{1/2}$ values, see Table S9, Supporting Information). We color-coded the $Cp_{1/2}$ values ranging from red-to-blue (high-to-low permeabilization efficiency, respectively) using a logarithmic scale (see legend of Figure 4A for details). As observed for P454 membrane partitioning, the $Cp_{1/2}$ values show a good correlation with the free energy of P454:CaM complex formation (Figure 4A). These results show that the three properties of P454-derived peptides (K_d, K_X, and $Cp_{1/2}$) are correlated, that is, any mutation affecting one of the parameters will likely affect the other two. Altogether, these data indicate that the biophysical properties of P454 required to interact and destabilize membranes are highly similar to that involved in CaM binding: the peptide must adopt an amphipathic helical conformation with positively charged and apolar residues to exert these three activities in vitro.

2.5. Characterization of Recombinant CyaA Toxins Harboring Mutations in the P454 Region

To explore whether the interaction of the P454 region with membrane and CaM is also involved in CyaA intoxication, we designed several recombinant toxins harboring specific modifications at the key residues identified above (R461 and R474, W458, H477, and aliphatic residues L463, L475, and I479) (Figure S13, Supporting Information) and characterized their cytotoxic activities (**Table 1**). The recombinant toxins were produced in *Escherichia coli* and purified to homogeneity (Figure S14, Supporting Information), and their capacities to bind to and translocate their AC domain across the plasma membrane were determined on sheep erythrocytes, a model of target cells (Table 1). In the first recombinant CyaA tested, $CyaA_{Mut1}$, six residues from the P454 region were modified: the arginine residues R461 and R474 were changed to glutamate, the leucine L463 and L475 and the isoleucine I479 to alanine, and the histidine residue H477 to serine. These combined modifications did not affect binding of $CyaA_{Mut1}$ to cells but completely abolished translocation of its catalytic domain into the cytosol. This result provides direct evidence that the P454 region is absolutely critical for the invasive activity of the toxin, i.e., , AC translocation into the target cell cytosol.

We then further delineated the respective contribution of these different residues to the cytotoxic properties of CyaA. We first examined the contribution of the arginine residues R461 and R474 to cell intoxication. Charge reversion of these two arginine residues by glutamate residues in $CyaA_{R\,12E}$ was enough to fully abolish the ability of CyaA to invade cells while not affecting toxin binding to plasma membrane (Table 1). However, the substitution of the guanidinium group of the two arginine residues by lysine residues in $CyaA_{R\,12K}$, as well as the neutralization of the arginine residues in $CyaA_{R\,12Q}$ and the deletion of the arginine side chain in $CyaA_{R\,12A}$, did not significantly affect the invasive activities of the corresponding toxins (Table 1). The contribution of the neutral and apolar residues in P454 region to CyaA internalization was evaluated in a second series of recombinant modified toxins, $CyaA_{Mut2}$ to $CyaA_{Mut7}$. The $CyaA_{Mut2}$ variant harboring the 4 mutations L463A, L475A, H477S, and I479A, was also completely unable to invade erythrocytes (Table 1). The modified toxin $CyaA_{Mut4}$, which harbors only 3 mutations L475A, H477S, and I479A at the C-terminus of P454, was also drastically impaired in translocation capability. The other recombinant toxin that was significantly altered in its invasion activity was $CyaA_{Mut7}$ carrying the double mutation W458A and I479A and showing about 60% of wild-type translocation activity. Notably, the binding of all these toxins to erythrocytes was not altered, indicating that the specific modifications introduced into the recombinant CyaA proteins did not affect the cell-binding step, but selectively affected the translocation step. Taken together, these results suggest that the ability of the P454 motif to associate with CaM within the target cell is critical for the efficient translocation of the AC domain across the membrane. This is further supported by the correlation between the cytotoxic activity of the CyaA recombinant proteins (data from Table 1) and the affinity of the corresponding P454-derived peptides (data from Table S3, Supporting Information) shown in Figure 4B.

2.6. Cytosolic CaM is Required for Efficient CyaA Internalization

The above cell intoxication data (Table 1 and Figure 4B) suggest that the ability of the P454 motif to bind CaM inside target cells might contribute to the translocation of the AC domain across membrane. To test this hypothesis, we analyzed the effects of a CaM inhibitor, calmidazolium (CDZ), which exhibits a high affinity (K_I about 10–50 nM) for holo-CaM.[71] For these experiments, erythrocytes were first incubated in the presence of calcium at 4 °C in conditions that allow the toxin to bind to the cell membrane but not to translocate across membranes, as originally described by Rogel and Hanski.[52] After washing of unbound toxin, a rapid (within minutes) internalization of the catalytic domain was observed upon transfer of the samples to 37 °C (**Figure 5**). However, when CDZ (10 μM) was added to the cell mixture just prior to the temperature shift from 4 to 37 °C, the amount of internalized AC was drastically reduced (Figure 5).

The inhibitory CDZ concentration (10 μM) is in excess over the total intracellular CaM concentration, estimated to be between 3 to 7 μM[72,73] of which up to 10% should be free.[74] In the presence of CDZ, the free CaM in erythrocytes should drop to low nM ranges, i.e., 1–10 nM (assuming a binding constant for CDZ:CaM of 10–50 nM). This free CaM concentration is enough for binding

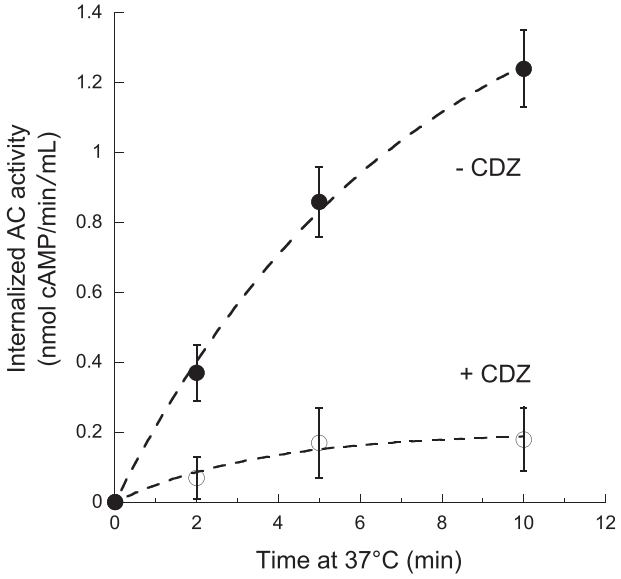

Figure 5. Calmidazolium (CDZ) inhibits CyaA translocation into erythrocytes. Erythrocytes were first incubated with CyaA (5.6 nM) at 4 °C in the presence of $CaCl_2$ for 30 min so that the toxin could bind to cells but not translocate across plasma membrane (see main text). After removal of unbound toxin, 10 μM CDZ were added (open symbols) or not (CyaA, filled symbols) and the cell mixtures were transferred to 37 °C. At the indicated time, the cell suspensions were treated with trypsin for 10 min and after addition of soybean trypsin inhibitor, cells were washed and lysed with 0.1% Tween 20 and the internalized AC activity (i.e., enzyme activity protected from trypsin digestion) was measured as described in Experimental Section. Each dot corresponds to the average value of three independent replicates.

and activation of AC (Figure S15, Supporting Information), given the very high AC:CaM affinity (K_d about 0.1 nM) but is well below the affinity constant of P454:CaM (K_d about 90 nM). Size exclusion chromatography experiments confirm that CDZ can specifically inhibit CaM association with P454, but not with the AC domain (Figure S16, Supporting Information). In agreement, the H:CaM complex (K_d about 10 nM; Figure S7 and Table S4, Supporting Information) is partially inhibited by CDZ (Figure S16, Supporting Information). Notably, it was previously shown that CaM binding to the catalytic domain of CyaA was not required for toxin internalization.[75] Taken together, we conclude that CDZ blocks CyaA internalization into the cells primarily by preventing CaM binding to the P454 motif. We propose that trapping of the CyaA polypeptide chain by cytosolic CaM via the P454 segment may facilitate the entry of the N-terminal AC domain into the cells.

3. Discussion

We demonstrate here the critical role of the P454 peptide segment (residues 454–484) in the translocation of the catalytic domain of CyaA across the plasma membrane of target cells, and suggest a new mechanism for CyaA invasion. We have previously shown that a deletion of the whole translocation domain TD (residues 373–485) hindered the entry of CyaA into target cells.[12] In the present work, we show that substitutions of a few residues within the P454 segment are sufficient to fully abrogate

the delivery of the AC domain into the cell cytoplasm, without impairing toxin binding to target cells. Most importantly, the mutated residues that result in inactivation of CyaA translocation are also involved in two key properties of the P454 motif: first, its ability to bind to membranes and destabilize the lipid bilayer, as reported previously[54,56] and corroborated here using various P454-derived peptides; and secondly, its ability to bind with high affinity to holo-CaM, as shown here for the first time. We propose that these two properties are directly implicated in the process of CyaA translocation across the plasma membrane of eukaryotic target cells.

The P454 peptide exhibits characteristics found in many calmodulin-binding peptides that form amphiphilic helices upon association with CaM. We have shown by a combination of biophysical approaches that P454 forms a 1:1 complex with CaM in a calcium-dependent manner, with a K_d of about 90 nM at 25 °C (Figures S2–S5 and Tables S1–S3, Supporting Information). We solved the crystal structures of P454 (actually a slightly shorter peptide, P458, exhibiting similar properties) in complex with holo-CaM, and obtained structural models in solution by SEC-SAXS measurements, which revealed the dynamics and the overall shape of the P454:CaM complex (Figure 2,3; and Figure S9, Supporting Information). Together with HDX-MS data, these studies have revealed the original mode of association of P454 with CaM, which primarily occurs via several interactions between the C-terminal moiety of the peptide and the hydrophobic groove of N-terminal domain of CaM. Comparison of the structural and dynamic characteristics of the P454:CaM complex with those of CaM with MLCK peptide or H peptide (the main CaM-binding site of the AC domain) illustrates the remarkable plasticity of CaM in binding to target proteins. These structural data also indicated key residues of P454 that could be potentially important in CaM-binding (Figure 3). The implication of these amino-acids in CaM was experimentally confirmed by analysis of P454-derived peptides with modified residues (Figure 4). In particular, modification of the two positively charged Arg residues into Glu resulted in a drastic decrease in CaM-binding affinity. Multiple mutations of aliphatic residues L463, L475, I479 to alanine, and histidine residue H477 to serine, also lead to a significant decrease in CaM-binding affinity.

Combining these mutations differently affected binding to CaM, as well as to the membrane itself (Figure 4A). In all cases, the affinity values of P454 and P454-derived peptides for CaM were 2–3 orders of magnitude higher than that for membranes, i.e., with dissociation constants in the nM range and μM ranges, respectively (Table S3, Supporting Information). Consequently, P454 preferentially interacts with calmodulin over membranes. Moreover, we demonstrate by using a droplet interface bilayers (DIB) technique that P454 can translocate across a lipid bilayer and that holo-CaM favors its accumulation in the *trans* compartment (Figure 1). In contrast, the passage of the fluorescent-$P454_{R12E}$ peptide could not be detected unless very high CaM concentrations were loaded in *trans* droplets to overcome the low affinity of this peptide for CaM ($K_d^{CaM} \approx 20$ μM). Taken together, these data suggest that the P454 peptide is capable of translocating across lipid membranes. Moreover, once translocated, the peptide is able to form a complex with CaM. This interaction displaces the P454 peptide from the membrane to form a peptide:CaM complex in solution due to a favorable free energy difference (Figures S4 and S8, Supporting Information). The C-terminal part of P454 strongly interacts with the N-CaM lobe via the arginine and apolar residues of the peptide (Figure 3).

The cell intoxication data (Table 1) indicate that the ability of CyaA to translocate its catalytic domain across the membrane of target cells is strongly correlated with both membrane permeabilization efficiency of the P454 motif and its affinity for CaM (Figure 4). We propose that after binding of CyaA to target cells, the translocation region interacts with the plasma membrane and the P454 motif locally destabilizes it, leading to calcium influx.[41] The negative potential across the membrane may then favor the passage of the positively charged P454 region through the lipid bilayer to reach the cytoplasmic side of the membrane where it can associate with holo-CaM. Binding to a cytosolic partner would strongly increase the entropic pulling force by preventing the backward movement of the polypeptide chain across the plasma membrane. This strong interaction between the P454 motif and CaM in the cytosol may then favor the translocation of the catalytic domain across the plasma membrane. Collectively, we propose that the membrane destabilization caused by P454, followed by its translocation and binding to calmodulin, are essential to convert the stochastic process of protein translocation into an efficient vectorial chain transfer into the cytoplasm of host cells, in a process akin to that of chaperones (e.g., BiP) grabbing polypeptides as they exit from the translocon to facilitate their translocation.[76]

To evaluate the contribution of P454:CaM complex formation to the AC translocation process into cells, we analyzed the effects of a CaM inhibitor, calmidazolium (CDZ), which exhibits a high affinity for calmodulin.[71] We found that CDZ selectively blocks AC internalization into cells and we provide evidence that CDZ primarily interferes with CaM binding to the P454 motif of CyaA, without altering CaM association with the catalytic domain and activation of its enzymatic activity (Figure 5; Figures S15 and S16, Supporting Information).

In summary, our results indicate that CaM plays a dual role in CyaA intoxication: first, it acts as a cytosolic binder that can grab the polypeptide chain by the P454 motif to favor the translocation of the catalytic domain across the plasma membrane of target cells; second, after entry of the catalytic domain into the cell, CaM can associate with the AC domain to activate its enzymatic activity by stabilizing active conformations of the catalytic site.[10,11] This illustrates a remarkable parsimony in the molecular mechanism of the CyaA toxin which exploits the same ubiquitous and abundant protein, CaM, to enable two essential functions, entry and activation, that are both required for an effective intoxication of eukaryotic cells. Interestingly, we demonstrated in a prior study that CyaA can efficiently translocate across a biomimetic membrane model made of a tethered lipid bilayer (tBLM) assembled over an amine-gold surface derivatized with CaM.[19] Remarkably, in this synthetic system, CaM is the only eukaryotic component needed for translocation of the CyaA catalytic domain. This observation nicely fits with the present results indicating that CaM may play the dual function of both cytosolic binder and activator of CyaA.

Interestingly, several toxins hijack eukaryotic cytosolic factors to achieve the translocation of their respective catalytic domains: these toxins contain segments able to translocate across target membranes and to interact with host soluble proteins.[77–91] We

propose that the formation of such toxin:target complexes significantly contributes to the energy required to achieve the translocation of bacterial toxin catalytic domains across membranes of eukaryotic cells.

4. Experimental Section

The Experimental Section is available in the Supporting Information.

Supporting Information

Supporting Information is available from the Wiley Online Library or from the author.

Acknowledgements

A.V., M.S., D.P.O'B., and P.G. contributed equally to this work. A.V. was supported by a DIM MalInf grant from the region Ile-de-France. M.S. was supported by the Pasteur – Paris University (PPU) International PhD Program. D.P.O.B. was supported by Institut Pasteur (grants PasteurInnoV15006-01A and PTR451). P.G. was supported by Sorbonne Université. The authors acknowledge SOLEIL and ESRF for provision of synchrotron radiation facilities. The authors thank the staffs of the DISCO, PROXIMA-1, and SWING beamlines for constant support and help during data collection (Synchrotron SOLEIL, St Aubin, France) and MASSIF (Synchrotron ESRF, Grenoble, France) beamlines for assistance during the X-ray diffraction data collection. Funding is acknowledged from Agence Nationale de la Recherche (grant number CACSICE Equipex ANR-11-EQPX-0008). Region Ile de France (grant number DIM MalInf 2016), CNRS (UMR 3528), Institut Pasteur (grant numbers PasteurInnoV15006-01A, PTR451 and PTR166-19, PPUIP program). The funders have no role in study design, data collection and analysis, decision to publish, or preparation of the manuscript.

Conflict of Interest

The authors declare no conflict of interest.

Data Availability Statement

All relevant HDX-MS, X-ray and small-angle X-ray scattering (SAXS) data are available in the Supporting Information. The crystal structures have been deposited on the protein data bank (PDB) with the access codes 6YNU and 6YNS. The molecular model and experimental SAXS data have been deposited on SASBDB (Small Angle Scattering Biological Data Bank), http://www.sasbdb.org/aboutSASBDB/) under the SAS code SASDJ64 (calcium-bound calmodulin) and SASDJ74 (P454 peptide from *B. pertussis* CyaA toxin complexed with calmodulin).

Keywords

adenylate cyclase, *Bordetella pertussis*, calmodulin, CyaA toxin, membrane translocation, protein membrane interaction, protein–protein interactions

Received: September 23, 2020
Revised: December 10, 2020
Published online:

[1] N. Guiso, *Toxins* **2017**, *9*, 277.
[2] J. Novak, O. Cerny, A. Osickova, I. Linhartova, J. Masin, L. Bumba, P. Sebo, R. Osicka, *Toxins* **2017**, *9*, 300.
[3] J. G. Coote, *FEMS Microbiol. Rev.* **1992**, *8*, 137.
[4] I. Linhartova, L. Bumba, J. Masin, M. Basler, R. Osicka, J. Kamanova, K. Prochazkova, I. Adkins, J. Hejnova-Holubova, L. Sadilkova, J. Morova, P. Sebo, *FEMS Microbiol. Rev.* **2010**, *34*, 1076.
[5] A. Chenal, A. C. Sotomayor Perez, D. Ladant, in *The Comprehensive Sourcebook of Bacterial Protein Toxins*, 4th ed. (Eds: J. Alouf, D. Ladant, M. R. Popoff), Elsevier, Amsterdam, Netherlands **2015**.
[6] R. Benz, *Biochim. Biophys. Acta* **2016**, *1858*, 526.
[7] D. Ladant, A. Ullmann, *Trends Microbiol.* **1999**, *7*, 172.
[8] J. C. Karst, V. Y. Ntsogo Enguene, S. E. Cannella, O. Subrini, A. Hessel, S. Debard, D. Ladant, A. Chenal, *J. Biol. Chem.* **2014**, *289*, 30702.
[9] Q. Guo, Y. Shen, Y. S. Lee, C. S. Gibbs, M. Mrksich, W. J. Tang, *EMBO J.* **2005**, *24*, 3190.
[10] J. C. Karst, A. C. Sotomayor Perez, J. I. Guijarro, B. Raynal, A. Chenal, D. Ladant, *Biochemistry* **2010**, *49*, 318.
[11] D. P. O'Brien, D. Durand, A. Voegele, V. Hourdel, M. Davi, J. Chamot-Rooke, P. Vachette, S. Brier, D. Ladant, A. Chenal, *PLoS Biol.* **2017**, *15*, e2004486.
[12] J. C. Karst, R. Barker, U. Devi, M. J. Swann, M. Davi, S. J. Roser, D. Ladant, A. Chenal, *J. Biol. Chem.* **2012**, *287*, 9200.
[13] O. Knapp, E. Maier, J. Masin, P. Sebo, R. Benz, *Biochim. Biophys. Acta* **2008**, *1778*, 260.
[14] M. Basler, O. Knapp, J. Masin, R. Fiser, E. Maier, R. Benz, P. Sebo, R. Osicka, *J. Biol. Chem.* **2007**, *282*, 12419.
[15] E. M. Barry, A. A. Weiss, I. E. Ehrmann, M. C. Gray, E. L. Hewlett, M. S. Goodwin, *J. Bacteriol.* **1991**, *173*, 720.
[16] M. Hackett, L. Guo, J. Shabanowitz, D. F. Hunt, E. L. Hewlett, *Science* **1994**, *266*, 433.
[17] G. D. Westrop, E. K. Hormozi, N. A. Da Costa, R. Parton, J. G. Coote, *Gene* **1996**, *180*, 91.
[18] D. P. O'Brien, S. E. Cannella, A. Voegele, D. Raoux-Barbot, M. Davi, T. Douche, M. Matondo, S. Brier, D. Ladant, A. Chenal, *FASEB J.* **2019**, *33*, 10065.
[19] R. Veneziano, C. Rossi, A. Chenal, J. M. Devoisselle, D. Ladant, J. Chopineau, *Proc. Natl. Acad. Sci. U. S. A.* **2013**, *110*, 20473.
[20] T. Rose, P. Sebo, J. Bellalou, D. Ladant, *J. Biol. Chem.* **1995**, *270*, 26370.
[21] P. Glaser, H. Sakamoto, J. Bellalou, A. Ullmann, A. Danchin, *EMBO J.* **1988**, *7*, 3997.
[22] R. A. Welch, *Curr. Top. Microbiol. Immunol.* **2001**, *257*, 85.
[23] O. Knapp, E. Maier, G. Polleichtner, J. Masin, P. Sebo, R. Benz, *Biochemistry* **2003**, *42*, 8077.
[24] C. Martin, M. A. Requero, J. Masin, I. Konopasek, F. M. Goni, P. Sebo, H. Ostolaza, *J. Bacteriol.* **2004**, *186*, 3760.
[25] C. Bauche, A. Chenal, O. Knapp, C. Bodenreider, R. Benz, A. Chaffotte, D. Ladant, *J. Biol. Chem.* **2006**, *281*, 16914.
[26] A. Chenal, J. I. Guijarro, B. Raynal, M. Delepierre, D. Ladant, *J. Biol. Chem.* **2009**, *284*, 1781.
[27] A. C. Sotomayor Perez, J. C. Karst, M. Davi, J. I. Guijarro, D. Ladant, A. Chenal, *J. Mol. Biol.* **2010**, *397*, 534.
[28] A. Chenal, J. C. Karst, A. C. Sotomayor Perez, A. K. Wozniak, B. Baron, P. England, D. Ladant, *Biophys. J.* **2010**, *99*, 3744.
[29] A. C. Sotomayor-Perez, D. Ladant, A. Chenal, *J. Biol. Chem.* **2011**, *286*, 16997.
[30] A. C. Sotomayor-Perez, O. Subrini, A. Hessel, D. Ladant, A. Chenal, *J. Am. Chem. Soc.* **2013**, *135*, 11929.
[31] A. C. Sotomayor-Perez, D. Ladant, A. Chenal, *Toxins* **2015**, *7*, 1.
[32] D. P. O'Brien, B. Hernandez, D. Durand, V. Hourdel, A. C. Sotomayor-Perez, P. Vachette, M. Ghomi, J. Chamot-Rooke, D. Ladant, S. Brier, A. Chenal, *Sci. Rep.* **2015**, *5*, 14223.
[33] L. Bumba, J. Masin, P. Macek, T. Wald, L. Motlova, I. Bibova, N. Klimova, L. Bednarova, V. Veverka, M. Kachala, D. I. Svergun, C. Barinka, P. Sebo, *Mol. Cell* **2016**, *62*, 47.
[34] D. P. O'Brien, A. C. S. Perez, J. Karst, S. E. Cannella, V. Y. N. Enguene, A. Hessel, D. Raoux-Barbot, A. Voegele, O. Subrini, M. Davi, J. I.

Guijarro, B. Raynal, B. Baron, P. England, B. Hernandez, M. Ghomi, V. Hourdel, C. Malosse, J. Chamot-Rooke, P. Vachette, D. Durand, S. Brier, D. Ladant, A. Chenal, *Toxicon* **2018**, *149*, 37.
[35] L. Motlova, N. Klimova, R. Fiser, P. Sebo, L. Bumba, *J. Mol. Biol.* **2020**, *432*, 5696.
[36] S. E. Cannella, V. Y. Ntsogo Enguene, M. Davi, C. Malosse, A. C. Sotomayor Perez, J. Chamot-Rooke, P. Vachette, D. Durand, D. Ladant, A. Chenal, *Sci. Rep.* **2017**, *7*, 42065.
[37] P. Guermonprez, N. Khelef, E. Blouin, P. Rieu, P. Ricciardi-Castagnoli, N. Guiso, D. Ladant, C. Leclerc, *J. Exp. Med.* **2001**, *193*, 1035.
[38] P. Guermonprez, C. Fayolle, M. J. Rojas, M. Rescigno, D. Ladant, C. Leclerc, *Eur. J. Immunol.* **2002**, *32*, 3071.
[39] M. El-Azami-El-Idrissi, C. Bauche, J. Loucka, R. Osicka, P. Sebo, D. Ladant, C. Leclerc, *J. Biol. Chem.* **2003**, *278*, 38514.
[40] J. Masin, M. Basler, O. Knapp, M. El-Azami-El-Idrissi, E. Maier, I. Konopasek, R. Benz, C. Leclerc, P. Sebo, *Biochemistry* **2005**, *44*, 12759.
[41] R. Fiser, J. Masin, M. Basler, J. Krusek, V. Spulakova, I. Konopasek, P. Sebo, *J. Biol. Chem.* **2007**, *282*, 2808.
[42] A. Chenal, D. Ladant, *Toxins* **2018**, *10*, 386.
[43] C. Angely, N. M. Nguyen, S. A. Dias, E. Planus, G. Pelle, B. Louis, M. Filoche, A. Chenal, D. Ladant, D. Isabey, *Biol. Cell.* **2017**, *109*, 293.
[44] S. Hasan, N. N. Kulkarni, A. Asbjarnarson, I. Linhartova, R. Osicka, P. Sebo, G. H. Gudmundsson, *Infect. Immun.* **2018**, *86*, 1.
[45] J. Roderova, A. Osickova, A. Sukova, G. Mikusova, R. Fiser, P. Sebo, R. Osicka, J. Masin, *Sci. Rep.* **2019**, *9*, 5758.
[46] C. Angely, D. Ladant, E. Planus, B. Louis, M. Filoche, A. Chenal, D. Isabey, *PLoS One* **2020**, *15*, e0228606.
[47] L. Bumba, J. Masin, R. Fiser, P. Sebo, *PLoS Pathog.* **2010**, *6*, e1000901.
[48] K. B. Uribe, A. Etxebarria, C. Martin, H. Ostolaza, *PLoS One* **2013**, *8*, e67648.
[49] A. Voegele, D. P. O'Brien, O. Subrini, N. Sapay, S. E. Cannella, V. Y. N. Enguene, A. Hessel, J. Karst, V. Hourdel, A. C. S. Perez, M. Davi, R. Veneziano, J. Chopineau, P. Vachette, D. Durand, S. Brier, D. Ladant, A. Chenal, *Pathog. Dis.* **2018**, *76*, 1.
[50] H. Sakamoto, J. Bellalou, P. Sebo, D. Ladant, *J. Biol. Chem.* **1992**, *267*, 13598.
[51] J. Vojtova, J. Kamanova, P. Sebo, *Curr. Opin. Microbiol.* **2006**, *9*, 69.
[52] A. Rogel, E. Hanski, *J. Biol. Chem.* **1992**, *267*, 22599.
[53] A. S. Otero, X. B. Yi, M. C. Gray, G. Szabo, E. L. Hewlett, *J. Biol. Chem.* **1995**, *270*, 9695.
[54] O. Subrini, A. C. Sotomayor-Perez, A. Hessel, J. Spiaczka-Karst, E. Selwa, N. Sapay, R. Veneziano, J. Pansieri, J. Chopineau, D. Ladant, A. Chenal, *J. Biol. Chem.* **2013**, *288*, 32585.
[55] J. Masin, A. Osickova, A. Sukova, R. Fiser, P. Halada, L. Bumba, I. Linhartova, R. Osicka, P. Sebo, *Sci. Rep.* **2016**, *6*, 29137.
[56] A. Voegele, O. Subrini, N. Sapay, D. Ladant, A. Chenal, *Toxins* **2017**, *9*, 369.
[57] A. Sukova, L. Bumba, P. Srb, V. Veverka, O. Stanek, J. Holubova, J. Chmelik, R. Fiser, P. Sebo, J. Masin, *Biochim. Biophys. Acta, Biomembr.* **2020**, *1862*, 183310.
[58] N. B. Last, D. E. Schlamadinger, A. D. Miranker, *Protein Sci.* **2013**, *22*, 870.
[59] J. G. Li, J. J. Koh, S. P. Liu, R. Lakshminarayanan, C. S. Verma, R. W. Beuerman, *Front. Neurosci.* **2017**, *11*, 73.
[60] M. H. Cardoso, B. T. Meneguetti, B. O. Costa, D. F. Buccini, K. G. N. Oshiro, S. L. E. Preza, C. M. E. Carvalho, L. Migliolo, O. L. Franco, *Int. J. Mol. Sci.* **2019**, *20*, 1.
[61] R. D. Brokx, M. M. Lopez, H. J. Vogel, G. I. Makhatadze, *J. Biol. Chem.* **2001**, *276*, 14083.
[62] A. Villarroel, M. Taglialatela, G. Bernardo-Seisdedos, A. Alaimo, J. Agirre, A. Alberdi, C. Gomis-Perez, M. V. Soldovieri, P. Ambrosino, C. Malo, P. Areso, *J. Mol. Biol.* **2014**, *426*, 2717.
[63] F. Liu, X. Chu, H. P. Lu, J. Wang, *Proc. Natl. Acad. Sci. U. S. A.* **2017**, *114*, E3927.
[64] H. Bayley, B. Cronin, A. Heron, M. A. Holden, W. L. Hwang, R. Syeda, J. Thompson, M. Wallace, *Mol. BioSyst.* **2008**, *4*, 1191.
[65] C. N. Johnson, F. Potet, M. K. Thompson, B. M. Kroncke, A. M. Glazer, M. W. Voehler, B. C. Knollmann, A. L. George, Jr., W. J. Chazin, *Structure* **2018**, *26*, 683.
[66] D. P. O'Brien, S. Brier, D. Ladant, D. Durand, A. Chenal, P. Vachette, *Biotechnol. Appl. Biochem.* **2018**, *65*, 62.
[67] A. Fiser, R. K. G. Do, A. Sali, *Protein Sci.* **2000**, *9*, 1753.
[68] G. Evrard, F. Mareuil, F. Bontems, C. Sizun, J. Perez, *J. Appl. Crystallogr.* **2011**, *44*, 1264.
[69] O. Rudenko, A. Thureau, P. Perez, *Evolutionary refinement of the 3D structure of multi-domain protein complexes from small angle X-ray scattering data*, **2019**.
[70] D. P. O'Brien, V. Hourdel, A. Chenal, S. Brier, *Expression, Purification, and Structural Biology of Membrane Proteins* (Eds: C. Perez, T. Maier), Methods in Molecular Biology Series, Humana, New York, NY **2020**, pp. 677–718.
[71] R. Dagher, C. Briere, M. Feve, M. Zeniou, C. Pigault, C. Mazars, H. Chneiweiss, R. Ranjeva, M. C. Kilhoffer, J. Haiech, *Biochim. Biophys. Acta, Mol. Cell Res.* **2009**, *1793*, 1068.
[72] S. Kakiuchi, S. Yasuda, R. Yamazaki, Y. Teshima, K. Kanda, R. Kakiuchi, K. Sobue, *J. Biochem.* **1982**, *92*, 1041.
[73] J. A. Cox, M. Comte, E. A. Stein, *Proc. Natl. Acad. Sci. U. S. A.* **1982**, *79*, 4265.
[74] D. J. Black, Q. K. Tran, A. Persechini, *Cell Calcium* **2004**, *35*, 415.
[75] N. Heveker, D. Ladant, *Eur. J. Biochem.* **1997**, *243*, 643.
[76] K. E. S. Matlack, B. Misselwitz, K. Plath, T. A. Rapoport, *Cell* **1999**, *97*, 553.
[77] E. Lemichez, M. Bomsel, G. Devilliers, J. vanderSpek, J. R. Murphy, E. V. Lukianov, S. Olsnes, P. Boquet, *Mol. Microbiol.* **1997**, *23*, 445.
[78] R. Ratts, H. Zeng, E. A. Berg, C. Blue, M. E. McComb, C. E. Costello, J. C. vanderSpek, J. R. Murphy, *J. Cell Biol.* **2003**, *160*, 1139.
[79] G. Haug, J. Leemhuis, D. Tiemann, D. K. Meyer, K. Aktories, H. Barth, *J. Biol. Chem.* **2003**, *278*, 32266.
[80] R. Ratts, C. Trujillo, A. Bharti, J. vanderSpek, R. Harrison, J. R. Murphy, *Proc. Natl. Acad. Sci. U. S. A.* **2005**, *102*, 15635.
[81] A. G. Tamayo, A. Bharti, C. Trujillo, R. Harrison, J. R. Murphy, *Proc. Natl. Acad. Sci. U. S. A.* **2008**, *105*, 5254.
[82] E. Kaiser, S. Pust, C. Kroll, H. Barth, *Cell. Microbiol.* **2009**, *11*, 780.
[83] C. Trujillo, J. Taylor-Parker, R. Harrison, J. R. Murphy, *Mol. Microbiol.* **2010**, *76*, 1010.
[84] L. Dmochewitz, M. Lillich, E. Kaiser, L. D. Jennings, A. E. Lang, J. Buchner, G. Fischer, K. Aktories, R. J. Collier, H. Barth, *Cell. Microbiol.* **2011**, *13*, 359.
[85] E. Kaiser, C. Kroll, K. Ernst, C. Schwan, M. Popoff, G. Fischer, J. Buchner, K. Aktories, H. Barth, *Infect. Immun.* **2011**, *79*, 3913.
[86] E. Kaiser, N. Bohm, K. Ernst, S. Langer, C. Schwan, K. Aktories, M. Popoff, G. Fischer, H. Barth, *Cell. Microbiol.* **2012**, *14*, 1193.
[87] A. E. Lang, K. Ernst, H. Lee, P. Papatheodorou, C. Schwan, H. Barth, K. Aktories, *Cell. Microbiol.* **2014**, *16*, 490.
[88] L. Schnell, L. Dmochewitz-Kuck, P. Feigl, C. Montecucco, H. Barth, *Toxicon* **2016**, *116*, 23.
[89] M. Schuster, L. Schnell, P. Feigl, C. Birkhofer, K. Mohr, M. Roeder, S. Carle, S. Langer, F. Tippel, J. Buchner, G. Fischer, F. Hausch, M. Frick, C. Schwan, K. Aktories, C. Schiene-Fischer, H. Barth, *Sci. Rep.* **2017**, *7*, 613.
[90] K. Ernst, J. Schmid, M. Beck, M. Hagele, M. Hohwieler, P. Hauff, A. K. Uckert, A. Anastasia, M. Fauler, T. Jank, K. Aktories, M. R. Popoff, C. Schiene-Fischer, A. Kleger, M. Muller, M. Frick, H. Barth, *Sci. Rep.* **2017**, *7*, 1.
[91] H. Burress, A. Kellner, J. Guyette, S. A. Tatulian, K. Teter, *J. Biol. Chem.* **2019**, *294*, 12122.
[92] R. Chattopadhyaya, W. E. Meador, A. R. Means, F. A. Quiocho, *J. Mol. Biol.* **1992**, *228*, 1177.

ADVANCED SCIENCE
Open Access

Supporting Information

for *Adv. Sci.*, DOI: 10.1002/advs.202003630

A High-Affinity Calmodulin-Binding Site in the CyaA Toxin Translocation Domain is Essential for Invasion of Eukaryotic Cells

Alexis Voegele, Mirko Sadi, Darragh Patrick O'Brien, Pauline Gehan, Dorothée Raoux-Barbot, Maryline Davi, Sylviane Hoos, Sébastien Brûlé, Bertrand Raynal, Patrick Weber, Ariel Mechaly, Ahmed Haouz, Nicolas Rodriguez, Patrice Vachette, Dominique Durand, Sébastien Brier, Daniel Ladant,* and Alexandre Chenal*

Supplementary Information for manuscript: A high-affinity calmodulin-binding site in the CyaA toxin translocation domain is essential for invasion into eukaryotic cells

Alexis Voegele, Mirko Sadi, Darragh P O'Brien, Pauline Gehan, Dorothée Raoux-Barbot, Maryline Davi, Sylviane Hoos, Sébastien Brûlé, Bertrand Raynal, Patrick Weber, Ariel Mechaly, Ahmed Haouz, Nicolas Rodriguez, Patrice Vachette, Dominique Durand, Sébastien Brier, Daniel Ladant, Alexandre Chenal

The Supplementary information file contains the materials and methods section, Tables S1 to S9, Figures S1 to S16, and the supplementary references.

Materials

1-palmitoyl-2-oleoyl-sn-glycero-3-phosphocholine (POPC, reference 850457C), 1-palmitoyl-2-oleoyl-sn-glycero-3-[phospho-rac-(1-glycerol)] (POPG, reference 840457C) were purchased from Avanti Polar Lipids (Alabaster, AL, USA). ANTS (A-350, 8-aminonapthalene-1,3,6 trisulfonic acid), and DPX (X-1525, p-xylene-bis-pyridinium bromide) were purchased from Molecular Probes (Eugene, OR, USA). Squalene, TPCK-treated trypsin, and soybean trypsin inhibitor were from Sigma-Aldrich. Calmidazolium chloride was purchased from Calbiochem.

Buffers used in this study

Experiments were performed using these 5 buffers:

Buffer A: 20 mM HEPES, 150 mM NaCl pH 7.4

Buffer B: 20 mM HEPES, 150 mM NaCl, 2 mM $CaCl_2$ pH 7.4

Buffer C: 20 mM HEPES, 150 mM NaCl, 4 mM $CaCl_2$ pH 7.4

Buffer D: 20 mM HEPES, 150 mM NaCl, 8 mM $MgCl_2$, 2 mM $CaCl_2$, pH 7.4

Buffer E: 20 mM HEPES, 150 mM NaCl, 9.8 mM $MgCl_2$, 0.2 mM $CaCl_2$, pH 7.4

Peptides synthesis

The P454 peptide corresponds to residues 454 to 484 of the CyaA toxin (ASAHWGQRALQGAQAVAAAQRLVHAIALMTQ) and contains a single native tryptophan W458. The P454-derived peptides were produced and purified by Genosphere Biotechnologies (Paris, France). All peptides were capped on the N-terminus with an acetyl group and on the C-terminus with an amide group, except for the P458 peptide (uncapped N-terminus). Their molecular weight was determined by MALDI-TOF and purity analyzed by HPLC.

The sequences of P454-derived peptides are as follows:

- P454 L463A corresponds to the substitution of L463 by an alanine: ASAHWGQRA**A**QGAQAVAAAQRLVHAIALMTQ.

- P454 L475A corresponds to the substitution of L475 by an alanine: ASAHWGQRALQGAQAVAAAQR**A**VHAIALMTQ.

- P454 L481A corresponds to the substitution of L481 by an alanine: ASAHWGQRALQGAQAVAAAQRLVHAIA**A**MTQ.

- P454 I479L, I479V and I479A correspond to the substitution of I479 by a leucine, a valine or an alanine, respectively:

ASAHWGQRALQGAQAVAAAQRLVHA**L**ALMTQ

ASAHWGQRALQGAQAVAAAQRLVHA**V**ALMTQ

ASAHWGQRALQGAQAVAAAQRLVHA**A**ALMTQ.

- P454 H477S corresponds to the substitution of H477 by a serine: ASAHWGQRALQGAQAVAAAQRLV**S**AIALMTQ.

- P454 H477S-I479A corresponds to the substitution of H477 by a serine and I479 by an alanine: ASAHWGQRALQGAQAVAAAQRLV**S**A**A**ALMTQ.

- P454 W458A-I479A corresponds to the substitution of both W458 and I479 by an alanine: ASAH**A**GQRALQGAQAVAAAQRLVHA**A**ALMTQ.

- P458 peptide corresponds to a shorter P454 peptide, from residue 458 to 481: WGQRALQGAQAVAAAQRLVHAIAL.

- P454 L463A-L475A-H477S-I479A corresponds to the substitution of L463, L475 and I479 by an alanine and H477 by a serine: ASAHWGQRA**A**QGAQAVAAAQR**A**V**S**A**A**ALMTQ.

- P454 W458A-L463A corresponds to the substitution of both W458 and L463 by an alanine: ASAH**A**GQRA**A**QGAQAVAAAQRLVHAIALMTQ.

- P454 L475A-H477S-I479A corresponds to the substitution of both L475 and I479 by an alanine and H477 by a serine: ASAHWGQRALQGAQAVAAAQR**A**V**S**A**A**ALMTQ.

The two arginine residues R461 (referred as R_1) or R474 (referred as R_2), or both of them (referred as R_{12}) were substituted by glutamine (R_1Q, R_2Q and R_{12}Q), alanine (R_{12}A), lysine (R_{12}K) or glutamate (R_{12}E) residues [1], yielding the following sequences:

P454 R_1Q: ASAHWGQ**Q**ALQGAQAVAAAQRLVHAIALMTQ

P454 R_2Q: ASAHWGQRALQGAQAVAAAQ**Q**LVHAIALMTQ

P454 R_{12}Q: ASAHWGQ**Q**ALQGAQAVAAAQ**Q**LVHAIALMTQ

P454 R_{12}A: ASAHWGQ**A**ALQGAQAVAAAQ**A**LVHAIALMTQ

P454 R_{12}K: ASAHWGQ**K**ALQGAQAVAAAQ**K**LVHAIALMTQ

P454 R_{12}E: ASAHWGQ**E**ALQGAQAVAAAQ**E**LVHAIALMTQ

The P454, P454 R_{12}E and H-helix (corresponding to residues 233-254 of CyaA) peptides were also synthetized with a 5-carboxytetramethylrhodamine (TAMRA) linked to their N-terminus and capped at the C-terminus with an amide group for the droplet interface bilayer experiments.

Production and purification of proteins used in this study

Human Calmodulin (CaM)

CaM was produced in *E. coli* and purified as previously described [2-4]. Briefly, CaM was precipitated with ammonium sulfate followed by a glacial acetic acid precipitation. Then, CaM was purified as follows: a first HIC on Phenyl Sepharose (EDTA-CaM), an IEC on Q-Sepharose fast flow, a second HIC on Phenyl Sepharose (calcium-CaM) and a SEC on Sephacryl S100. Protein concentration was determined by spectrophotometry (ε_{280nm} = 2,980 M^{-1} cm^{-1}).

CyaA recombinant proteins

All the CyaA recombinant proteins were produced in *E. coli* BLR. The *E. coli* strain XL1-Blue (Stratagene, California) was used for DNA manipulation and *in vitro* DNA manipulations were performed according to standard protocols [5].

The expression vector used for the wild-type and modified CyaA proteins is derived from plasmid pT7CACT1 ([6], kind gift from Peter Sebo). In a first step, we constructed pCACTw11 in which the CyaA coding region located between the unique BstBI and NcoI sites of pT7CACT1 was replaced, with the Gibson technique [7], using the NEBuilder® HiFi DNA Assembly Cloning Kit from New England Biolabs, USA) by a synthetic DNA fragment (DLTw11, Figure S13, obtained from Twist Bioscience, USA) encoding the native CyaA sequence with *E. coli* optimized codons and harboring several unique restriction sites flanking the P454 region (Figure S13). Plasmid pCACTw11 expresses the native, acylated, and fully functional CyaA toxin. Plasmid pCACTw16, that expresses the modified protein $CyaA_{Mut1}$, was constructed similarly by HiFi subcloning between the BstBI and NcoI sites of a synthetic DNA fragment (DLTw16, Figure S13) encoding a mutated CyaA sequence with six modified residues in the P454 region (R461E, L463A, R474E, L475A, H477S and I479A). Plasmids encoding the CyaA mutants $CyaA_{R12E}$, $CyaA_{R12Q}$, $CyaA_{R12A}$, $CyaA_{R12K}$, $CyaA_{Mut6}$, and $CyaA_{Mut7}$, were constructed by HiFi subcloning between the BstBI and HindIII sites of

pCACTw11 (or pCACTw16) of synthetic DNA fragments (obtained from Twist Bioscience) encoding the CyaA sequences with appropriate codon changes. Plasmids encoding the CyaA mutants $CyaA_{Mut2,}$ $CyaA_{Mut3,}$ $CyaA_{Mut4,}$ and $CyaA_{Mut5}$ were constructed by HiFi subcloning between the BstBI and HindIII sites of pCACTw11 (or pCACTw16) of PCR-amplified fragments with synthetic oligonucleotides (obtained from Sigma-Aldrich) designed to introduce the appropriate codon changes. All DNA sequences of recombinant plasmids were verified by DNA sequencing (performed by Eurofins, France). Further details of plasmid construction and sequence can be provided upon request.

The wild-type and modified recombinant CyaA proteins were produced and purified as previously described [8-10]. Briefly, inclusion bodies were resuspended overnight in 8 M urea, 20 mM HEPES. Proteins were purified on two consecutive IEC (Q-Sepharose fast flow and Q-Sepharose Hi-Performance) equilibrated with 6 M urea, 20 mM HEPES, 150 mM NaCl, pH 7.4. Proteins were eluted with a NaCl gradient. Proteins were further purified onto a HIC Phenyl-Sepharose column. Proteins were eluted with 6 M urea, 20 mM HEPES, pH 7.4. Finally, proteins were loaded on a Sephacryl S500 equilibrated with 6 M urea, 20 mM HEPES, 50 mM NaCl, pH 7.4. Proteins were concentrated on Amicon 50 kDa. Protein concentration was determined by spectrophotometry (ε_{280} = 144,000 M^{-1} cm^{-1}). The primary sequence of the WT CyaA is displayed in Figure S1 and the sequences with the substituted residues in the P454 region of the CyaA mutants are listed in Table 1.

Lipid vesicles preparation

Small unilamellar vesicles (SUVs) and large unilamellar vesicles (LUVs) were prepared with POPC and POPG at a molar ratio of 8:2, at a lipid concentration of 10 mM in buffer A, as previously described [1]. Briefly, SUVs and LUVs were prepared by reverse phase evaporation and filtered through polycarbonate filters of 1 μm and 0.2 μm of pore size diameter to obtain LUV. SUVs were further sonicated. The hydrodynamic diameters and mean net charge of the vesicles were measured by dynamic light scattering (DLS) and electrophoretic mobility, respectively, using a ZetaSizer NanoZS (Malvern Pananalytical, Orsay, France) [11].

Peptide titrations by SUVs and CaM followed by tryptophan fluorescence

Titrations were carried out with a FP-8200 Jasco spectrofluorimeter, equipped with a Peltier-thermostated ETC-272T at 25°C. A bandwidth of 5 nm was used for both excitation and emission beams. Fluorescence experiments were carried out in a 109.004F-QS cuvette (Hellma, France) with constant stirring. Fluorescence emission was recorded between 300 and

400 nm at a scan rate of 100 nm/min, with an excitation wavelength of 280 nm. Fluorescence emission spectra were corrected for SUV or CaM baselines. Fluorescence intensity ratio at 330 nm over 370 nm was used to measure the partition coefficient (K_X) of peptides between the solution and membranes [1, 12] and the affinity (K_d) of peptides for CaM [13].

Determination of partition coefficient K_X and dissociation constant K_d from experimental data

The partition coefficient K_X is defined as the ratio of protein in the lipid (P_L) and in buffer (P_W) phases [12, 14], expressed by: $K_X = \frac{\frac{[P_L]}{[L]}}{\frac{[P_W]}{[W]}}$, giving $\frac{[P_W]}{[P_L]} = \frac{[W]}{K_X[L]}$, where [W] the concentration of water (55.5 M) and [L] the lipid concentration.

The fraction of peptide partitioned into the membrane, f_{PL}, is equal to:

$f_{P_L} = \frac{[P_L]}{[P_T]} = \frac{[P_L]}{[P_L]+[P_W]} = \frac{1}{1+(\frac{[P_W]}{[P_L]})} = \frac{1}{1+(\frac{[W]}{[L]K_X})}$, where P_T is the total concentration of peptides $[P_T] = [P_L] + [P_W]$.

The dissociation constant, K_d, is obtained from titration experiments of the P454-derived peptides by CaM and is expressed as follows: $K_d = \frac{[P]*[CaM]}{[P{:}CaM]}$, given $\frac{K_d}{[CaM]} = \frac{[P]}{[P{:}CaM]}$ and the fraction of complex, $f_{P:CaM}$, is: $f_{P:CaM} = \frac{[P{:}CaM]}{[P{:}CaM]+[P]} = \frac{1}{1+\frac{[P]}{[P:CaM]}} = \frac{1}{1+\frac{K_d}{[CaM]}}$.

The equations are fitted to the experimental data using the KaleidaGraph software, providing the K_X and K_d values. The partition coefficient is related to the apparent dissociation constant: $K_X \times K_d = [W]$ and to the free energy of partition $\Delta G_{Kx} = -RT\ln(K_X)$, where ΔG is the free energy in kcal/mol, R the gas constant ($R = 1.98 \times 10^{-3}$ kcal/mol/K) and T the temperature in Kelvin. The free energy of peptide CaM interaction, ΔG_{Kd}, is given by $\Delta G_{Kd} = RT\ln(K_d)$.

Sedimentation velocity-Analytical ultracentrifugation (SV-AUC)

SV-AUC experiments were carried out in a ProteomeLab XL-I analytical ultracentrifuge (Beckman Coulter, Brea, CA, USA). Samples of 400 µL and 410 µL of buffer were loaded in cells equipped with 12-mm thick double-sector epoxy centerpieces and sapphire windows. P454 and CaM were tested alone (at 57 µM and 72 µM, respectively) or mixed in a molar ratio 1:1 (at 70 µM each). Samples were incubated 2h at 20°C in the ultracentrifuge and, then span at 42,000 rpm in an An-50 Ti rotor. Detection of protein concentration as a function of radial position and time was monitored with the ProteomeLab software (Beckman Coulter,

Brea, CA, USA) by both absorbance at 280 nm and interferometry. Four hundred scans were collected at 3-min intervals with a radial step size of 0.003 cm. SV scans were analyzed using the continuous size distribution model c(s) of the software Sedfit [15]. All the c(s) distributions were calculated with a fitted frictional ratio f/f0 and a maximum entropy regularization procedure with a confidence level of 0.68. All partial specific volumes were theoretically calculated with the software Sednterp (Spin Analytical, Berwick, ME, USA). Buffer density and viscosity at 20°C of 1.0310 $g.mL^{-1}$ and 1.0061 cP respectively were also determined with Sednterp for buffer B.

Isothermal titration calorimetry

ITC experiments were performed using a VP-ITC calorimeter (Malvern Panalytical, Orsay, France). The ITC experiments were performed in buffer B or buffer A complemented with 2 mM EDTA. For a typical titration, the solution of analyte (ranging from 0.2 to 10 μM) was loaded in the reaction cell. The titrants (ranging from 4 to 430 μM) were loaded into the syringe and then the titrant was injected into the reaction cell, usually at intervals ranging from 200 to 600 seconds. Heats of dilutions were measured by injecting the titrant into the protein-free buffer, and were subtracted from the heat of reaction. To obtain the thermodynamic parameters ΔH, ΔS and ΔG, titration profiles were analyzed using the single- or two-site models with Origin7 software (OriginLab). Changes of heat capacity (ΔCp) for the P454:CaM complex formation was obtained from the slope of ΔH values versus temperature. ITC experiments were performed at 10, 20, 25, 30 and 38°C.

Synchrotron Radiation Circular Dichroism

Synchrotron radiation circular dichroism (SRCD) was performed on the DISCO beamline of the synchrotron SOLEIL (Saint-Aubin, France). Spectra were recorded at 25°C with an integration time of 1.2 s and a bandwidth of 1 nm with a resolution of 1 nm. A far-UV spectrum represents the average of four individual scans. QS cells (Hellma, France) with a pathlength of 20, 50, 100 or 200 μm (depending on final protein concentrations) were used to record spectra in the far-UV range (from 190 to 250 nm). CD spectra of peptides and proteins were measured in buffers A and B, 20% of trifluoroethanol (TFE), in the presence of SUVs (POPC:POPG 8:2) or CaM. Secondary structure content was estimated using Bestsel software [16, 17].

Membrane permeabilization

To monitor membrane permeabilization induced by peptides, ANTS (fluorophore probe) and DPX (quencher) were encapsulated into large unilamellar vesicles (LUVs). The LUVs were prepared at a concentration of 10 mM lipid at a POPC:POPG molar ratio of 8:2 containing 20 mM ANTS and 60 mM DPX. The multilamellar vesicle suspension was extruded through 0.4- and 0.2 μm polycarbonate filters to produce LUVs. The unencapsulated ANTS and DPX were removed by gel filtration with a 5 mL Sephadex G-25 column (GE Healthcare Life Sciences). For permeabilization assays, LUVs were incubated in buffer A at 0.45 mM lipid concentration at 25°C in a 101-QS cuvette (Hellma, France) and under constant stirring. The excitation wavelength was set at 390 nm and the emission of ANTS was continuously measured at 515 nm. The maximum intensity of permeabilization, corresponding to the maximum recovery of ANTS fluorescence, was measured after addition of 0.1% of Triton X100. The concentration of membrane-bound peptides required to induce the recovery of half intensity of the ANTS fluorescence ($C_{P1/2}$) was extracted from the permeabilization intensity as a function of peptide concentration [1].

Membrane permeabilization with CaM and EDTA

LUVs were incubated in buffer B at a lipid concentration of 0.45 mM. P454 was added at a concentration inducing vesicle permeabilization. After a few seconds of permeabilization, holo-CaM was added to the solution at a peptide:CaM molar ratio of 1:3. EDTA was subsequently added in excess to chelate calcium and convert holo-CaM to apo-CaM.

Cell intoxication assays

Toxin binding and translocation into sheep erythrocytes were assayed essentially as described previously [18]. The CyaA proteins were diluted from the urea stock solutions to a final concentration of 5.6 nM (1 μg/mL) into sheep erythrocytes (5 x 10^8 cells/mL, from Charles River Laboratories, Wilmington, MA, USA) in buffer A or in buffer B complemented with 2 mM EDTA, and incubated at 30°C for 20 min. An aliquot was taken to measure the total adenylate cyclase (AC) activity that (measured in the presence of 1 μgM CaM at 30°C and pH 8.0, as described in [18]). The cell suspensions were chilled on ice and centrifuged at 4°C. The pelleted cells were resuspended in buffer A and separated into two different batches. One was centrifuged again and pelleted cells were lysed with 0.1% Tween 20. The measured enzymatic activity corresponds to the toxin bound to the cells and was expressed as a percentage of total activity added to the cells. The second batch was digested with 20 μg of

TPCK-treated trypsin (Millipore Sigma, Burlington, MA, USA) for 10 min at 30°C to digest the adenylate cyclase that remained at the external surface of the erythrocytes. A 5-fold excess of soybean trypsin inhibitor was added and cells were washed with buffer A and lysed with 0.1% Tween 20. The activity protected from trypsin digestion corresponds to the internalized toxin. Activities are expressed as percentages of total toxin added to the erythrocytes (taken as 100%) and represent average values from at least three independent measurements. One unit of CyaA activity corresponds to 1 μmol of cAMP formed per min at 30°C and pH 8.0. The bound and internalized AC activities measured with the CyaA recombinant proteins were normalized to that of the WT CyaA toxin.

For the CyaA intoxication experiments in the presence of calmidazolium (CDZ), in order to minimize the cell exposure to this potent CaM inhibitor, we performed a two-step intoxication assay as described originally by Rogel and Hanski [19]. For this, the erythrocytes (5 x 10^8 cells/mL) were in a first step incubated with CyaA (1 μg/mL, 5.6 nM) in buffer A plus 2 mM $CaCl_2$ at 4 °C for 30 min. In these conditions, the toxin can bind to the cell membrane but cannot translocate across membrane [19]. The unbound toxin was removed by extensive washing in buffer A at 4 °C. An aliquot was kept in ice for measuring bound activity (that amounted to about 0.8 to 1.5% ot total CyaA activity, 5 separate experiments). The cells were then resuspended in cold buffer A plus 2 mM $CaCl_2$ and split in two fractions. CDZ (10 μM) was added to one fraction that was further incubated at 4 ° C for 1-2 min to allow diffusion and cell penetration of the drug, and then both fractions were transferred to 37 °C. At 2, 5, and 10 min, aliquots of cell suspension were withdrawn and mixed with trypsin as above for 10 min at 30°C. After addition of soybean trypsin inhibitor, the cells were washed with buffer A then lysed with 0.1% Tween 20 and the internalized AC activity protected from trypsin digestion was measured and expressed as a percentage of bound AC activity. Importantly, CDZ (10 μM) has no inhibitory effect on the enzymatic activity when assayed in the presence of 1 μM CaM (see Figure S15).

Size exclusion chromatography of P454, H and AC364 with CaM in the presence of CDZ

The SEC experiments were performed on a TSKgel G3000SW 7.5 mm ID * 30 cm - column equilibrated in buffer B at a flow rate of 0.6 mL/min at RT. The elution profiles were measured by absorbance at 280 nm, conductivity and by tryptophan fluorescence on a FP750 fluorometer (Ex.: 280 nm; Em.: 340 nm; bandwidths 10/10 nm) equipped with a on-line cell. Tryptophan fluorescence is used for the SEC profiles because this allows monitoring the tryptophan-containing CaM ligands, i.e., P454, H and AC364, while CaM provides only a

weak fluorescence signal. CDZ alone loaded at 40 uM in the SEC does not contribute to the fluorescence signal. The samples were prepared at the following final concentrations: 10 µM of peptides (P454 and H) and AC364, 15 µM of CaM and 40 µM of CDZ. The initial concentration of CDZ was 14.5 mM in 100% DMSO. Addition of CDZ at a final concentration of 40 µM gives a final concentration of less than 0.3 % of DMSO in the samples containing CDZ.

Peptide translocation followed by droplet interface bilayer experiments

An aqueous phase is prepared with buffer D or E and the oil phase is prepared with 15 % (v/v) of chloroform and 0.08 % (w/v) of lipids (POPC:POPG at a 9:1 molar ratio) in squalene. A population of droplets is obtained by adding 2 µL of the aqueous phase to 20 µL of the oil phase before briefly shaking the mixture to create an invert emulsion. Two droplet populations were prepared: one containing the TAMRA-labeled peptide in buffer D, the "source", *cis*-droplets and the other one containing buffer D or E, or in the presence or in the absence of calmodulin, the "capture", *trans*-droplets. The two droplet populations were deposited successively on a glass slide (covered with a thin layer of polydimethylsiloxane, PDMS), which allows their mixing and the random formation of pairs of droplets. A lipid bilayer is thus formed at the interface between the two adhering droplets. We then track the possible translocation of the TAMRA-labeled peptides through this bilayer. The fluorescence signals of the "source" and the "capture" droplets were monitored by epifluorescence microscopy for 15 minutes with an Olympus microscope and a MicroMax camera (Princeton Instrument). Fluorescent probes were excited by illumination with a mercury lamp with an excitation filter (515-555 nm).

Image analysis

Quantification of the translocation process is possible thanks to the analysis of the fluorescence images of the droplet pairs. Even if fluorescence is not directly proportional to peptide concentration due to photo-bleaching and small volume variations, one can hypothesize that the fluorescence intensities of the "source" and the "capture" droplets are proportional to the ratio of their concentrations. Moreover, as the initial concentration in the "source" droplet is known and as the total amount of peptide is conserved during the experience, we can write that: $C_s(t=0) \times V_s = C_s(t) \times V_s + C_c(t) \times V_c$, where C_i is the concentration of the droplet i, V_i its volume, which was determined from microscopy images (i="s" for the source droplet and "c" for the capture droplet). We can thus estimate C_c, the concentration of the "capture" droplet at any time as:

$$C_c = \frac{C_s(t=0) \times V_s}{V_c + \frac{V_s \times F_s}{F_c}}$$

where F_i is the fluorescence intensity measured for droplet i.

For each experiment, background fluorescence was subtracted from the fluorescence of the droplet pair. Furthermore, during experiments we observed that a certain amount of peptide was able to exit the droplets, reaching the oil phase and possibly go back inside another droplet. To take into account this amount of peptide that could go inside the "capture" droplet without crossing the bilayer, we performed all experiments with a control droplet, or "dark" droplet, initially peptide-free and we subtracted its fluorescence from the one of the "capture" droplet of the pair so that the remaining fluorescence increase of the capture droplet was from translocation through the bilayer only and not contaminated by the oil-mediated peptide diffusion phenomenon.

Small angle X-ray scattering (SAXS)

Data acquisition

X-ray scattering data were collected at the SWING beamline of the SOLEIL Synchrotron (Saint-Aubin, France). All measurements were performed using a size-exclusion HPLC column on-line with the SAXS measuring cell, a 1.5 mm diameter quartz capillary contained in an evacuated vessel [20]. All experimental details are given in Table S5 in accordance with the guidelines given in [21].

We studied solutions of CaM in the presence of a 2-fold excess of P454. All proteins were analyzed in buffer C. Scattering of the elution buffer before void volume was recorded and used as buffer scattering for subtraction from all protein patterns. For each frame, the protein concentration (about 0.6/2 mg/mL at the top of elution peak for CaM-P454 and CaM respectively) was estimated from UV absorption at 280 nm using a spectrometer located immediately upstream of the SAXS measuring cell. We also studied the P458:CaM complex in solution. Due to low sample concentration, the recorded SAXS data were of much lower quality, sufficient however to appear essentially identical to that of the P454:CaM complex.

Data analysis

SAXS data were normalized to the intensity of the incident beam and background subtracted using the programs FoxTrot (courtesy of SWING beamline) and Primus (https://www.embl-hamburg.de/biosaxs/primus.html) [22]. Identical frames under the main elution peak were selected using Cormap [23] and averaged for further analysis. The radius of gyration (R_g) was

evaluated using the Guinier approximation [24] and also derived from the distance distribution function P(r) calculated by the program GNOM [25]. Two independent molecular masses M estimates were obtained using the SAXSMoW2 and ScÅtter programs available at the URLs http://saxs.ifsc.usp.br/ and https://bl1231.als.lbl.gov/scatter/, respectively. Both mass determinations do not depend on the value of the protein concentration c, a feature of particular interest in the case of CaM containing samples since CaM does not possess any tryptophan.

Ab initio shape determination

The shape or envelope of the complex of CaM with P454 peptide was determined using the *ab initio* program DAMMIF [26]. 20 runs yielded as many shapes that were compared using the DAMAVER suite of routines based on the calculation of the Normalized Spatial Discrepancy (NSD) that is lower than 0.7 if all 20 models are similar. The final envelope is obtained using DAMMIN [27] that uses the envelope of all superimposed DAMMIF models (the union of all models) as initial volume.

Rigid-body modeling

SAXS models of the P454:CaM complex were obtained from the crystal structures by using the DADIMODO modeling program [28] that uses an all-atom description of the molecule and explores conformational space by random modifications of the internal degrees of freedom ϕ and ψ angles within the helix between the two domains of CaM.

The molecular model and experimental SAXS data have been deposited on SASBDB (Small Angle Scattering Biological Data Bank, http://www.sasbdb.org/aboutSASBDB/) under the SAS code SASDJ64 (calcium-bound calmodulin) and SASDJ74 (P454 peptide from *B. pertussis* CyaA toxin complexed with calmodulin).

Crystallography

Crystallization and diffraction data collection

To obtain crystals suitable for X-ray diffraction studies, we used the procedure and the crystallization pipeline implemented in the medium-scale crystallography platform at the Institut Pasteur, Paris [29]. Briefly, crystallization screening trials of calmodulin in complex with different peptides (molar ratio 1:2) were carried out by the sitting drop vapor-diffusion method with a Mosquito automated nanoliter dispensing system (TTP Labtech, Melbourn, UK) at 291K. Sitting drops of 400 nL were set up in Greiner plates for 672 commercially available screening solutions using a 1:1 mixture of protein sample and reservoir well solution (150 µL). The plates were stored in a RockImager (Formulatrix, Bedford, USA) automated

imaging system to monitor crystal growth. Manual optimizations of the different obtained hits were performed in Linbro plates with the hanging-drop method by mixing 2 µl of protein with 2 µl of reservoir solution. The best crystals were obtained with the conditions shown in Table S5A. For data collection, the crystals were flash-cooled in liquid nitrogen using a condition of crystallization supplemented by 30% (v/v) of glycerol as a cryoprotectant. The X-ray diffraction data were collected on beamline PROXIMA-1 (Synchrotron SOLEIL, St Aubin, France) or on beamline MASIFF (Synchrotron ESRF, Grenoble, France) and processed with autoPROC (Global Phasing Ltd.) [30].

Structure determination and model refinement

The crystal structures of the calmodulin in complex with the synthetic P458 peptide were solved by the molecular replacement technique using separately, the N-ter and C-ter lobes of calmodulin (from the PDB entry 1CTR) as search models with program Phaser [31]. Peptides were manually traced into Fourier difference electron density maps. Final models of the complexes were obtained through interactive cycles of manual model building with Coot [32] and reciprocal space refinement with Buster [33]. X-ray data collection and model refinement statistics are summarized in Table S5. Figures showing the crystallographic model were generated and rendered with Pymol (Schrodinger, LLC). The atomic coordinates and structure factors of the CaM-P458 complexes have been deposited in the RCSB Protein Data Bank under the accession codes 6YNU (C2221 form) and 6YNS (P212121 form).

HDX-MS analysis

A summary of the Hydrogen/Deuterium eXchange – Mass Spectrometry (HDX-MS) experiments is provided in Table S7.

Biological samples

In order to determine the effect of P454 binding on CaM, the labeling was performed on CaM alone, and in the presence of a two-fold molar excess P454. HDX-MS experiments were carried out in buffer B, *i.e.*, in the presence of 2 mM $CaCl_2$. The quality of each protein and peptide was assessed prior to labeling by intact mass measurement (data not shown).

Sample preparation for HDX-MS

The P454:CaM complex was formed by mixing 10 µL of P454 (20 µM in buffer B) with 10 µL of CaM solution (10 µM in buffer B). The labeling control (*i.e.,* CaM alone) was prepared by replacing the P454 solution by 10 µL of buffer B. Prior to addition of the deuterated buffer B (99.98% D_2O in 20 mM HEPES, 150 mM NaCl, 2 mM $CaCl_2$, pD 7.4), all solutions were equilibrated for 1 h at room temperature. Continuous labeling was initiated at 20˚C by adding

80 µL of deuterated buffer (80% final excess deuterium). Considering a K_d of 90 nM and a 1 to 1 binding stoichiometry, 92.3% of CaM remains bound to P454 during labeling. The exchange reaction was quenched after 0.16, 1, 10, 30, 60 and 120 min by mixing 14 µL of the labeling reaction (*i.e.,* 14 pmoles of CaM) with 56 µL of quench buffer (0.6% formic acid) maintained at 4 ˚C to achieve a final pH of 2.5. Quenched samples were immediately snap-frozen in liquid nitrogen and stored at -80 ˚C. Triplicate labelling experiments were performed for each time point and condition for all HDX-MS analyses (independent technical replicates).

Data acquisition

HDX-MS analyses were performed with the aid of an HDX manager (Waters Corporation) maintained at 0 ºC. Prior to mass analysis, samples were rapidly thawed and 50 µL were digested for 2 min at 20 ºC using an in-house prepared column (2.0 x 20 mm, 66 µL bead volume) of immobilized pepsin beads (Thermo Scientific). Peptides were trapped, concentrated and desalted using a VanGuard™ CSH C18 pre-column (1.7 µm, 2.1 x 5 mm; Waters), and separated using an ACQUITY UPLC™ CSH C18 column (1.7 µm, 1 x 100 mm). Labeled peptides were eluted with an 8 min gradient of 5-30% acetonitrile at 40 µL/min and 0°C. After each run, the pepsin column was manually cleaned with two consecutive washes of 1.5% formic acid, 5% acetonitrile, 1.5 M guanidinium chloride, pH 1.6. Blank injections were performed after each sample to confirm the absence of carry-over.

The LC flow was directed to a Synapt™ G2-Si HDMS™ mass spectrometer (Waters Corporation) equipped with a standard electrospray ionization source (ESI). Mass accuracy was ensured by continuously infusing a Glu-1-Fibrinogen solution (100 fmol/µL in 50% acetonitrile, 0.1% formic acid) through the reference probe of the ESI source at a flow rate of 2.5 µL/min. Mass spectra were acquired in positive-ion and resolution mode over the 50–1950 *m/z* range. Peptides were identified in undeuterated samples using a combination of data-independent acquisition scheme (MS^E; trap collision energy ramp: 15.0 to 45.0 V) and exact mass measurement (<5.0 ppm mass error) using the same chromatographic settings than for the deuterated samples.

Data processing

Peptide maps were generated by database searching in ProteinLynx Global Server 3.0 (Waters Corporation, Milford, MA) using the following processing and workflow parameters: low and elevated intensity thresholds set to 100.0 and 50.0 counts; intensity threshold sets to 750.0 counts; automatic peptide and fragment tolerance; non-specific primary digest reagent; false discovery rate sets to 4%. Each fragmentation spectrum was manually inspected for

assignment confirmation. Peptide map were refined in DynamX 3.0 (Waters Corporation, Milford, MA) using the following Import PLGS results filter: minimum intensity = 3000; minimum products per amino acid value = 0.4; minimum consecutive products = 1; minimum sum intensity for products = 1000; minimum score = 7; maximum MH+ error = 5 ppm. DynamX 3.0 HDX software (Waters Corporation, Milford, MA) was used to extract the centroid masses of all peptides selected for local HDX-analyses; only one charge state was considered per peptide. No adjustment was made for back-exchange and the results are reported as relative deuterium exchange levels expressed in either mass unit or fractional exchange. Fractional exchange data was calculated by dividing the experimentally measured uptake by the theoretically maximum number of exchangeable backbone amide hydrogens that could be replaced into each peptide (taking into account the final excess of deuterium present in the labeling mixture). MEMHDX was used to visualize and statistically validate HDX results (Wald test, false discovery rate sets to 5%) [34].

Statistical Analysis

2D-SAXS data were radially averaged, normalized to the intensity of the incident beam and put on an absolute scale using the scattering from water [35] before buffer scattering subtraction. All these operations were performed using the programs FoxTrot (courtesy of SWING beamline) and Primus (https://www.embl-hamburg.de/biosaxs/primus.html) [22]. The resulting 1D scalar scattering intensity profiles are represented by the normalized intensities and their associated standard deviations (SD). Identical frames under the main elution peak were selected using Cormap [23] and averaged for further analysis. The agreement between experimental data and calculated intensities from models was evaluated using the reduced χ^2 metric [22].

X-ray data collection, processing and model refinement statistics corresponding to the X-ray structures are summarized in Table S5. The software packages used are autoPROC, Phaser, Coot, Buster and Pymol, as described in the Crystallography section.

Concerning the experiments of peptide translocation followed by droplet interface bilayer experiments, the *cis* and *trans* droplet populations were successively deposited on a glass slide, which allowed their mixing and the random formation of pairs of droplets. Four to seven independent trials, i.e., pairs of *cis* and *trans* droplets, were conducted for each condition and represented as dots on boxplots in Figures 1 and S6. Distributions of conditions were compared with the non-parametric Mann-Whitney test. The level of significance was set

at 5% (ns: $p > 0.05$, *: $p < 0.05$ and **: $p < 0.01$). Boxplots and statistical analyses were performed with R software (https://www.r-project.org/) and the ggplot2 package (https://ggplot2.tidyverse.org/).

The statistical analysis for the HDX-MS experiments is described below. A summary of the HDX-MS experiments is provided in Table S7 and in the HDX-MS analysis section. Pre-processing of data: one unique charge state was considered per peptide (user selection). The quality determination of the dataset was accomplished by MEMHDX (PCA plots) (http://memhdx.c3bi.pasteur.fr) to evaluate the agreement across replicates. Data presentation: Logit representation is used for Figure S10 D. For Figure S10 C, each dot reported on the uptake differential plots corresponds to the average value of three independent replicates. The repeatability of the measurement determined for each state (pooled standard deviation) using the 46 selected peptides and the 966 unique MS data points per state is reported in table S7. Sample size (n) for each statistical analysis: Triplicate labeling experiments were performed for each time point (7 time points including unlabeled controls) and condition for all HDX-MS analyses (independent technical replicates). Considering 46 peptides, 1 charge state, 3 replicates, 7 time points and 2 conditions, the complete HDX-MS datasets contains n = 1932 unique data points. Statistical methods used to assess significant differences with sufficient details: To take into account the time dependency of the exchange reaction, two distinct p-values were calculated per peptide using two individual Wald tests. The FDR was set to 5% ($p < 0.05$). Software used for statistical analysis: MEMHDX software (http://memhdx.c3bi.pasteur.fr).

Table S1: Sedimentation coefficient of P454, CaM and P454:CaM complex at a 1:1 molar ratio. P454 and CaM were investigated alone (at 57 µM and 72 µM, respectively) and mixed in a 1:1 molar ratio (at 70 µM each). Experiments were performed at 20°C in buffer B with density at 1.0310 $g.mL^{-1}$ and viscosity at 1.0061 cP.

	P454	CaM	P454:CaM
Sedimentation coefficient (S)	0.65 ± 0.1	1.85 ± 0.1	2.25 ± 0.1

Table S2: Thermodynamic parameters of P454:CaM titrations at different temperatures extracted from ITC experiments shown in Figure S3C-D.

Temperature (K)	K_A (10^6 M^{-1})	K_d (nM)	ΔH (kcal/mol)	ΔS (kcal/mol/K)	-TΔS (kcal/mol)	ΔG (kcal/mol)
283	28	35	2.6	0.043	-12.3	-9.6
293	3.6	270	-3.9	0.016	-4.8	-8.8
298	11	90	-5.3	0.014	-4.3	-9.6
303	8	120	-9.8	-0.0009	0.3	-9.5
311	6	160	-13.5	-0.012	3.8	-9.6

ΔG, ΔH and TΔS : S.D. < 1 kcal/mol. S.D. for ΔS is below 10%.

S.D for K_A and K_d is below 15%

Table S3: Affinity constants and free energy values of the P454-derived peptides for POPC:POPG SUVs and CaM. The free energy ΔG_{Kx} for POPC:POPG was calculated from the partition coefficient K_x. The K_d for CaM was calculated from fluorescent titrations and ITC experiments. Note that the K_d values for CaM and for membranes are expressed in nM and µM, respectively.

Peptides	K_d for CaM (nM)	ΔG_{Kd} for CaM (kcal/mol)	Partition coefficient K_X ($\times 10^3$)	ΔG_{Kx} * for POPC POPG 8:2 (kcal/mol)	K_d ** for POPC:POPG 8:2 (µM)	µH ***
P454	90	-9.6	790	-8	70	0.422
P454 R1Q	100	-9.5	190	-7.2	290	0.422
P454 R2Q	180	-9.2	150	-7	370	0.366
P454 R12Q	2090	-7.7	70	-6.6	790	0.366
P454 R12A	130	-9.4	280	-7.4	200	0.329
P454 R12K	50	-9.9	220	-7.3	260	0.421
P454 R12E	22700	-6.3	80	-6.7	690	0.396
P454 L463A	200	-9.1	630	-7.9	90	0.422
P454 L475A	120	-9.4	350	-7.7	160	0.363
P454 L481A	90	-9.6	780	-8	70	0.433
P454 I479A	1430	-7.9	330	-7.5	170	0.303
P454 I479V	110	-9.4	560	-7.8	100	0.375
P454 I479L	60	-9.8	700	-7.9	80	0.414
P454 H477S	190	-9.1	340	-7.5	160	0.435
P458	240	-9.0	190	-7.2	290	0.314
P454 H477S-I479A (HSIA)	1190	-8.0	105	-6.8	530	0.314
P454 W458A-I479A (WAIA)	2040	-7.7	4.2	-4.9	13200	0.303
P454 L463A-L475A-H477S-I479A (EtoR)	9090	-6.8	35	-6.2	1580	0.337
P454 W458A-L463A (HNter)	640	-8.4	22	-5.9	2550	0.422
P454 L475A-H477S-I479A (HCter)	1540	-7.9	18	-5.8	3160	0.314

* : the free energy of solution-to-membrane partiting is calculated from: $\Delta G_{Kx} = -RTLnKx$
**: The mole-fraction partition coefficient K_X is converted into the dissociation constant K_d using the following relation: $[W]/K_X = K_d$, where [W] is the water concentration (55.5 M).
***: Hydrophobic moment values are computed from Heliquest (with a window of 12) available at https://heliquest.ipmc.cnrs.fr/
S.D. values are within ± 10%.

Table S4: Thermodynamic parameters of the H:CaM ITC experiment performed at 25°C in buffer B shown in figure S7. A two-sites binding model was used to extract the thermodynamic parameters from the ITC data.

	Stoichiometry (n)	K_A (10^6 M^{-1})	K_d (nM)	ΔH (kcal/mol)	ΔS (kcal/mol/K)	-TΔS (kcal/mol)	ΔG (kcal/mol)
Site 1	0.9 ± 0.1	114 ± 12	9 ± 2	-5.4 ± 0.6	0.02 ± 0.002	-5.6 ± 0.6	-10.9 ± 1
Site 2	1.03 ± 0.1	2.6 ± 0.3	380 ± 50	-17.7 ± 2	-0.03 ± 0.003	8.9 ± 0.9	-8.7 ± 0.9

Table S5A. Diffraction data collection and refinement statistics of P458:CaM crystal structures.

	C2221_form	P212121_form
Crystallization conditions	0.3 M Ammonium sulfate 30% (w/v) PEG 4000	0.2M of MgCl2 0.1M HEPES-HCl pH 7.5 25% (w/v) PEG3350
Resolution range	67.6-3.11 (3.23 -3.11)	88.86 -3.93 (4.07 - 3.93)
Space group	C 2 2 21	P 21 21 21
Unit cell	73.341 174.344 97.843 90 90 90	97.001 106.974 221.635 90 90 90
Total reflections	103617 (10499)	140108 (14505)
Unique reflections	11538 (1132)	21073 (2063)
Multiplicity	9.0 (9.3)	6.6 (7.0)
Completeness (%)	99.49 (99.65)	99.54 (99.76)
Mean I/sigma(I)	22.97 (3.18)	8.15 (3.03)
Wilson B-factor	97.46	110.61
R-merge	0.055 (0.647)	0.188 (0.736)
R-meas	0.058 (0.684)	0.204 (0.794)
R-pim	0.018 (0.219)	0.078 (0.297)
CC1/2	1 (0.946)	0.997 (0.875)
CC*	1 (0.986)	0.999 (0.966)
Reflections used in refinement	11538 (1129)	21073 (2061)
Reflections used for R-free	592 (52)	1074 (96)
R-work	0.246 (0.385)	0.221 (0.252)
R-free	0.290 (0.488)	0.284 (0.314)
CC(work)	0.893 (0.913)	0.960 (0.895)
CC(free)	0.860 (0.777)	0.945 (0.860)
Number of non-hydrogen atoms	2665	17084
macromolecules	2656	17055
ligands	9	29
Protein residues	340	2209
RMS(bonds)	0.010	0.016
RMS(angles)	1.16	1.74
Ramachandran favored (%)	98.19	97.07
Ramachandran allowed (%)	1.51	2.51
Ramachandran outliers (%)	0.30	0.43
Rotamer outliers (%)	0.00	0.00
Clashscore	8.85	19.35
Average B-factor	147.89	113.81
macromolecules	147.92	113.86
ligands	138.83	84.03
Number of TLS groups	10	
Molecules per ASU (CaM/P458)	2/2	12/24
PDB entry	6YNU	6YNS

Statistics for the highest-resolution shell are shown in parentheses.

Inaccessible residues
Solvent-accessible residues
HSDC Residues making **H**ydrogen/**D**isulphide bond, **S**alt bridge or **C**ovalent link
Interfacing residues
ASA Accessible Surface Area, Å² **BSA** Buried Surface Area, Å² **ΔⁱG** Solvation energy effect, kcal/mol |||| Buried area percentage, one bar per 10%

##	Structure 1	HSDC	ASA	BSA	ΔⁱG
1	D:TRP 458		271.16	0.00	0.00
2	D:GLY 459		42.33	0.00	0.00
3	D:GLN 460		158.25	0.00	0.00
4	D:ARG 461		225.16	0.00	0.00
5	D:ALA 462		55.33	0.00	0.00
6	D:LEU 463		81.81	0.00	0.00
7	D:GLN 464		125.76	30.14 |||	-0.22
8	D:GLY 465		36.08	0.00	0.00
9	D:ALA 466		58.78	0.00	0.00
10	D:GLN 467		121.94	0.00	0.00
11	D:ALA 468		58.38	40.38 ||||||	0.56
12	D:VAL 469		97.90	14.59 ||	0.21
13	D:ALA 470		57.59	0.00	0.00
14	D:ALA 471		53.67	27.62 ||||||	0.44
15	D:ALA 472		52.18	52.02 ||||||||||	0.81
16	D:GLN 473		92.30	15.70 ||	-0.11
17	D:ARG 474		190.61	0.00	0.00
18	D:LEU 475		118.41	94.55 ||||||||	1.51
19	D:VAL 476		82.31	77.99 ||||||||	1.11
20	D:HIS 477		95.24	31.60 ||||	0.62
21	D:ALA 478		55.07	29.39 ||||||	0.09
22	D:ILE 479		146.52	141.87 ||||||||||	1.82
23	D:ALA 480		93.41	75.23 |||||||||	0.65
24	D:LEU 481		177.28	27.72 ||	0.04

Table S5B. P454 residues involved in the interaction with the N-lobe of CaM.

##	Structure 1	HSDC	ASA	BSA	ΔⁱG
1	B:TRP 458	H	280.59	241.34 |||||||||	2.17
2	B:GLY 459		41.61	0.00	0.00
3	B:GLN 460		142.80	16.89 ||	-0.19
4	B:ARG 461		245.37	5.53		-0.05
5	B:ALA 462		64.72	54.60 |||||||||	0.63
6	B:LEU 463		65.71	53.88 |||||||||	0.80
7	B:GLN 464		111.46	0.00	0.00
8	B:GLY 465		33.89	12.00 ||||	0.18
9	B:ALA 466		62.78	62.78 ||||||||||	0.86
10	B:GLN 467		115.46	75.30 |||||||	-0.09
11	B:ALA 468		62.88	0.00	0.00
12	B:VAL 469		97.01	42.40 |||||	0.68
13	B:ALA 470		57.70	47.98 |||||||||	0.76
14	B:ALA 471		54.54	0.17		0.00
15	B:ALA 472		50.81	0.00	0.00
16	B:GLN 473		91.56	0.00	0.00
17	B:ARG 474	HS	192.35	49.69 |||	-0.54
18	B:LEU 475		117.88	0.00	0.00
19	B:VAL 476		84.08	0.00	0.00
20	B:HIS 477		99.60	0.00	0.00
21	B:ALA 478		67.87	0.00	0.00
22	B:ILE 479		146.78	0.00	0.00
23	B:ALA 480		80.63	0.00	0.00
24	B:LEU 481		181.92	0.00	0.00

Table S5C. P454 residues involved in the interaction with the C-lobe of CaM.

Table S6: Data collection and scattering derived parameters from SAXS.

	CaM	P454-CaM	*H-CaM*[a]	*MLCK-CaM*[a]
Data collection parameters				
Instrument	SWING (SOLEIL)			
Detector	CCD-based AVIEX			
Beam geometry	0.8 mm x 0.15 mm			
Wavelength [Å]	1.0			
q-range [$Å^{-1}$]	$0.006 < q < 0.50$			
Absolute scaling	Comparison with scattering from pure H_2O			
Exposure (Dead) time [s]	1/0.5			
Temperature [K]	288			
SEC-SAXS column	Biosec 3 Agilent			
Loading concentration[µM]	409	136 (CaM)-272(P454)		
Injection volume [µL]	50			
Buffer	20 mM Hepes, 150 mM NaCl, 4 mM CaCl2, pH 7.4			
Flow rate [$mL.min^{-1}$]	0.2			
Software employed for SAXS data reduction and analysis				
Foxtrot	SWING in-house software			
PRIMUS	ATSAS 2.8 suite, Franke et al. J. Appl. Cryst. 2017			
DADIMODO	Roudenko O., Thureau A. & Pérez J., 2018			
DAMMIF/DAMMIN	D. Franke and D. I. Svergun, J. Appl. Cryst. 2009			
Structural parameters				
I(0) Guinier [cm^{-1}]	0.02576 ± 0.00004	0.00781 ± 0.00001	*0.0159*	*0.0134*
R_g Guinier [Å]	22.16 ± 0.1	19.74 ± 0.1	*21.9*	*17.4*
qRg-range	0.250 - 1.03	0.256 - 1.30		
I(0) p(r) [cm^{-1}]	0.02574 ± 0.00004	0.00783 ± 0.00001	*0.0159*	*0.0134*
R_g p(r) [Å]	22.25 ± 0.1	19.96 ± 0.1	*22.1*	*17.3*
q-range [$Å^{-1}$]	0.0113 - 0.35	0.013 - 0.35		
D_{Max} [Å]	73	70	*75*	*52*
Molecular mass determination				
$MM_{sequence}$ [kDa] [b]	16.8	20.1		
$MM_{SAXS\ MoW}$ [kDa] [c]	17.2	19.9		
$MM_{SAXS\ QR}$ [kDa] [d]	16.4	19.1		
DAMMIF/DAMMIN analysis				
Model number	20	20		
NSD	0.56	0.74		
χ^2 (Dammin)	1.56	1.34		
DADIMODO analysis				
Model number		20		
q-range [$Å^{-1}$]		0.016-0.50		
χ^2 (Crysol)		1.49-1.70		

[a] Values extracted from Table S1 in O'Brien *et al.*, *PLoS Biol* **2017,** *15* (12), e2004486 [4].

[b] The calculated masses were derived from the sequences.

[c] Molecular mass M obtained from the whole I(q) curve (q_{max} = 0.3$Å^{-1}$) using the SAXS-MoW2 program, available at http://saxs.ifsc.usp.br/.

[d] Molecular mass M obtained from the whole I(q) curve (q_{max} = 0.25 $Å^{-1}$) using the ScÅtter3 program, available at https://bl1231.als.lbl.gov/scatter/.

Table S7: HDX Data Summary

EXPERIMENT	**P454 BINDING TO CaM**	
Dat set :	CaM_Ca	CaM_Ca_P454
HDX reaction details ○ *pD* ○ *T°C* ○ *Excess deuterium*	 7.4 20°C 80%	 7.4 20°C 80%
HDX time course analyzed (min)	0.16, 1, 10, 30, 60, 120	0.16, 1, 10, 30, 60, 120
Number of peptides	46	46
Sequence coverage	89.3	89.3
Average peptide length	11.7	11.7
Redundancy	4.01	4.01
Average peptide length/Redundancy ratio	2.91	2.91
Replicates	3 (technical)	3 (technical)
Repeatability (pooled standard deviation)[#]	0.07 Da	0.07 Da
Significant difference between state[$]	Wald test, $p < 0.05$	

[#] One unique charge state was used per peptide
[$] MEMHDX (www. memhdx.c3bi.pasteur.fr)

Table S8: Estimation of the α-helical content of P454-derived peptides. The secondary structure content is estimated using the on-line Bestsel software [17] available at http://bestsel.elte.hu/index.php. The alpha-helical content (%) is reported in the table for each peptide in buffer A, in 20% TFE and in the presence of POPC POPG (molar ratio 8:2) at 2 mM lipid concentration. The far-UV CD spectra of several P454-derived peptides are shown in figure S12.

P454 derived peptide	Solution (helix, %)	TFE 20% (helix, %)	POPC:POPG 8:2 (helix, %)
P454	17 ± 2	60 ± 2	50 ± 1
P454 R12Q	8 ± 4	50 ± 2	23 ± 1
P454 R12K	13 ±2	45 ± 4	26 ± 1
P454 R12E	6 ± 1	55 ± 3	10 ± 1
P454 L463A	14 ± 2	48 ± 3	19 ± 2
P454 L475A	5 ± 2	45 ± 1	15 ± 1
P454 L481A	5 ± 1	49 ± 1	44 ± 3
P454 I479A	8 ± 2	29 ± 1	12 ± 3
P454 I479V	2 ± 1	47 ± 6	37 ± 2
P454 I479L	13 ± 1	51 ± 1	51 ± 5
P454 H477S	4 ± 2	40 ± 1	20 ± 2
P458	10 ± 4	50	23 ± 2
P454 W458A-I479A	10 ± 3	55 ± 1	7 ± 3
P454 L463A-L475A-H477S-I479A (EtoR)	4 ± 1	38 ± 2	5 ± 2
P454 W458A- L463A (HNt)	7 ± 1	56	8 ± 2
P454 H477S-I479A	2 ± 2	51 ± 4	27 ± 3
P454 L475A-H477S-I479A (HCt)	6 ± 2	51 ± 4	6 ± 2

Table S9: Concentrations of P454-derived peptides required to induce the recovery of 50% of ANTS fluorescence intensity upon LUVs permeabilization ($C_{P1/2}$) (see Material and Methods for details). Vesicle permeabilization induced by P454-derived peptides is blocked by the addition of calmodulin in the presence of calcium (see Material and Methods for details), except for the peptides (i.e., R12E, EtoR and W458A-I479A) that cannot be assayed as they do not permeabilize vesicles. Substituted residues are bold in the peptide sequences. S.D.: ± 5%, excepted for R12E, W458A-I479A and EtoR for which the $Cp_{1/2}$ values cannot be determined.

Peptide name (nickname)	$C_{P1/2}$ (μM)	Peptide sequences
P454 WT	0.07	ASAHWGQRALQGAQAVAAAQRLVHAIALMTQ
P454 R461Q (R*1*Q)	0.22	ASAHWGQ**Q**ALQGAQAVAAAQRLVHAIALMTQ
P454 R474Q (R*2*Q)	0.11	ASAHWGQRALQGAQAVAAAQ**Q**LVHAIALMTQ
P454 R461Q R474Q (R*12*Q)	0.23	ASAHWGQ**Q**ALQGAQAVAAAQ**Q**LVHAIALMTQ
P454 R461A R474A (R*12*A)	0.14	ASAHWGQ**A**ALQGAQAVAAAQ**A**LVHAIALMTQ
P454 R461K R474K (R*12*K)	0.09	ASAHWGQ**K**ALQGAQAVAAAQ**K**LVHAIALMTQ
P454 R461E R474E (R*12*E)	> 50	ASAHWGQ**E**ALQGAQAVAAAQ**E**LVHAIALMTQ
P454 L463A (L463A)	0.41	ASAHWGQRA**A**QGAQAVAAAQRLVHAIALMTQ
P454 L475A (L475A)	0.64	ASAHWGQRALQGAQAVAAAQR**A**VHAIALMTQ
P454 L481A (L481A)	0.06	ASAHWGQRALQGAQAVAAAQRLVHAIA**A**MTQ
P454 I479A (I479A)	7.86	ASAHWGQRALQGAQAVAAAQRLVHA**A**ALMTQ
P454 I479V (I479V)	0.09	ASAHWGQRALQGAQAVAAAQRLVHA**V**ALMTQ
P454 I479L (I479L)	0.04	ASAHWGQRALQGAQAVAAAQRLVHA**L**ALMTQ
P454 H477S (H477S)	0.25	ASAHWGQRALQGAQAVAAAQRLV**S**AIALMTQ
P458	1.26	WGQRALQGAQAVAAAQRLVHAIAL
P454 H477S-I479A	1.88	ASAHWGQRALQGAQAVAAAQRLV**S**A**A**ALMTQ
P454 W458A-I479A	> 80	ASAH**A**GQRALQGAQAVAAAQRLVHA**A**ALMTQ
P454 L463A-L475A-H477S-I479A	> 50	ASAHWGQRA**A**QGAQAVAAAQR**A**V**S**A**A**ALMTQ
P454 W458A-L463A	6.59	ASAH**A**GQRA**A**QGAQAVAAAQRLVHAIALMTQ
P454 L475A-H477S-I479A	9.03	ASAHWGQRALQGAQAVAAAQR**A**V**S**A**A**ALMTQ

A

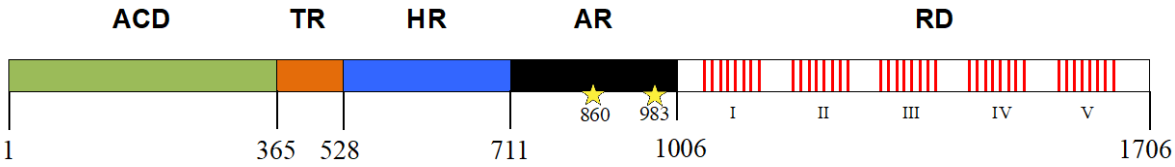

B

MQQSHQAGYANAADRESGIPAAVLDGIKAVAKEKNATLMFRLVNPHSTSLIAEGVATKGLGVHAKSSD
WGLQAGYIPVNPNLSKLFGRAPEVIARADNDVNSSLAHGHTAVDLTLSKERLDYLRQAGLVTGMADGV
VASNHAGYEQFEFRVKETSDGRYAVQYRRKGGDDFEAVKVIGNAAGIPLTADIDMFAIMPHLSNFRDS
ARSSVTSGDSVTDYLARTRRAASEATGGLDRERIDLLWKIARAGARSAVGTEARRQFRYDGDMNIGVI
TDFELEVRNALNRRAHAVGAQDVVQHGTEQNNPFPEADEKIFVVSATGESQMLTRGQLKEYIGQQRGE
GYVFYENRAYGVAGKSLFDDGLGAAPGVPSGRSKFSPDVLETVPASPGLRRPSLGAVERQDSGYDSLD
GVGSRSFSLGEVSDMAAVEAAELEMTRQVLHAGARQDDAEPGVSG**ASAHWGQRALQGAQAVAAAQRLV
HAIALMTQ**FGRAGSTNTPQEAASLSAAVFGLGEASSAVAETVSGFFRGSSRWAGGFGVAGGAMALGGG
IAAAVGAGMSLTDDAPAGQKAAAGAEIALQLTGGTVELASSIALALAAARGVTSGLQVAGASAGAAAG
ALAAALSPMEIYGLVQQSHYADQLDKLAQESSAYGYEGDALLAQLYRDKTAAEGAVAGVSAVLSTVGA
AVSIAAAASVVGAPVAVVTSLLTGALNGILRGVQQPIIEKLANDYARKIDELGGPQAYFEKNLQARHE
QLANSDGLRKMLADLQAGWNASSVIGVQTTEISKSALELAAITGNADNLKSVDVFVDRFVQGERVAGQ
PVVLDVAAGGIDIASRKGERPALTFITPLAAPGEEQRRRTKTGKSEFTTFVEIVGKQDRWRIRDGAAD
TTIDLAKVVSQLVDANGVLKHSIKLDVIGGDGDDVVLANASRIHYDGGAGTNTVSYAALGRQDSITVS
ADGERFNVRKQLNNANVYREGVATQTTAYGKRTENVQYRHVELARVGQLVEVDTLEHVQHIIGGAGND
SITGNAHDNFLAGGSGDDRLDGGAGNDTLVGGEGQNTVIGGAGDDVFLQDLGVWSNQLDGGAGVDTVK
YNVHQPSEERLERMGDTGIHADLQKGTVEKWPALNLFSVDHVKNIENLHGSRLNDRIAGDDQDNELWG
HDGNDTIRGRGGDDILRGGLGLDTLYGEDGNDIFLQDDETVSDDIDGGAGLDTVDYSAMIHPGRIVAP
HEYGFGIEADLSREWVRKASALGVDYYDNVRNVENVIGTSMKDVLIGDAQANTLMGQGGDDTVRGGDG
DDLLFGGDGNDMLYGDAGNDTLYGGLGDDTLEGGAGNDWFGQTQAREHDVLRGGDGVDTVDYSQTGAH
AGIAAGRIGLGILADLGAGRVDKLGEAGSSAYDTVSGIENVVGTELADRITGDAQANVLRGAGGADVL
AGGEGDDVLLGGDGDDQLSGDAGRDRLYGEAGDDWFFQDAANAGNLLDGGDGRDTVDFSGPGRGLDAG
AKGVFLSLGKGFASLMDEPETSNVLRNIENAVGSARDDVLIGDAGANVLNGLAGNDVLSGGAGDDVLL
GDEGSDLLSGDAGNDDLFGGQGDDTYLFGVGYGHDTIYESGGGHDTIRINAGADQLWFARQGNDLEIR
ILGTDDALTVHDWYRDADHRVEIIHAANQAVDQAGIEKLVEAMAQYPDPGAAAAAPPAARVPDTLMQS
LAVNWR

Figure S1: (**A**) Schematic representation of the CyaA toxin. The toxin is composed of the following domains: a N-terminal catalytic domain (ACD, residues 1-364), a translocation region (TR, 365-527), a hydrophobic region (HR, 528-710), an acylation region (AR, 711-1005) with acylated K860 and K983 labeled with yellow stars, and a C-terminal receptor-binding domain (RD, 1006-1706) containing the Repeat-in-ToXin (RTX) motifs (red bars). (**B**) Sequence of the full-length CyaA toxin from *Bordetella pertussis*. The region corresponding to the P454 peptide is bold and underlined. The same color code is used in panels A and B.

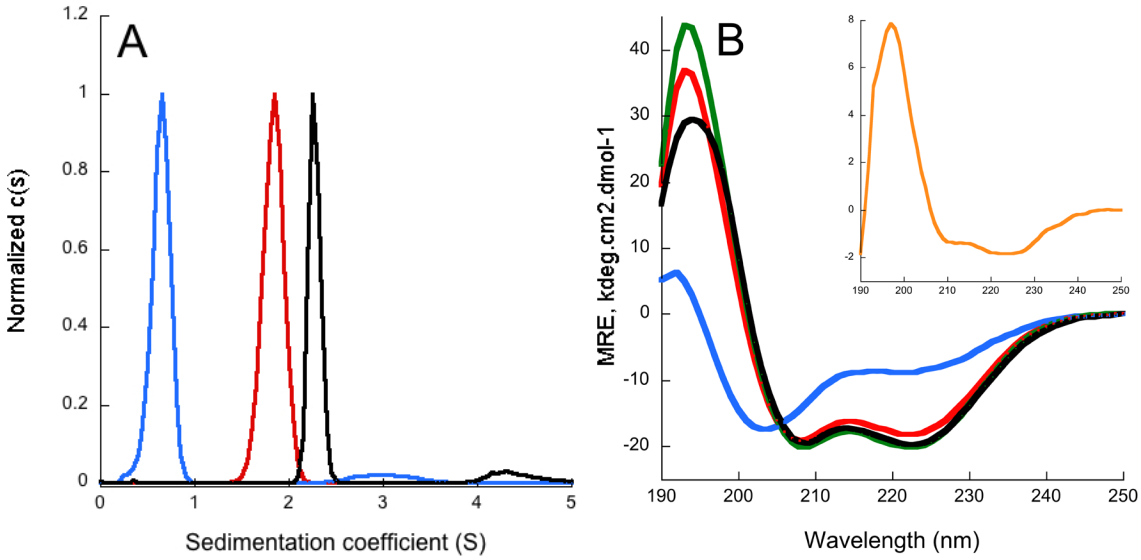

Figure S2: (**A**) Sedimentation coefficient distributions of P454 (blue), CaM (red) and the P454:CaM complex (black). Sedimentation coefficients are listed in Table S1. (**B**) Synchrotron radiation circular dichroism in the far-UV region of P454 and CaM. Spectra were recorded in a 100 µm cell. Far-UV spectra of P454 (blue), CaM (green) or P454:CaM at a 1:1 molar ratio (black) in buffer B. The red spectrum corresponds to the combination of the isolated CaM and P454 spectra. The inset corresponds to the structural changes induced by the P454:CaM complex formation (subtraction of the black spectrum by the red spectrum). The subtraction spectrum shows that the P454:CaM complex formation induces an increase of secondary structure content. Experimental conditions: buffer B, temperature: 25°C.

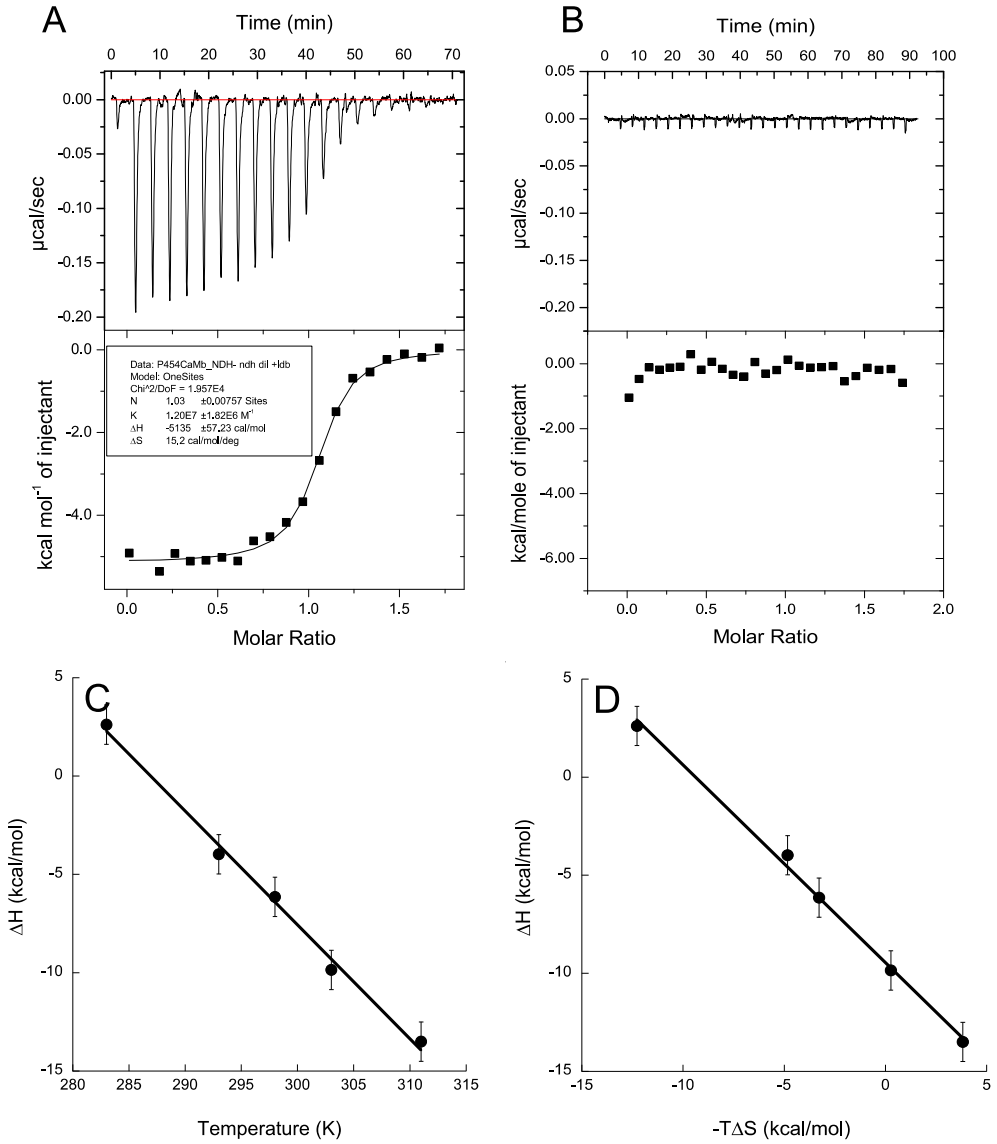

Figure S3: (**A**) Isothermal titration calorimetry of CaM by P454 in buffer B at 25°C using a VP-ITC instrument. Titration was performed by injections of 13 µL of P454 (loaded in the syringe at 90 µM) into the cell containing CaM at 10 µM (see Table S3 for ΔG values). (**B**) Isothermal titration calorimetry of CaM by P454 in buffer A complemented with 0.2 mM EDTA at 25°C. Titration was performed by consecutive injections of 10 µL of P454 (loaded in the syringe at 90 µM) into the cell containing CaM at 10 µM. (**C**) ITC experiments were performed at various temperatures to infer the heat capacity of the reaction. The slope of ΔH=f(T) provides us with the heat capacity ΔCp of the P454:CaM complex. The ΔCp value is negative, as measured for canonical CaM-binding peptides [36], however, lower than those measured for globular peptide:CaM complexes, suggesting that the P454:CaM complex does not adopt a globular conformation. This is confirmed by X-ray and SAXS data reported in this article. (**D**) Representation of the enthalpy-entropy compensation (EEC) plot derived from ITC experiments of P454:CaM titrations at different temperatures. The P454:CaM complex formation at various temperatures follows a typical entropy-enthalpy compensation. The enthalpy and temperature values are listed in Table S2. S.D for ΔH values is ± 1 kcal/mol.

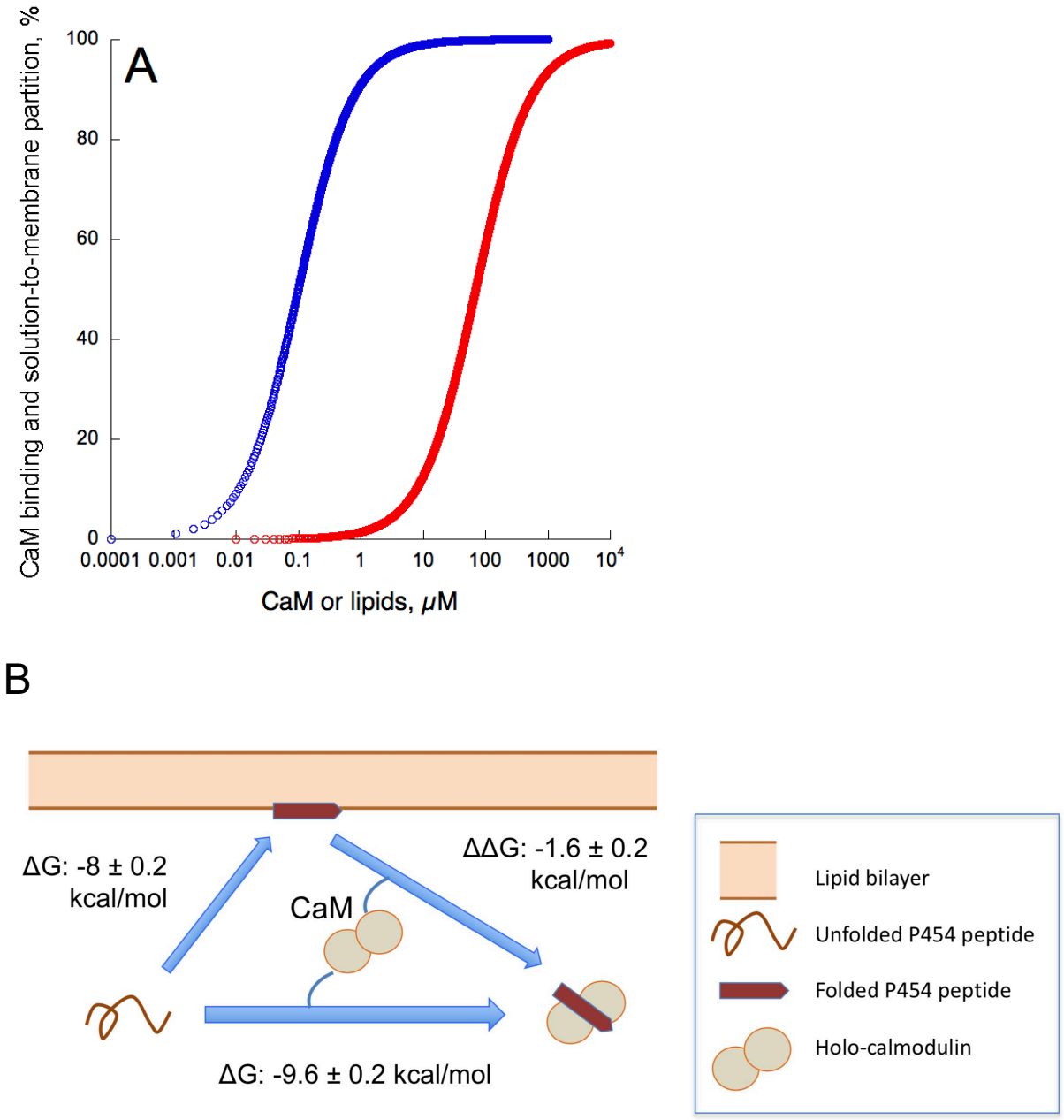

Figure S4: (**A**) Fraction of P454 bound to CaM and membrane, calculated from the affinity constants for CaM (K_d=90 nM, blue trace) and POPC POPG 8:2 membranes (K_d=70 μM, red trace). The mole-fraction partition coefficient K_X is converted into K_d using the following relation: $[W]/K_X = K_d$, where [W] is the water concentration (55.5 M). (**B**) Scheme of P454 interactions with membranes and CaM. The P454 peptide is represented in red and CaM by two grey lobes. The free energy of interaction of P454 with membrane and with CaM was calculated from its K_X and K_d values, as described in the materials and methods section. The K_X and K_d values are listed in Table S3.

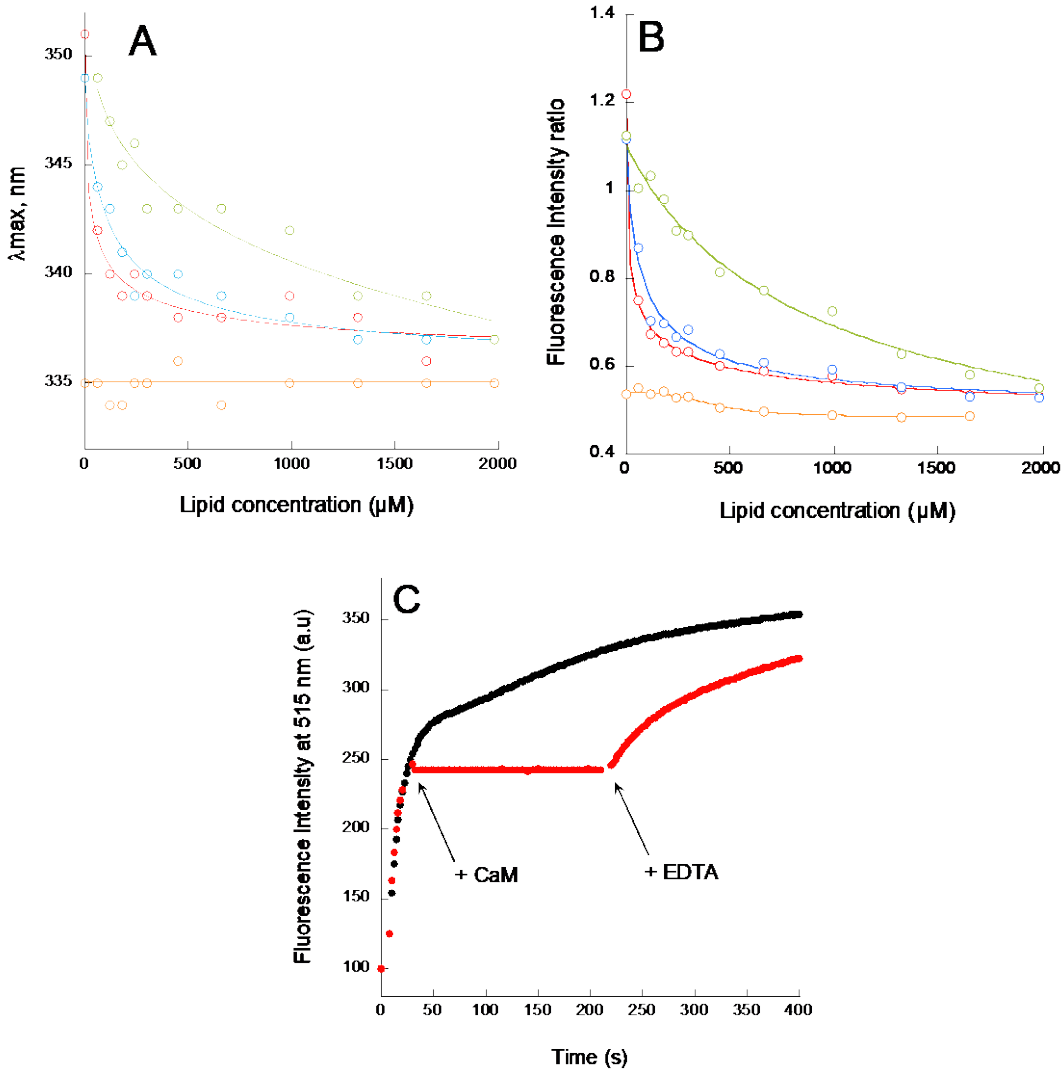

Figure S5: P454 membrane interaction and permeabilization followed by fluorescence. Maximum wavelength of emission (**A**) and ratio of fluorescence intensity (**B**) of P454 followed by tryptophan fluorescence as a function of lipid concentration. A sample of P454 is prepared for each lipid concentration. Tryptophan fluorescence of P454 was first measured for each concentration of lipids with SUVs composed of POPC POPG 8:2 (red circles) in buffer A. Then, an excess of apo-CaM is added to each sample (blue circles, molar ratio P454:CaM 1:3), followed by 1 mM of calcium (orange circles) and finally 2 mM EDTA (green circles). (**C**) Membrane permeabilization assay. Time course of ANTS and DPX efflux from LUVs made of POPC POPG 8:2 (0.45 mM lipid concentration) in buffer B, *i.e.*, including 2 mM $CaCl_2$. Experiment was performed in the presence of P454 at 100 nM (black curve). In red, the same experiment is performed but holo-CaM is added (molar ratio P454:CaM 1:3) at 40 sec, followed by addition of 5 mM EDTA (red curve).

Figure S6: Droplet Interfacial Bilayers (DIB) experiments.

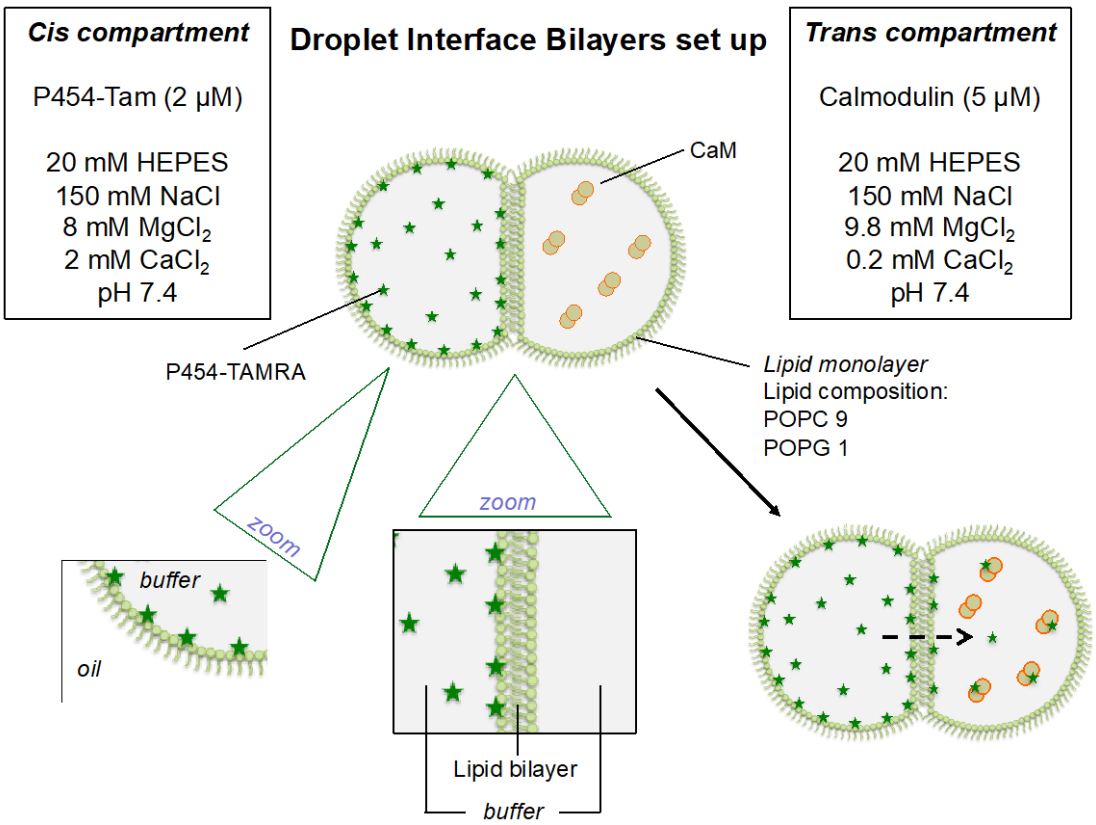

Figure S6A: Scheme of the Droplet Interface Bilayer (DIB) experimental set-up.

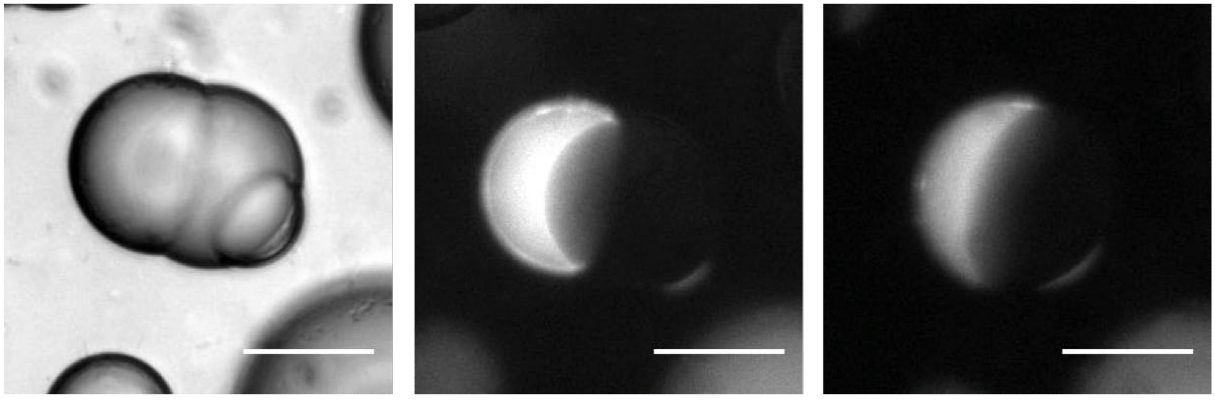

Figure S6B: Pictures of a DIB made of 10% POPG 90% POPC with P454 (2 µM) in the left droplet and without CaM in the right droplet. On the left: brightfield microscopy image. In the middle: fluorescence microscopy image at the beginning of the experiment (t=0min). On the right: fluorescence microscopy image after 15 minutes of experiment. No fluorescence was observed in the *trans* compartment in this experiment. Scale bar represents 30 µm.

Figure S6 continued on next page

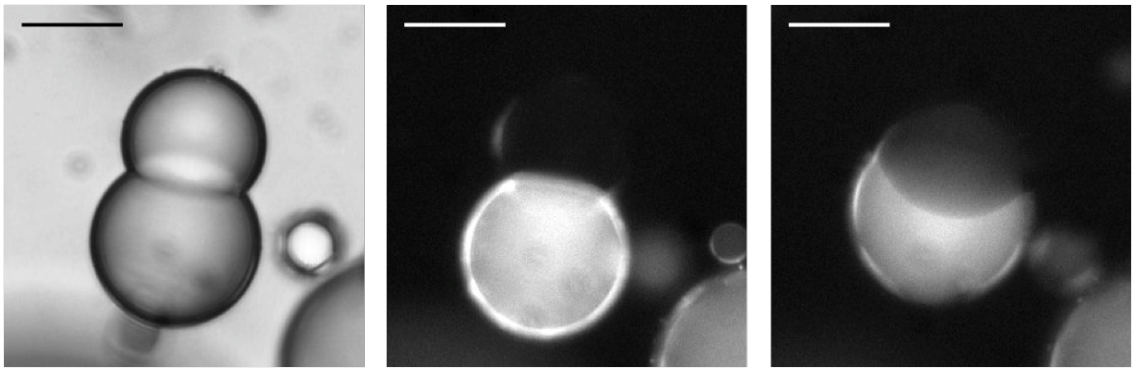

Figure S6C: Images of a DIB made of 10% POPG 90% POPC with P454 (2 µM) in the bottom droplet and CaM (5 µM) in the upper droplet. On the left: brightfield microscopy image. In the middle: fluorescence microscopy image at the beginning of the experiment (t=0min). On the right: fluorescence microscopy image after 15 minutes of experiment. Translocation was observed in this experiment. Scale bar represents 30 µm.

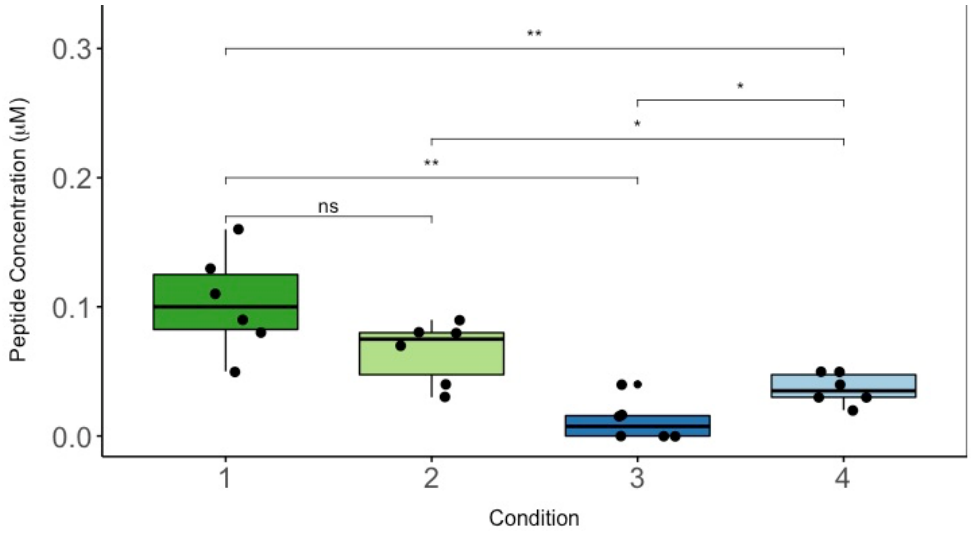

Figure S6D: Peptide translocation across droplet interface bilayers. Boxplot representation of the TAMRA-P454 concentration (µM) in the *trans* droplet 15 min after the formation of the droplet interface bilayers (see Material and Methods for details). All experiments were performed in the presence of a calcium gradient across the lipid bilayer ($CaCl_2$: 2 mM *cis vs* 0.2 mM *trans*). Peptide concentration in the *trans* droplet of TAMRA-P454 WT (green conditions, 1-2) and TAMRA-P454 R12E (blue conditions, 3-4) was measured in the presence of 5 µM of CaM (dark colors, 1 and 3) and 100 µM of CaM (light colors, 2 and 4) in the *trans* droplet. Five to seven independent trials were conducted for each condition. Mann-Whitney-Wilcoxon test was applied to compare experiments.

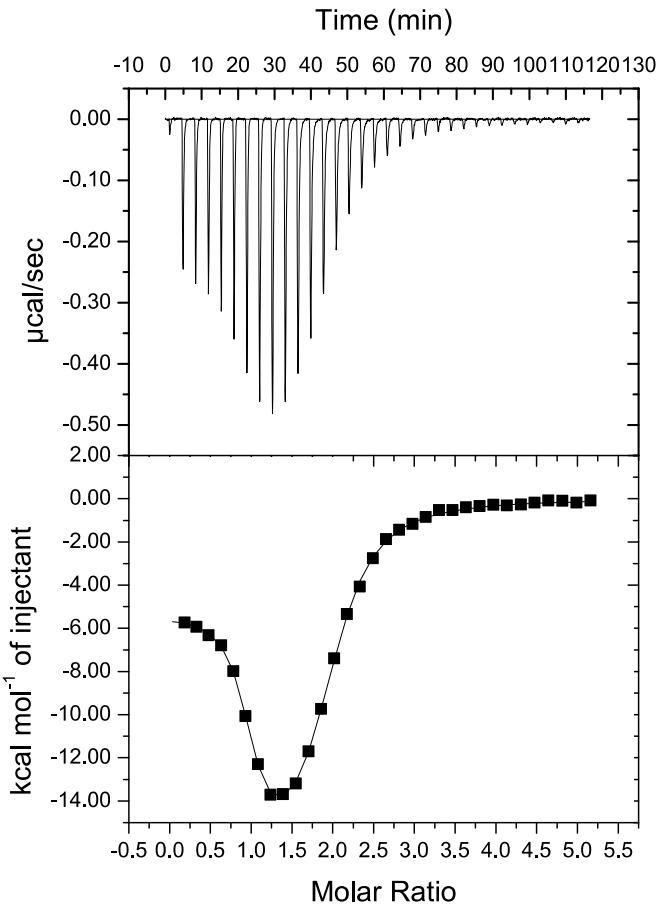

Figure S7: Isothermal titration calorimetry of holo-CaM by the H-helix peptide in buffer B at 25°C. The H-helix peptide is loaded in the syringe at 130 µM and CaM in the cell at 5 µM. Titration was performed on VP-ITC with consecutive injections of 8 µL. A two-sites binding model was used to fit to the ITC data and to extract the thermodynamic parameters reported in Table S4.

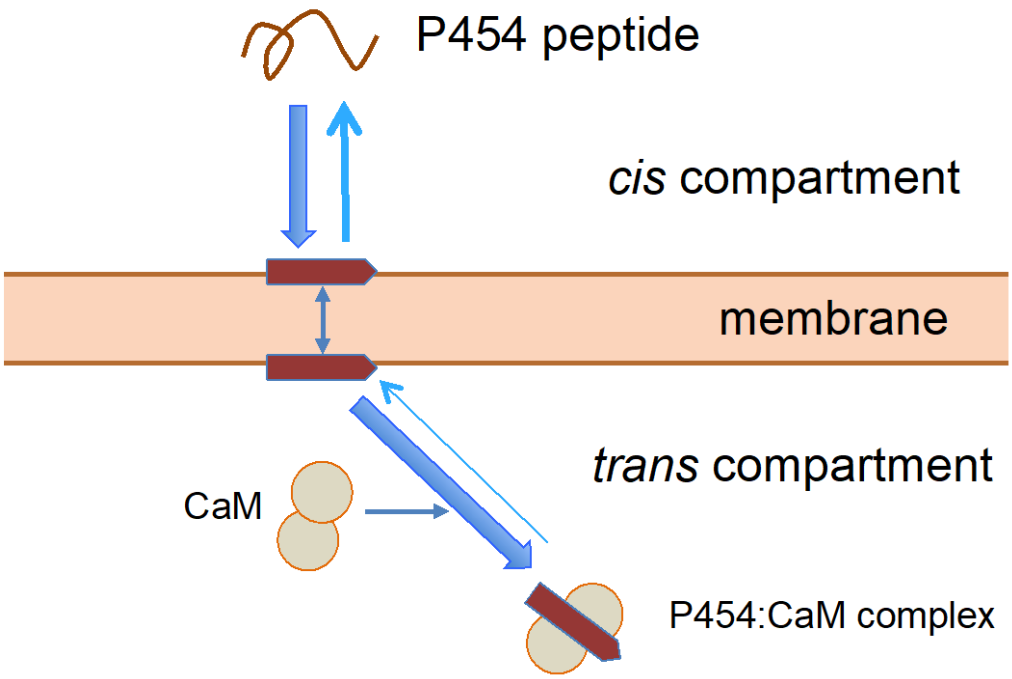

Figure S8: Scheme of the P454 translocation and CaM binding inferred from the *in vitro* experiments based on the ITC, fluorescence, SRCD and DIB experiments described in this study.

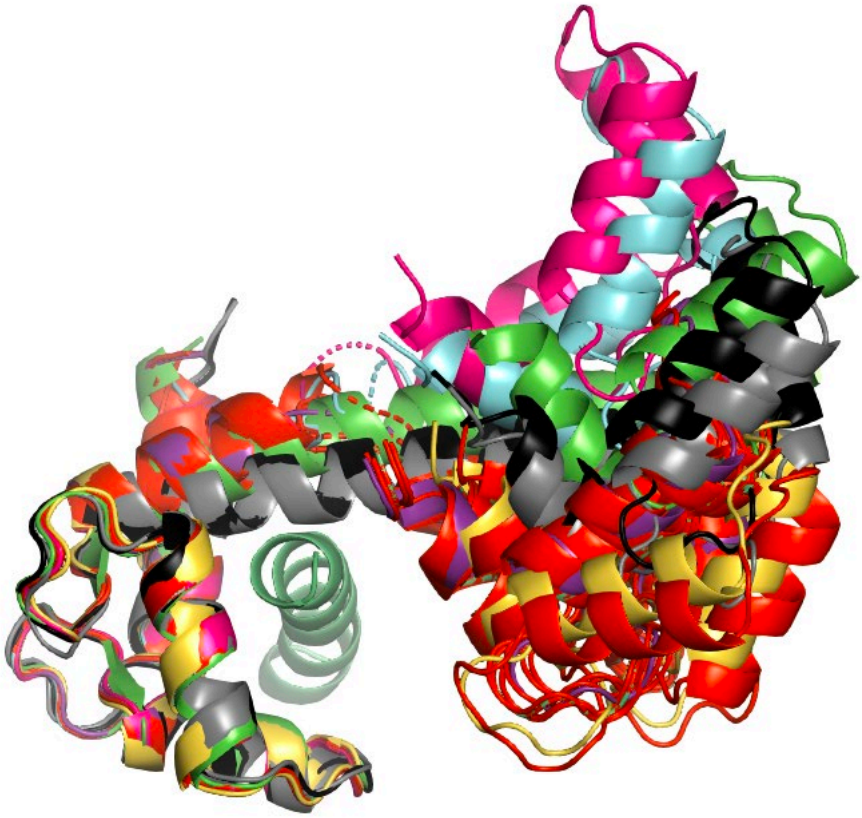

Figure S9: Superimposition of the fourteen P458:CaM crystal structures. The crystal structure 1CLL [37] of the extended conformation of CaM is shown in light green. The 2 crystal structures 6YNU (black and grey) and the 12 crystal structures 6YNS are displayed with the N-CaM lobe superimposed. The P458 peptide is shown in cartoon representation and colored in green. Diffraction data collection and refinement statistics of P458:CaM crystal structures 6YNS and 6YNU are given in Table S5.

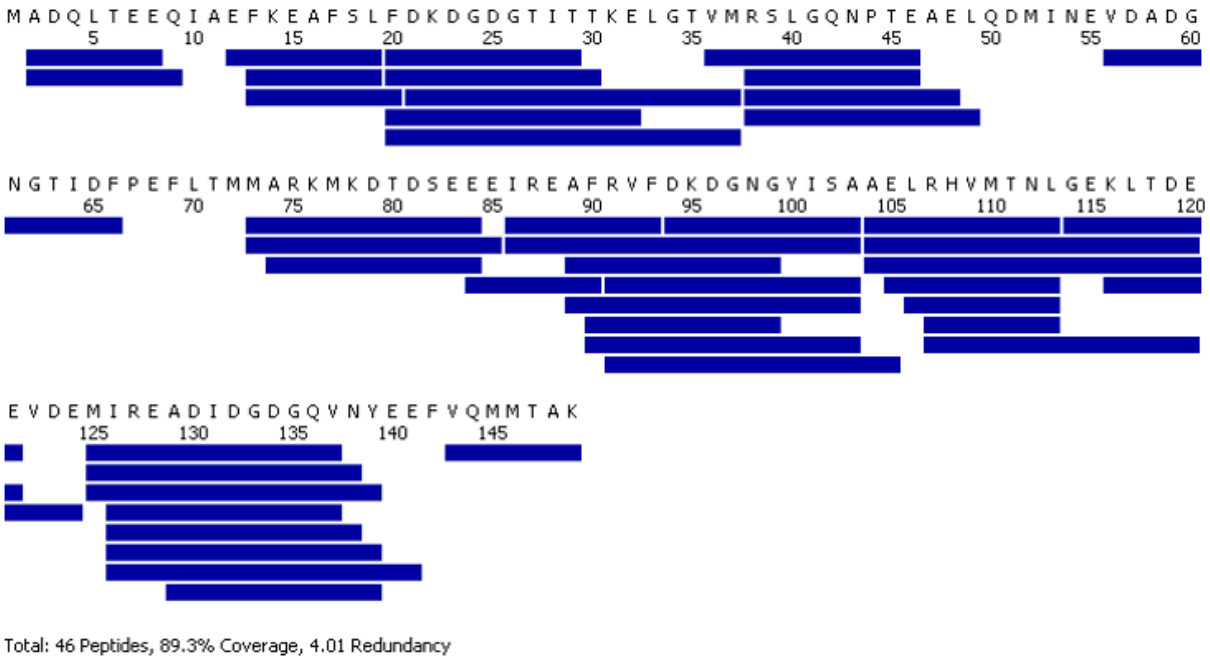

Figure S10A: Peptide map used to analyze the deuterium content in CaM. CaM was digested with immobilized pig pepsin at 20°C and pH 2.5 for 2 min. Each blue bar corresponds to a unique peptide selected for HDX-MS analysis. A final linear sequence coverage 89.3% (4.01 redundancy) was achieved.

Figure S10 continued next page

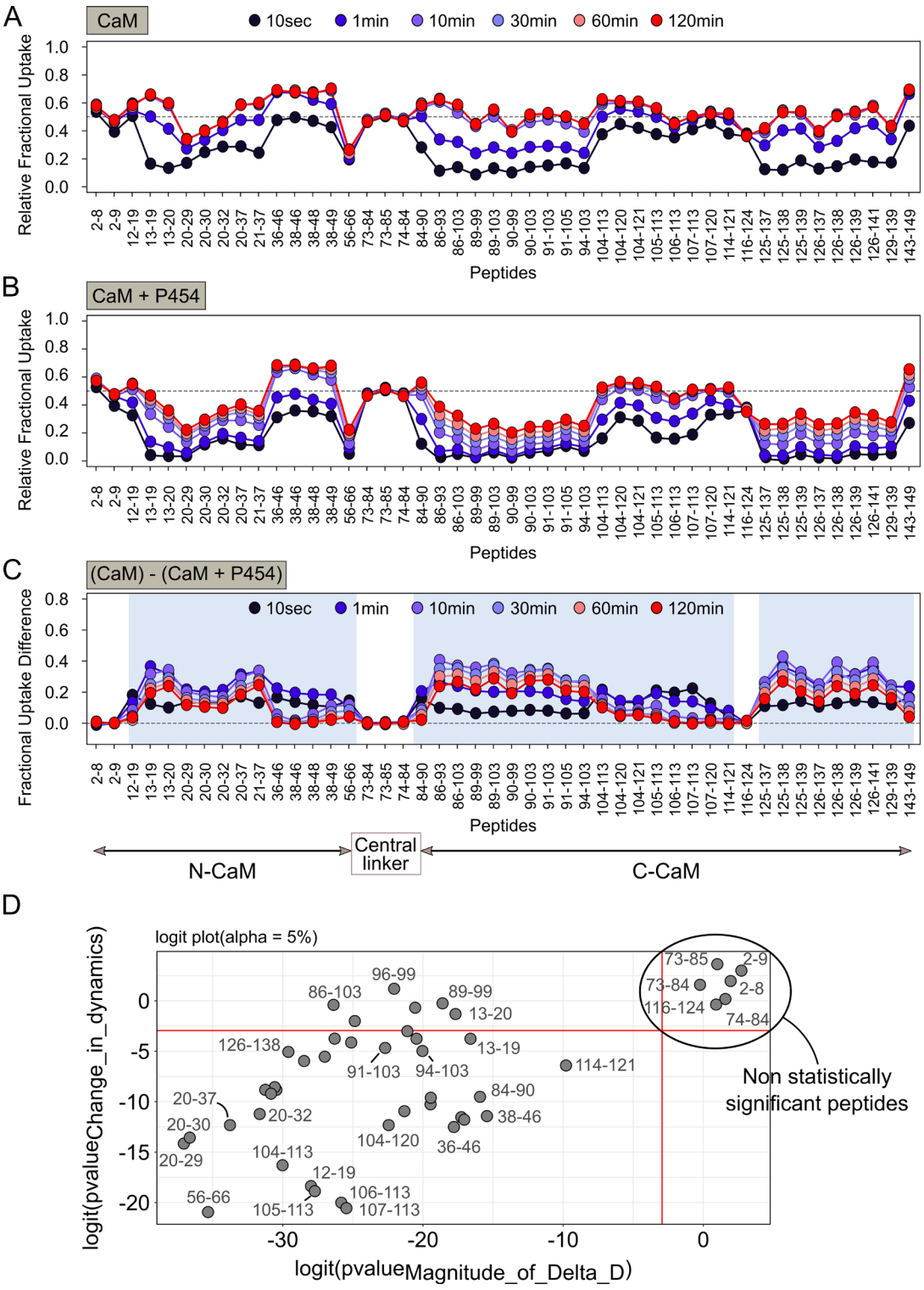

Figure S10 continued. Effect of P454 binding on the HDX-MS behavior of full-length human CaM. Fractional uptake profiles of CaM alone (**A**) and in the presence of a 4-fold molar excess P454 (**B**). The deuterium content calculated for each peptide and condition and at each time point is plotted as a function of peptide position. Each dot corresponds to the average value of three independent replicates. (**C**) Differential fractional uptake plot showing the uptake difference between full-length human CaM alone and in the presence of a 2-fold molar excess P454 for all peptides and labeling time points. The binding of P454 induces significant reduction of deuterium uptake throughout both N- and C-terminal of CaM.

Regions displaying statistically significant variations of deuterium uptake in the presence of P454 (Wald test, $p < 0.05$) are highlighted in light blue. (**D**) Logit representation showing the statistical results obtained with MEMHDX for each peptide (gray dots) of CaM in the presence of P454. The FDR value was set to 5% (red lines). Peptides displaying no statistically significant difference of deuterium uptake between states are clustered on the right hand corner of the plot.

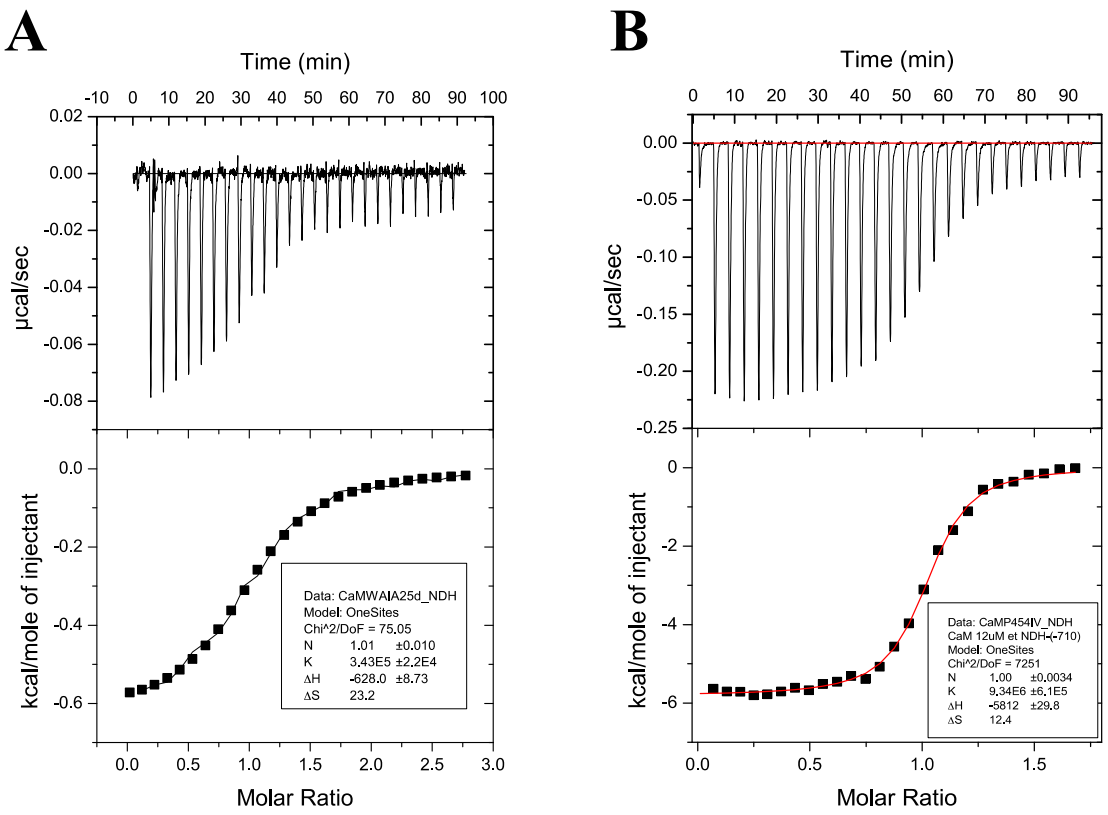

Figure S11: Isothermal titration calorimetry of holo-CaM by P454-derived peptides performed on a VP-ITC instrument. The $P454_{W458A\text{-}I479A}$ (**A**) and $P454_{I479V}$ (**B**) peptides are loaded in the syringe at 130 µM and injected in the cell containing holo-CaM at 10 µM. The free energy values of peptide:CaM interaction are listed in Table S3.

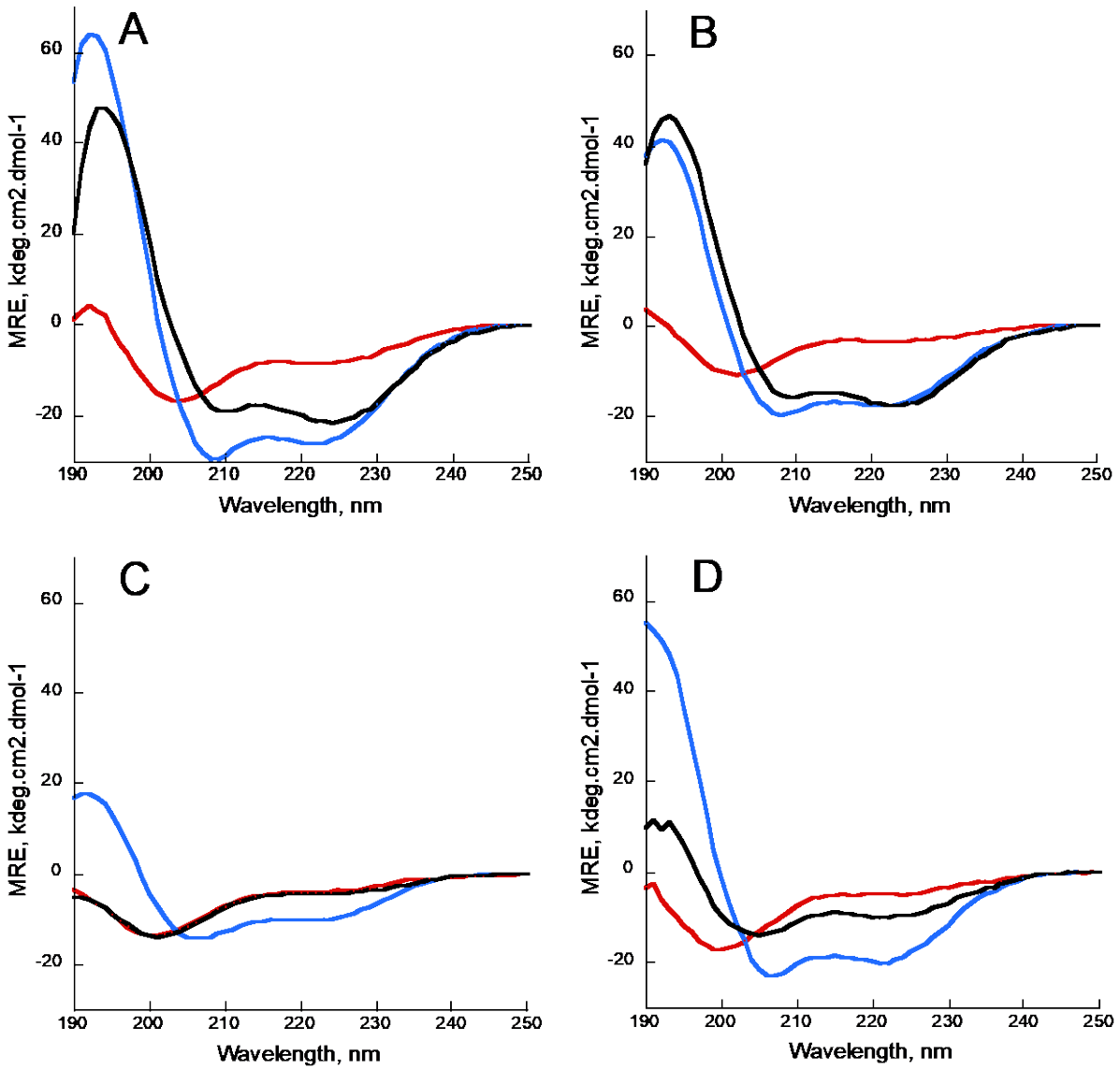

Figure S12: Synchrotron radiation circular dichroism in the far-UV region of P454-derived peptides. The far-UV CD spectra of the peptides have been acquired at 25°C in buffer A (red), in the presence of 20% TFE (blue) or in the presence of SUVs composed of POPC:POPG 8:2 at 2 mM lipids (black). Far-UV CD spectra of the following peptides are shown: P454 (**A**), P454 L481A (**B**), P454 I479A (**C**) and P454 R12Q (**D**). CD units are expressed as mean residue ellipticity (MRE)/1000, i.e., in Kdeg.cm^2.dmol^{-1}. The secondary structure content of the peptides is obtained from the deconvolution of the far-UV CD spectra (see Table S8) using the BestSel software [17] available at http://bestsel.elte.hu/index.php.

Figure S13: Map of pCACTw11 plasmid and DNA sequence of encoded CyaA gene

A) pCACTw11 plasmid map

Schematic map of pCACTw11 plasmid highlighting the regions

The open reading frame coding for the wild type CyaA is in orange with the segment located between the BstBI and NcoI sites replaced by a synthetic DNA fragment highlighted in magenta. The P454 coding region is in blue.

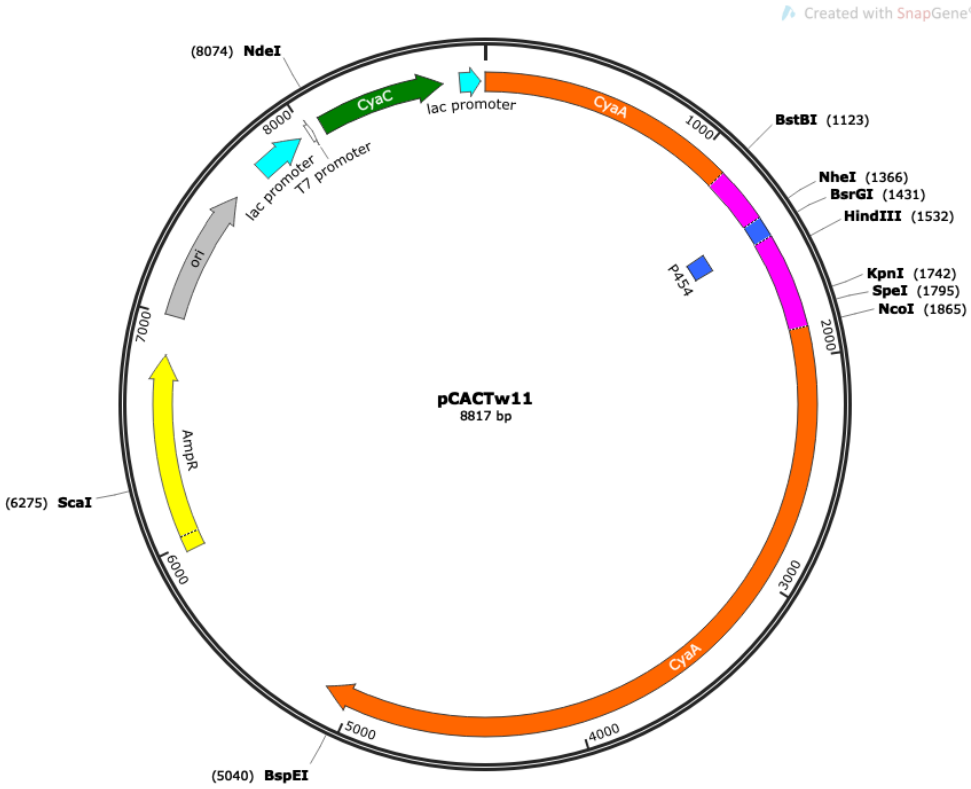

B) CyaA WT open reading frame in pCACTw11 plasmid

The full CyaA open reading frame is shown below with the synthetic DNA fragment located between the BstBI and NcoI sites in magenta. The P454 coding region is in blue. The bold underlined sequences correspond to the BstBI, NheI, KpnI and NcoI restriction sites that were used for subcloning the various synthetic DNA fragment encoding the modified CyaA toxins produced in this work.

ATGACCATGCAGCAATCGCATCAGGCTGGTTACGCAAACGCCGCCGACCGGGAG
TCTGGCATCCCCGCAGCCGTACTCGATGGCATCAAGGCCGTGGCGAAGGAAAAA
AACGCCACATTGATGTTCCGCCTGGTCAACCCCCATTCCACCAGCCTGATTGCCG
AAGGGGTGGCCACCAAAGGATTGGGCGTGCACGCCAAGTCGTCCGATTGGGGGT
TGCAGGCGGGCTACATTCCCGTCAACCCGAATCTTTCCAAACTGTTCGGCCGTGC
GCCCGAGGTGATCGCGCGGGCCGACAACGACGTCAACAGCAGCCTGGCGCATGG
CCATACCGCGGTCGACCTGACGCTGTCGAAAGAGCGGCTTGACTATCTGCGGCAA
GCGGGCCTGGTCACCGGCATGGCCGATGGCGTGGTCGCGAGCAACCACGCAGGC
TACGAGCAGTTCGAGTTTCGCGTGAAGGAAACCTCGGACGGGCGCTATGCCGTGC
AGTATCGCCGCAAGGGCGGCGACGATTTCGAGGCGGTCAAGGTGATCGGCAATG

CCGCCGGTATTCCACTGACGGCGGATATCGACATGTTCGCCATTATGCCGCATCT
GTCCAACTTCCGCGACTCGGCGCGCAGTTCGGTGACCAGCGGCGATTCGGTGACC
GATTACCTGGCGCGCACGCGGCGGGCCGCCAGCGAGGCCACGGGCGGCCTGGAT
CGCGAACGCATCGACTTGTTGTGGAAAATCGCTCGCGCCGGCGCCCGTTCCGCAG
TGGGCACCGAGGCGCGTCGCCAGTTCCGCTACGACGGCGACATGAATATCGGCG
TGATCACCGATTTCGAGCTGGAAGTGCGCAATGCGCTGAACAGGCGGGCGCACG
CCGTCGGCGCGCAGGACGTGGTCCAGCATGGCACTGAGCAGAACAATCCTTTCCC
GGAGGCAGATGAGAAGATTTTCGTCGTATCGGCCACCGGTGAAAGCCAGATGCT
CACGCGCGGGCAACTGAAGGAATACATTGGCCAGCAGCGCGGCGAGGGCTATGT
CTTCTACGAGAACCGTGCATACGGCGTGGCGGGGAAAAGCCTGTTCGACGATGG
GCTGGGAGCCGCGCCCGGCGTGCCGAGCGGACG**TTCGAA**GTTCTCGCCGGATGT
ACTGGAAACCGTTCCGGCGTCACCAGGTTTGCGTCGTCCTTCGCTGGGTGCAGTT
GAACGTCAGGATTCTGGTTATGACTCTCTTGATGGTGTTGGTTCGCGTTCTTTCTC
ATTAGGTGAGGTTTCTGACATGGCTGCAGTTGAAGCAGCTGAACTGGAAATGACT
CGTCAAGTTTTACACGCTGGTGCACGTCAGGACGATGCTGAGCCAGGTGTTTCTG
GT**GCTAGC**GCTCATTGGGGTCAGCGTGCTCTGCAAGGTGCTCAGGCTGTTGCAGC
TGCTCAGCGTCTTGTACATGCTATTGCACTGATGACTCAATTCGGGCGCGCCGGTT
CTACTAACACTCCACAGGAAGCTGCTTCTCTTTCTGCTGCAGTTTTCGGTCTGGGT
GAAGCTTCTAGCGCAGTAGCTGAAACTGTTTCTGGTTTTTTCCGTGGTTCTTCACG
CTGGGCTGGCGGTTTCGGCGTGGCTGGTGGCGCAATGGCTCTGGGAGGTGGTATC
GCTGCAGCTGTTGGTGCTGGTATGTCTTTGACTGATGACGCTCCAGCTGGTCAAA
AAGCTGCAGCTGGTGCTGAAATTGCTCTGCAGTTAACAGGT**GGTACC**GTTGAGCT
GGCTTCTTCCATTGCTTTGGCCTTAGCTGCAGCTCGTGGTGTAACTAGTGGCTTGC
AGGTTGCCGGTGCTTCTGCAGGTGCGGCTGCTGGTGCATTGGCCGCGGCGCTCAG
TC**CCATGG**AGATCTACGGCCTGGTGCAGCAATCGCACTATGCGGATCAGCTGGA
CAAGCTGGCGCAGGAATCGAGCGCATACGGTTACGAGGGCGACGCCTTGCTGGC
CCAGCTGTATCGCGACAAGACGGCCGCCGAGGGCGCCGTCGCCGGCGTCTCCGC
CGTCCTGAGCACGGTGGGGGCGGCGGTGTCGATCGCCGCGGCGGCCAGCGTGGT
AGGGGCCCCGGTGGCGGTGGTCACTTCCTTGCTGACCGGGGCTCTCAACGGCATC
CTGCGCGGCGTGCAGCAGCCCATCATCGAAAAGCTGGCCAACGATTACGCTCGC
AAGATCGACGAGCTGGGCGGGCCGCAAGCGTACTTCGAGAAAAACCTGCAGGCG
CGTCACGAACAACTGGCCAATTCGGACGGCCTACGGAAAATGCTGGCCGACCTG
CAGGCCGGTTGGAACGCCAGCAGCGTGATCGGGGTGCAGACGACAGAGATCTCC
AAGTCGGCGCTCGAACTGGCCGCCATTACCGGCAACGCGGACAACCTGAAATCC
GTCGACGTGTTCGTGGACCGCTTCGTCCAGGGCGAGCGGGTGGCCGGCCAGCCG
GTGGTCCTCGACGTCGCCGCCGGCGGCATCGATATCGCCAGCCGCAAGGGCGAG
CGGCCGGCGCTGACGTTCATCACGCCGCTGGCCGCGCCAGGAGAAGAGCAGCGC
CGGCGCACGAAAACGGGCAAGAGCGAATTCACCACATTCGTCGAGATCGTGGGC
AAGCAGGACCGCTGGCGCATCCGGGACGGCGCGGCCGACACCACCATCGATCTG
GCCAAGGTGGTGTCGCAACTGGTCGACGCCAATGGCGTGCTCAAGCACAGCATC
AAACTGGATGTGATCGGCGGAGATGGCGATGACGTCGTGCTTGCCAATGCTTCGC
GCATCCATTATGACGGCGGCGCGGGCACCAACACGGTCAGCTATGCCGCCCTGG
GTCGACAGGATTCCATTACCGTGTCCGCCGACGGGGAACGTTTCAACGTGCGCAA
GCAGTTGAACAACGCCAACGTGTATCGCGAAGGCGTGGCTACCCAGACAACCGC
CTACGGCAAGCGCACGGAGAATGTCCAATACCGCCATGTCGAGCTGGCCCGTGTC
GGGCAAGTGGTGGAGGTCGACACGCTCGAGCATGTGCAGCACATCATCGGCGGG
GCCGGCAACGATTCGATCACCGGCAATGCGCACGACAACTTCCTAGCCGGCGGG
TCGGGCGACGACAGGCTGGATGGCGGCGCCGGCAACGACACCCTGGTTGGCGGC
GAGGGCCAAAACACGGTCATCGGCGGCGCCGGCGACGACGTATTCCTGCAGGAC
CTGGGGGTATGGAGCAACCAGCTCGATGGCGGCGCGGGCGTCGATACCGTGAAG

TACAACGTGCACCAGCCTTCCGAGGAGCGCCTCGAACGCATGGGCGACACGGGC
ATCCATGCCGATCTTCAAAAGGGCACGGTCGAGAAGTGGCCGGCCCTGAACCTGT
TCAGCGTCGACCATGTCAAGAATATCGAGAATCTGCACGGCTCCCGCCTAAACGA
CCGCATCGCCGGCGACGACCAGGACAACGAGCTCTGGGGCCACGATGGCAACGA
CACGATACGCGGCCGGGGCGGCGACGACATCCTGCGCGGCGGCCTGGGCCTGGA
CACGCTGTATGGCGAGGACGGCAACGACATCTTCCTGCAGGACGACGAGACCGT
CAGCGATGACATCGACGGCGGCGCGGGGCTGGACACCGTCGACTACTCCGCCAT
GATCCATCCAGGCAGGATCGTTGCGCCGCATGAATACGGCTTCGGGATCGAGGC
GGACCTGTCCAGGGAATGGGTGCGCAAGGCGTCCGCGCTGGGCGTGGACTATTA
CGATAATGTCCGCAATGTCGAAAACGTCATCGGTACGAGCATGAAGGATGTGCTC
ATCGGCGACGCGCAAGCCAATACCCTGATGGGCCAGGGCGGCGACGATACCGTG
CGCGGCGGCGACGGCGATGATCTGCTGTTCGGCGGCGACGGCAACGACATGCTG
TATGGCGACGCCGGCAACGACACCCTCTACGGGGGGCTGGGCGACGATACCCTT
GAAGGCGGCGCGGGCAACGATTGGTTCGGCCAGACGCAGGCGCGCGAGCATGAC
GTGCTGCGCGGCGGAGATGGGGTGGATACCGTCGATTACAGCCAGACCGGCGCG
CATGCCGGCATTGCCGCGGGTCGCATCGGGCTGGGCATCCTGGCTGACCTGGGCG
CCGGCCGCGTCGACAAGCTGGGCGAGGCCGGCAGCAGCGCCTACGATACGGTTT
CCGGTATCGAGAACGTGGTGGGCACGGAACTGGCCGACCGCATCACGGGCGATG
CGCAGGCCAACGTGCTGCGCGGCGCGGGTGGCGCCGACGTGCTTGCGGGCGGCG
AGGGCGACGATGTGCTGCTGGGCGGCGACGGCGACGACCAGCTGTCGGGCGACG
CCGGACGCGATCGCTTGTACGGCGAAGCCGGTGACGACTGGTTCTTCCAGGATGC
CGCCAATGCCGGCAATCTGCTCGACGGCGGCGACGGCCGCGATACCGTGGATTTC
AGCGGCCCGGGCCGGGGCCTCGACGCCGGCGCAAAGGGCGTATTCCTGAGCTTG
GGCAAGGGGTTCGCCAGCCTGATGGACGAACCCGAAACCAGCAACGTGTTGCGC
AATATCGAGAACGCCGTGGGCAGCGCGCGTGATGACGTGCTGATCGGCGACGCA
GGCGCCAACGTCCTCAATGGCCTGGCGGGCAACGACGTGCTGTCCGGCGGCGCT
GGCGACGATGTGCTGCTGGGCGACGAGGGCTCGGACCTGCTCAGCGGCGATGCG
GGCAACGACGATCTGTTCGGCGGGCAGGGCGATGATACTTATCTGTTCGGGGTCG
GGTACGGGCACGACACGATCTACGAATCGGGCGGCGGCCATGACACCATCCGCA
TCAACGCGGGGGCGGACCAGCTGTGGTTCGCGCGCCAGGGCAACGACCTGGAGA
TCCGCATTCTCGGCACCGACGATGCACTTACCGTGCACGACTGGTATCGCGACGC
CGATCACCGGGTGGAAATCATCCATGCCGCCAACCAGGCGGTAGACCAGGCAGG
CATCGAAAAGCTGGTCGAGGCAATGGCGCAGTATCCGGACCCCGGCGCGGCGGC
GGCTGCCCCGCCGGCGGCGCGCGTGCCGGACACGCTGATGCAGTCCCTGGCTGTC
AACTGGCGCTGA

Figure S13 continued next page

C) Synthetic DLTW11 DNA fragment

Sequence of the synthetic DNA fragment used for pCACTw11 construction. In black letters are the extra sequence needed for Hifi cloning while the codon-optimized CyaA sequence located between the BstBI and NcoI sites is in magenta. The P454 coding region is in blue. The bold underlined sequences correspond to the BstBI, NheI, KpnI and NcoI restriction sites used for subcloning.

CCCGGCGTGCCGAGCGGACGTTCGAAGTTCTCGCCGGATGTACTGGAAACCGT
TCCGGCGTCACCAGGTTTGCGTCGTCCTTCGCTGGGTGCAGTTGAACGTCAGGAT
TCTGGTTATGACTCTCTTGATGGTGTTGGTTCGCGTTCTTTCTCATTAGGTGAGGTT
TCTGACATGGCTGCAGTTGAAGCAGCTGAACTGGAAATGACTCGTCAAGTTTTAC
ACGCTGGTGCACGTCAGGACGATGCTGAGCCAGGTGTTTCTGGT**GCTAGC**GCTC
ATTGGGGTCAGCGTGCTCTGCAAGGTGCTCAGGCTGTTGCAGCTGCTCAGCGTCT
TGTACATGCTATTGCACTGATGACTCAATTCGGGCGCGCCGGTTCTACTAACACT
CCACAGGAAGCTGCTTCTCTTTCTGCTGCAGTTTTCGGTCTGGGTGAAGCTTCTAG
CGCAGTAGCTGAAACTGTTTCTGGTTTTTTCCGTGGTTCTTCACGCTGGGCTGGCG
GTTTCGGCGTGGCTGGTGGCGCAATGGCTCTGGGAGGTGGTATCGCTGCAGCTGT
TGGTGCTGGTATGTCTTTGACTGATGACGCTCCAGCTGGTCAAAAAGCTGCAGCT
GGTGCTGAAATTGCTCTGCAGTTAACAGGT**GGTACC**GTTGAGCTGGCTTCTTCCA
TTGCTTTGGCCTTAGCTGCAGCTCGTGGTGTAACTAGTGGCTTGCAGGTTGCCGGT
GCTTCTGCAGGTGCGGCTGCTGGTGCATTGGCCGCGGCGCTCAGTC**CCATGG**AG
ATCTACGGCCTGGTGCAG

D) Synthetic DLTW16 DNA fragment coding for CyaA$_{Mut1}$.

Sequence of the synthetic DNA fragment used for pCACTw16 construction. The color code is same as above. Highlighted in yellow are the 6 codons that were changed.

CCCGGCGTGCCGAGCGGACGTTCGAAGTTCTCGCCGGATGTACTGGAAACCGT
TCCGGCGTCACCAGGTTTGCGTCGTCCTTCGCTGGGTGCAGTTGAACGTCAGGAT
TCTGGTTATGACTCTCTTGATGGTGTTGGTTCGCGTTCTTTCTCATTAGGTGAGGTT
TCTGACATGGCTGCAGTTGAAGCAGCTGAACTGGAAATGACTCGTCAAGTTTTAC
ACGCTGGTGCACGTCAGGACGATGCTGAGCCAGGTGTTTCTGGT**GCTAGC**GCTC
ATTGGGGTCAGGAAGCTGCACAAGGTGCTCAGGCTGTTGCAGCTGCTCAGGAAG
CAGTATCTGCTGCAGCACTGATGACTCAATTCGGGCGCGCCGGTTCTACTAACAC
TCCACAGGAAGCTGCTTCTCTTTCTGCTGCAGTTTTCGGTCTGGGTGAAGCTTCTA
GCGCAGTAGCTGAAACTGTTTCTGGTTTTTTCCGTGGTTCTTCACGCTGGGCTGGC
GGTTTCGGCGTGGCTGGTGGCGCAATGGCTCTGGGAGGTGGTATCGCTGCAGCTG
TTGGTGCTGGTATGTCTTTGACTGATGACGCTCCAGCTGGTCAAAAAGCTGCAGC
TGGTGCTGAAATTGCTCTGCAGTTAACAGGT**GGTACC**GTTGAGCTGGCTTCTTCC
ATTGCTTTGGCCTTAGCTGCAGCTCGTGGTGTAACTAGTGGCTTGCAGGTTGCCG
GTGCTTCTGCAGGTGCGGCTGCTGGTGCATTGGCCGCGGCGCTCAGTC**CCATGG**A
GATCTACGGCCTGGTGCAG

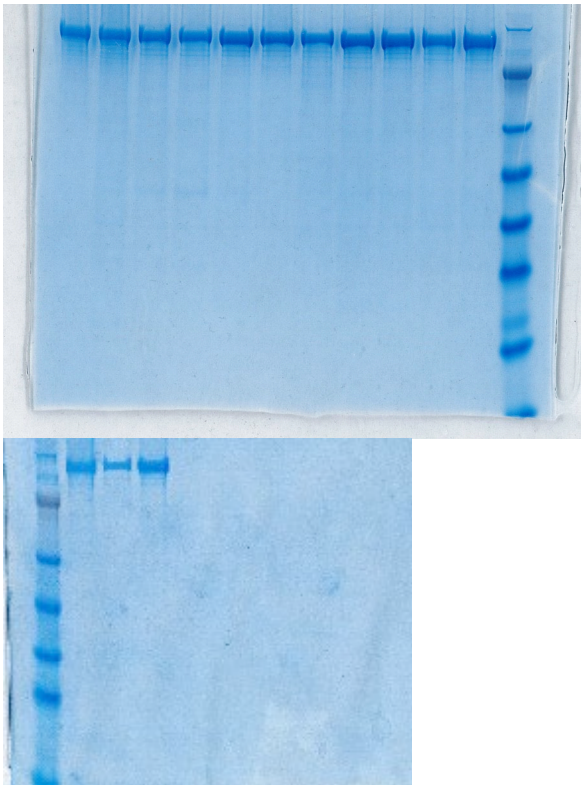

Figure S14: SDS-PAGE of purified recombinant CyaA proteins. Two µg of each recombinant CyaA protein are loaded on each line. First (top) SDS-PAGE, from left to right: CyaA WT (batch #0918); CyaA WT (batch #0719); $CyaA_{Mut6}$; $CyaA_{R12E}$; $CyaA_{Mut1}$; $CyaA_{Mut7}$; $CyaA_{R12Q}$; $CyaA_{Mut2}$; $CyaA_{Mut4}$; $CyaA_{R12A}$; $CyaA_{R12K}$ and Ladder SeeBlue Plus. Second (bottom) SDS-PAGE, from left to right: Ladder SeeBlue Plus; CyaA WT (batch #0918); $CyaA_{Mut3}$ and $CyaA_{Mut5}$.

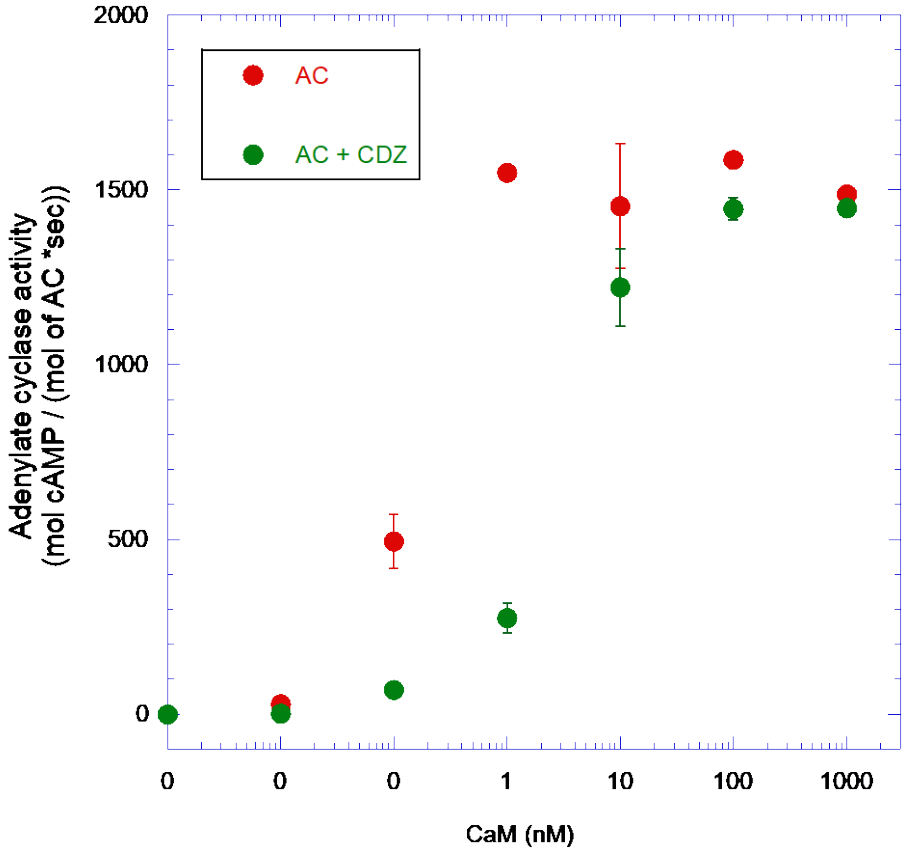

Figure S15: CaM-dependent activation of AC with or without calmidazolium (CDZ). The adenylate cyclase activity of AC384GK (encompassing the full catalytic domain of CyaA) was measured in the presence of the indicated concentrations of CaM (red symbols) and in the presence of 10 µM calmidazolium (CDZ, green symbols) as previously described in Vougier *et al.* 2004 at 30 °C, pH 8.0 and 0.1 mM $CaCl_2$. AC384GK was at 0.2 nM. The adenylate cyclase activity is expressed as mol of cAMP per sec per mol of AC384GK.

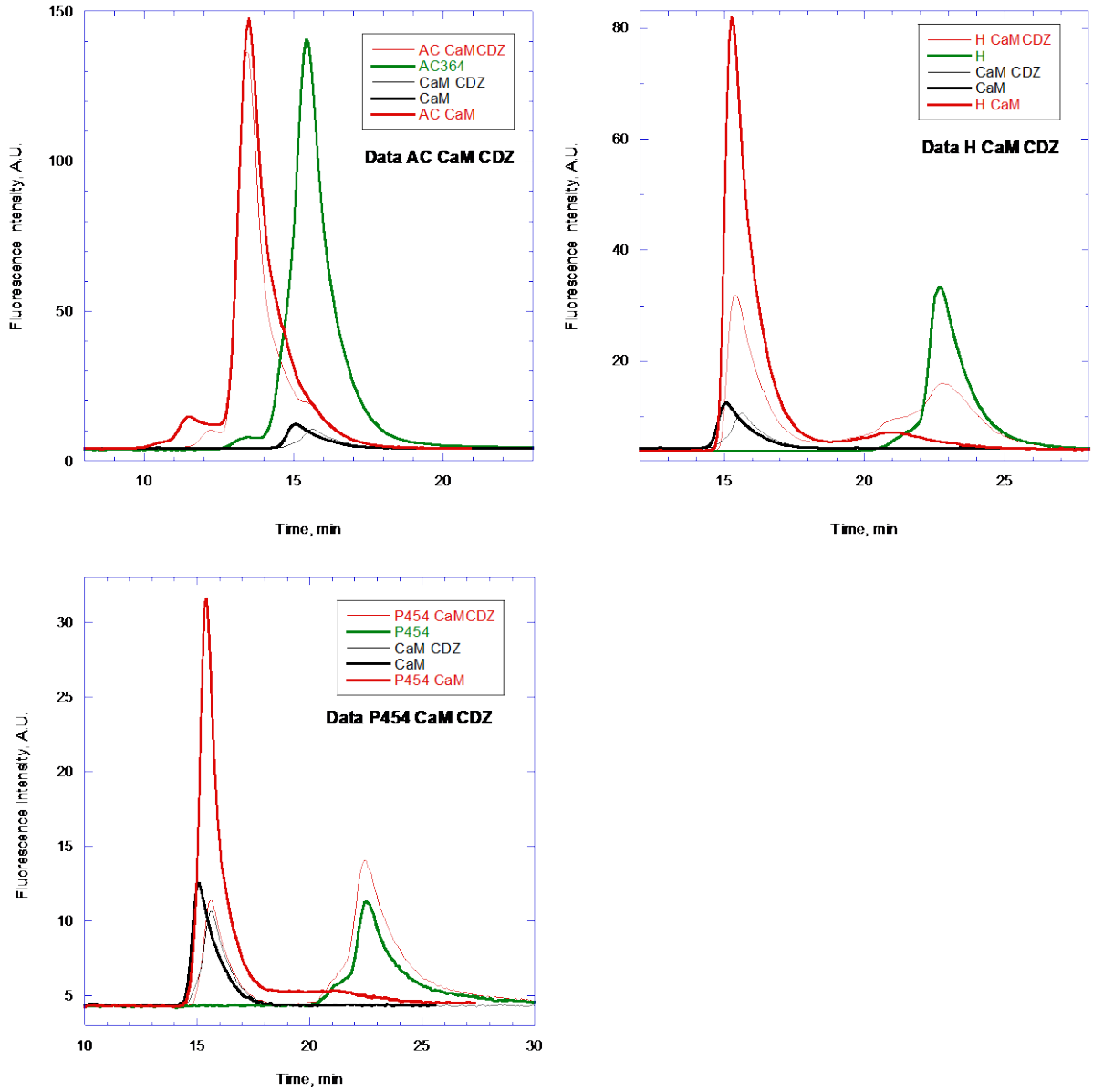

Figure S16: Size exclusion chromatography of AC, H and P454 in the absence and presence of CaM and CDZ followed by tryptophan intrinsic fluorescence (excitation: 280 nm; emission: 340 nm). AC, H and P454 contain tryptophan residues. CaM does not contain any tryptophan residue but 8 phenylalanine residues, providing a residual fluorescence signal. The chromatograms of AC, H and P454 are green. CaM is dark and the complexes are red. In the presence of CDZ, the chromatograms are identified by hairline traces (CaM:CDZ is in light dark and complexes:CDZ are in light red). The molecules were mixed at the following finale concentrations: AC, H and P454 at 10 µM, CaM at 15 µM and CDZ at 40 µM. The chromatograms of CaM alone and CaM:CDZ shown in the 3 figures are from the same samples. The SEC experiments were performed on a TSKgel G3000SW 7.5 mm ID * 300 mm. The buffer is 20 mM Hepes, 150 mM NaCl, 2 mM CaCl2, pH 7.4.

References

1 A. Voegele, O. Subrini, N. Sapay, D. Ladant, and A. Chenal, *Toxins (Basel)*. 9, (2017)
2 S. Vougier, J. Mary, N. Dautin, J. Vinh, B. Friguet, and D. Ladant, *J Biol Chem*. 279, 30210-8 (2004)
3 J. C. Karst, A. C. Sotomayor Perez, J. I. Guijarro, B. Raynal, A. Chenal, and D. Ladant, *Biochemistry*. 49, 318-28 (2010)
4 D. P. O'Brien, D. Durand, A. Voegele, V. Hourdel, M. Davi, J. Chamot-Rooke, P. Vachette, S. Brier, D. Ladant, and A. Chenal, *PLoS Biol*. 15, e2004486 (2017)
5 J. F. Sambrook, and D. W. Russell, *Cold Spring Harbor, NY: Cold Spring Harbor Laboratory Press*. (2006)
6 R. Osicka, A. Osickova, T. Basar, P. Guermonprez, M. Rojas, C. Leclerc, and P. Sebo, *Infection and Immunity*. 68, 247-256 (2000)
7 D. G. Gibson, L. Young, R. Y. Chuang, J. C. Venter, C. A. Hutchison, and H. O. Smith, *Nature Methods*. 6, 343-U41 (2009)
8 J. C. Karst, V. Y. Ntsogo Enguene, S. E. Cannella, O. Subrini, A. Hessel, S. Debard, D. Ladant, and A. Chenal, *J Biol Chem*. 289, 30702-16 (2014)
9 S. E. Cannella, V. Y. Ntsogo Enguene, M. Davi, C. Malosse, A. C. Sotomayor Perez, J. Chamot-Rooke, P. Vachette, D. Durand, D. Ladant, and A. Chenal, *Sci Rep*. 7, 42065 (2017)
10 D. P. O'Brien, S. E. Cannella, A. Voegele, D. Raoux-Barbot, M. Davi, T. Douche, M. Matondo, S. Brier, D. Ladant, and A. Chenal, *FASEB J*. 33, fj201802442RR (2019)
11 A. C. Sotomayor-Perez, J. C. Karst, D. Ladant, and A. Chenal, *Methods Mol Biol*. 896, 331-49 (2012)
12 O. Subrini, A. C. Sotomayor-Perez, A. Hessel, J. Spiaczka-Karst, E. Selwa, N. Sapay, R. Veneziano, J. Pansieri, J. Chopineau, D. Ladant, and A. Chenal, *J Biol Chem*. 288, 32585-98 (2013)
13 A. C. Sotomayor Perez, J. C. Karst, M. Davi, J. I. Guijarro, D. Ladant, and A. Chenal, *J Mol Biol*. 397, 534-49 (2010)
14 S. H. White, and W. C. Wimley, *Annu Rev Biophys Biomol Struct*. 28, 319-65 (1999)
15 P. Schuck, *Biophys J*. 78, 1606-19 (2000)
16 A. Micsonai, F. Wien, L. Kernya, Y. H. Lee, Y. Goto, M. Refregiers, and J. Kardos, *Proc Natl Acad Sci U S A*. 112, E3095-103 (2015)
17 A. Micsonai, F. Wien, E. Bulyaki, J. Kun, E. Moussong, Y. H. Lee, Y. Goto, M. Refregiers, and J. Kardos, *Nucleic Acids Res*. 46, W315-W322 (2018)
18 G. Karimova, C. Fayolle, S. Gmira, A. Ullmann, C. Leclerc, and D. Ladant, *Proc Natl Acad Sci U S A*. 95, 12532-7 (1998)
19 A. Rogel, and E. Hanski, *J Biol Chem*. 267, 22599-605 (1992)
20 G. David, and J. Pérez, *J. Appl. Cryst.* 42, 892-900. (2009)
21 J. Trewhella, A. P. Duff, D. Durand, F. Gabel, J. M. Guss, W. A. Hendrickson, G. L. Hura, D. A. Jacques, N. M. Kirby, A. H. Kwan, J. Perez, L. Pollack, T. M. Ryan, A. Sali, D. Schneidman-Duhovny, T. Schwede, D. I. Svergun, M. Sugiyama, J. A. Tainer, P. Vachette, J. Westbrook, and A. E. Whitten, *Acta Crystallogr D Struct Biol*. 73, 710-728 (2017)
22 D. Franke, M. V. Petoukhov, P. V. Konarev, A. Panjkovich, A. Tuukkanen, H. D. T. Mertens, A. G. Kikhney, N. R. Hajizadeh, J. M. Franklin, C. M. Jeffries, and D. I. Svergun, *J Appl Crystallogr*. 50, 1212-1225 (2017)
23 D. Franke, C. M. Jeffries, and D. I. Svergun, *Nat Methods*. 12, 419-22 (2015)
24 A. Guinier, *Ann Phys (Paris)*. 12, 161–237 (1939)
25 D. I. Svergun, *J. Appl. Cryst.* 25, 495-503 (1992)
26 D. Franke, and D. I. Svergun, *J Appl Crystallogr*. 42, 342-346 (2009)

27 D. I. Svergun, *Biophysical Journal*. 76, 2879-2886 (1999)
28 G. Evrard, F. Mareuil, F. Bontems, C. Sizun, and J. Perez, *Journal of Applied Crystallography*. 44, 1264-1271 (2011)
29 P. Weber, C. Pissis, R. Navaza, A. E. Mechaly, F. Saul, P. M. Alzari, and A. Haouz, *Molecules*. 24, (2019)
30 C. Vonrhein, C. Flensburg, P. Keller, A. Sharff, O. Smart, W. Paciorek, T. Womack, and G. Bricogne, *Acta Crystallogr D Biol Crystallogr*. 67, 293-302 (2011)
31 A. J. Mccoy, R. W. Grosse-Kunstleve, P. D. Adams, M. D. Winn, L. C. Storoni, and R. J. Read, *Journal of Applied Crystallography*. 40, 658-674 (2007)
32 P. Emsley, and K. Cowtan, *Acta Crystallographica Section D-Biological Crystallography*. 60, 2126-2132 (2004)
33 G. Bricogne, E. Blanc, M. Brandl, C. Flensburg, and P. Keller, *Cambridge, UK: Global Phasing Ltd.*, (2011)
34 V. Hourdel, S. Volant, D. P. O'Brien, A. Chenal, J. Chamot-Rooke, M. A. Dillies, and S. Brier, *Bioinformatics*. (2016)
35 D. Orthaber, A. Bergmann, and O. Glatter, *Journal of Applied Crystallography*. 33, 218-225 (2000)
36 R. D. Brokx, M. M. Lopez, H. J. Vogel, and G. I. Makhatadze, *J Biol Chem*. 276, 14083-91 (2001)
37 R. Chattopadhyaya, W. E. Meador, A. R. Means, and F. A. Quiocho, *J Mol Biol*. 228, 1177-92 (1992)